*Review*

# Growth Processing and Strategies: A Way to Improve the Gas Sensing Performance of Nickel Oxide-Based Devices

Marwa Ben Arbia [ID] and Elisabetta Comini *[ID]

Sensor Laboratory, Department of Information Engineering, University of Brescia, Via Valotti 9, 25133 Brescia, Italy; m.benarbia@studenti.unibs.it
* Correspondence: elisabetta.comini@unibs.it

**Abstract:** The review paper provides a comprehensive analysis of nickel oxide (NiO) as an emerging material in environmental monitoring by surveying recent developments primarily within the last three years and reports the growth processing and strategies employed to enhance NiO sensing performance. It covers synthesis methods for pristine NiO, including vapor-phase, liquid-phase, and solution-processing techniques, highlighting advantages and limitations. The growth mechanisms of NiO nanostructures are explored, with a focus on the most recent research studies. Additionally, different strategies to improve the gas sensing performance of NiO are discussed (i.e., surface functionalization by metallic nanoparticles, heterostructure formation, carbon-based nanomaterials, and conducting polymers). The influence of these strategies on selectivity, sensitivity, response time, and stability of NiO-based sensors is thoroughly examined. Finally, the challenges and future directions that may lead to the successful development of highly efficient NiO-based gas sensors for environmental monitoring are introduced in this review.

**Keywords:** nickel oxide; nanostructures; composites; heterojunctions; gas sensing

## 1. Introduction

Environmental monitoring is of great importance in today's world due to the increasing awareness of environmental issues and the need for sustainable development. It involves systematic observation, measurement, and analysis of environmental parameters to understand and assess the state of the environment, detect changes, and identify potential risks or hazards. Metal oxide gas sensors play a significant role in environmental monitoring, particularly in the detection and measurement of various gases and pollutants in the air. These sensors are designed to detect and quantify gases such as carbon monoxide (CO), nitrogen dioxide ($NO_2$), ozone ($O_3$), sulfur dioxide ($SO_2$), volatile organic compounds (VOCs), and many others [1]. The use of metal oxide gas sensors in environmental monitoring offers several advantages. They are sensitive to low gas concentrations, allowing for early detection of pollutants and potential hazards. They are also relatively low-cost compared to other sensor technologies, making them accessible for widespread deployment [2–4].

Emerging materials for gas-sensing metal oxide semiconductors (MOX) have been extensively investigated. Among these materials, we will focus on nickel oxide (NiO), which is a versatile material with a range of properties that make it attractive for various applications, including catalysis, energy storage, solar water oxidation [5], and electronics. NiO has attracted significant research interest due to its unique electronic and magnetic properties, as well as its potential as a cost-effective and environmentally friendly material.

NiO can exist in different crystal phases [6], where the rock salt structure is highly recommended for gas sensors due to its stability at high temperatures [7]. The rock salt structure is characterized by a face-centered cubic (FCC) lattice, with nickel cations ($Ni^{2+}$) occupying the FCC lattice sites, while oxygen anions ($O^{2-}$) fill the octahedral holes between the nickel cations (See Figure 1).
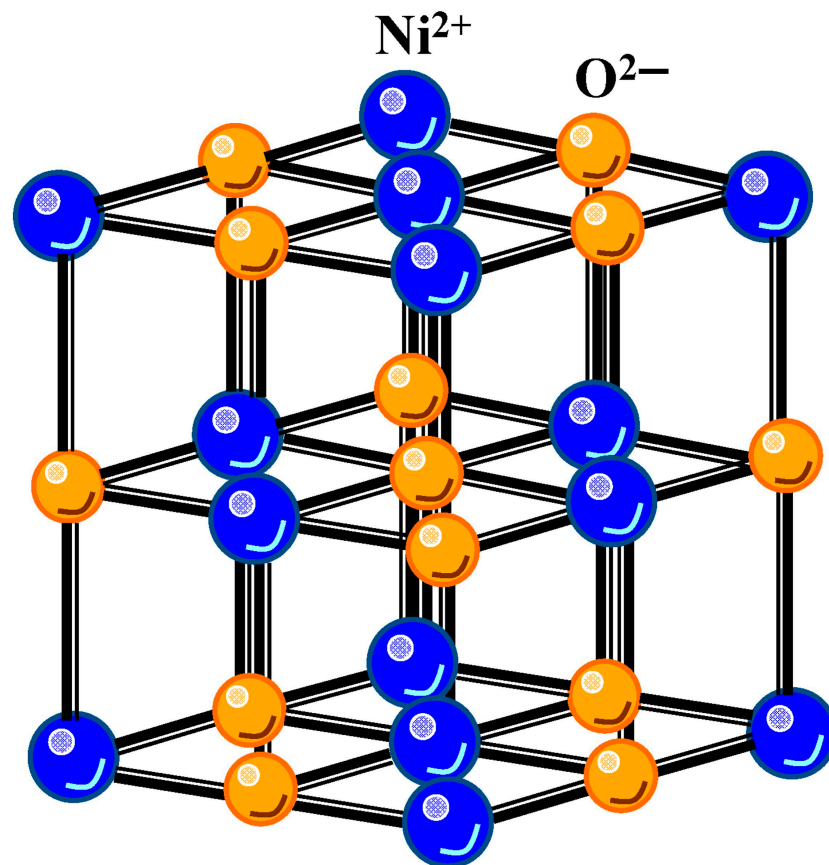
**Figure 1.** FCC crystal structure of NiO, reproduced from reference [8] MDPI publisher (Copyright 2020).

It is important to note that the crystal phase of NiO can be influenced by various factors such as temperature, pressure, and synthesis methods. Moreover, its gas-sensing properties are significantly influenced by its chemical state. The presence of oxygen vacancies in NiO creates active sites for gas molecules to be adsorbed and react, thereby enhancing its gas sensing capabilities. Due to its wide bandgap (3.5–4 eV) [9], the stoichiometric form of NiO behaves as an insulator with a very low intrinsic conductivity of $10^{-13}$ S cm$^{-1}$ at room temperature (RT) [10]. However, NiO is a metal-deficient p-type semiconductor, which means that it contains vacancies in the cation lattice site, specifically nickel vacancies. These vacancies result in a partial conversion of $Ni^{2+}$ ions to $Ni^{3+}$ ions to maintain electrical neutrality within the structure. Consequently, the created $Ni^{3+}$ ions assume the role of charge carriers for conduction in NiO, which facilitates electron transfer and further promotes the formation of oxygen vacancies [11,12].

The presence of nickel defects within NiO material, even at temperatures higher than 150 K, provides complex and variable $O_2$ desorption. This complexity could result in temperature-dependent interactions with specific analytes and lead to enhanced selectivity of humidity-tolerant NiO sensors [13].

The distinctive behavior of NiO in comparison to other commonly used metal oxides is proved by operando diffuse reflectance infrared Fourier transform spectroscopy investigations [14]. It is found that NiO exhibits a good response to CO and $H_2$ analytes in dry and humid conditions. This humidity tolerance is one of the advantages of using such material in real monitoring sensing applications. It is also reported that NiO sensing is primarily driven by the reduction and oxidation of the material rather than the formation of specific ionic species at the surface.

Nickel oxide shows remarkable properties that have been extensively studied and validated as a viable material in gas sensing applications: it has been ranked third in terms of

scientific publications over the past three years, as highlighted in Figure 2. Despite the low sensitivity it shows in comparison with n-type materials, NiO enhances the catalytic effect and humidity tolerance that justifies its inclusion among p-type metal oxide candidates for gas detection in real-environment devices [15].
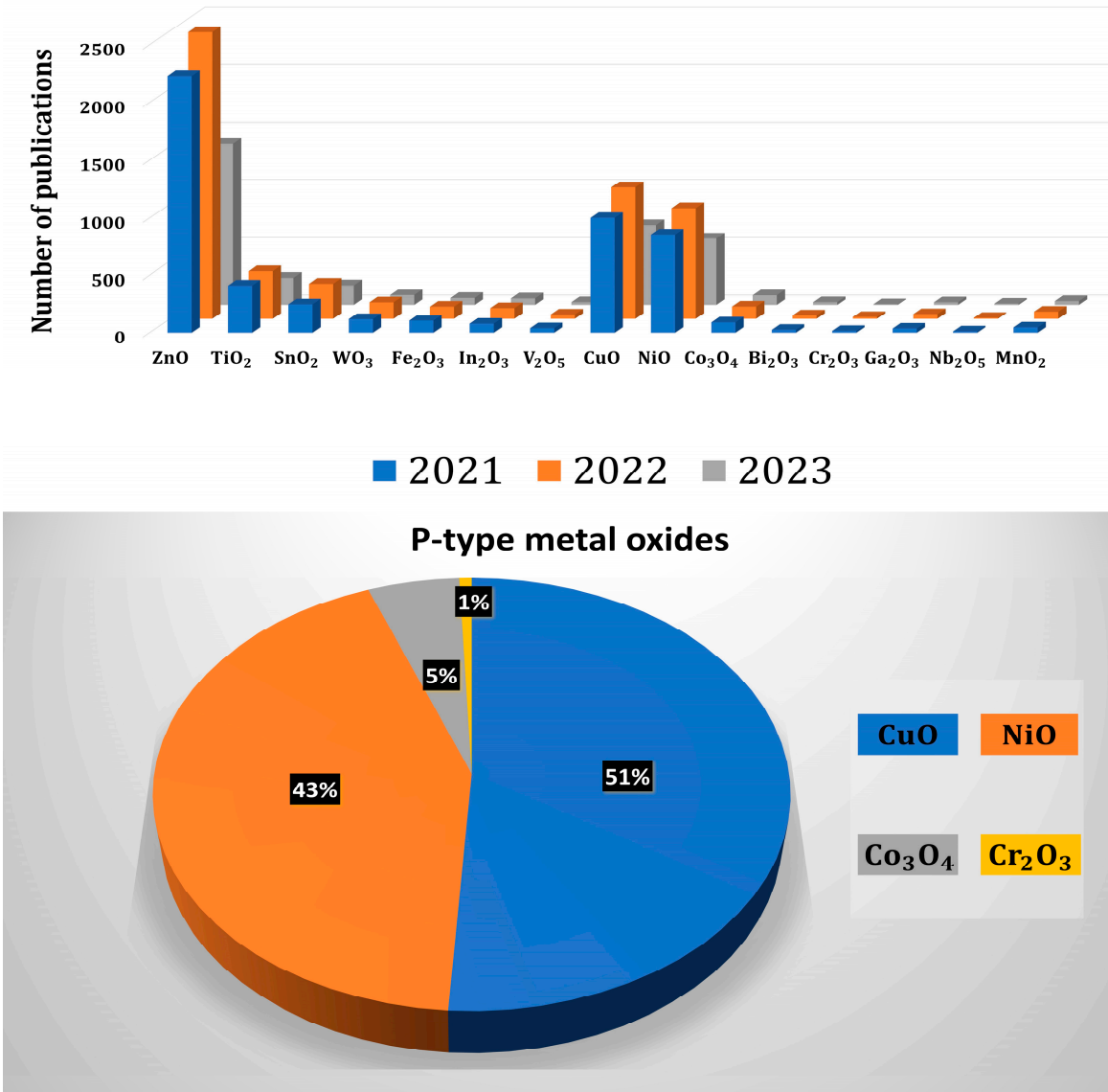


**Figure 2.** Number of scientific publications (research articles) on metal oxide gas sensors over the last three years. Data extracted from Elsevier on 9 May 2023.

Additionally, NiO proves its sensitivity toward several gases, as described in Figure 3, where the greatest number of publications is assigned to ethanol, acetone, and formaldehyde detection.

Several reviews have highlighted the remarkable gas-sensing capabilities of nickel oxide (NiO), particularly in detecting volatile organic compounds (VOCs) and other gases (CO, $NO_2$, $H_2S$, $NH_3$, etc.) [16–18].
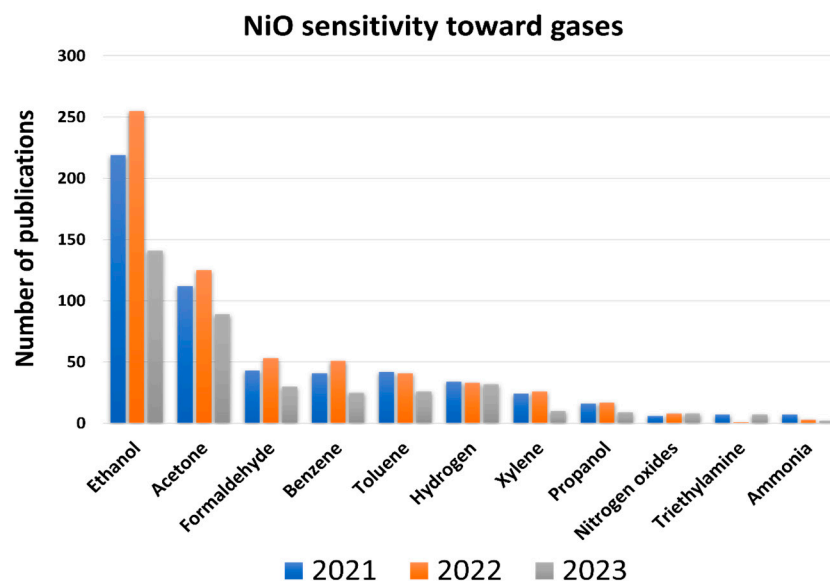
**Figure 3.** Number of research articles on NiO gas sensing toward various gases over the last three years. Data extracted from Elsevier on 21 May 2023 with keywords 'NiO' or 'nickel oxide', 'gas sensing' or 'gas sensors', and 'specified gas'.

To highlight the strides in understanding and using nickel oxide for gas sensing, we conducted a comprehensive review. This overview delves into recent research on growth processing, gas sensing mechanisms, and strategies to enhance NiO performance. The section describing the growth strategies is devoted to explaining the experimental procedures leading to different morphologies of NiO that can be beneficial for gas sensing applications in the future. The goal is to reinforce the NiO position as a promising material in gas sensing applications by drawing the scientific community's attention to new techniques and conditions that can provide good morphologies and high sensing performance.

## 2. Pristine Nickel Oxide Semiconductor: Growth Strategies

### 2.1. Vapor-Phase Deposition

#### 2.1.1. Sputtering

Sputtering deposition is a physical vapor deposition technique used to deposit thin films of materials onto a substrate. It involves bombarding the target material with high-energy particles in a low-pressure gas environment, causing atoms or molecules to be ejected from the target surface. This process occurs due to the transfer of momentum between the ions and the atoms in the target material. The ions penetrate the surface of the target material and transfer their kinetic energy to the target atoms, causing them to be ejected from the target. This process can occur through a variety of mechanisms, including direct knock-on collisions, momentum transfer through electron excitations, or chemical reactions with the target material. Once ejected, the sputtered atoms can deposit onto a substrate and form a thin film. The quality and properties of the deposited film can be controlled by adjusting the deposition parameters such as the energy and angle of incidence of the ions, the pressure, and the composition of the gas in the sputtering chamber, the time of deposition, target-to-substrate distance, and substrate temperature. A schematic illustration of sputtering concept is presented in Figure 4.

NiO thin film has been widely deposited via sputtering. In the following, we cite some research works and list the deposition parameters and film thicknesses in Table 1.

Notably, film thickness of sputtered NiO as sensing material is very important for gas detection efficiency [19–21], and Table 1 provides a summary of experimental conditions that enable the adjustment of thickness using different modes, pressure, power, and time.
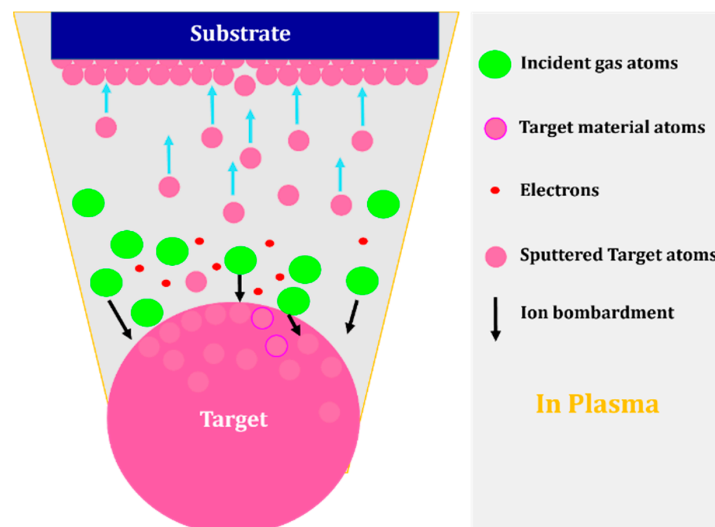
**Figure 4.** Schematic representation of the sputtering process.

**Table 1.** Sputtering parameters for deposition of NiO films and their thicknesses (since 2022).

| Reference | Pressure (mTorr) | Time (s) | Substrate—Temperature | Power (W) | Mode | Film Thickness (nm) |
|---|---|---|---|---|---|---|
| [22] | 2.25 | N/A | ITO/Glass—RT | 200 | DC * | 150 |
| [23] | 0.003 | 3600 | Soda-Lime Glass (SLG)—RT | 90 | RF * | 200 |
| [24] | 10 | NA | PET/ITO—RT | 50 | RF | 200 |
| [25] | 7.5 | 9000 | Glass—RT | 250 | RF | 222 |
| [26] | 3.75 | NA | FTO/Glass—RT | 70 | RF | 25 |
| [27] | 9 | NA | ITO/Glass—RT | 120 | DC | 250 |
| [28] | 15 | 5 | Glass—RT | 100 | RF | 4.99 |
| | | 10 | | | | 21.85 |
| | | 15 | | | | 31.50 |
| | | 20 | | | | 42.10 |
| [29] | 3.75 | NA | Platinum thin film—400 °C | 40 | DC | 50–200 |
| [30] | 7.5 | 3600 | Glass—300 °C | 120 | DC | 160.2 |
| | 9 | | | | | 168.8 |
| | 10.5 | | | | | 166.9 |
| | 12 | | | | | 157.5 |
| | 13.5 | | | | | 150.0 |
| [31] | 37.5 | NA | Silica—400 °C | 100 | RF | 30 |
| | 7.5 | | Silica—RT | 50 | | 30 |
| [32] | 112.5 | 10,800 | Glass—RT | 140 | DC | NA |

* NA: Not Available data; DC: Direct Current (DC) type; RF: Radio Frequency.

NiO-sputtered films have granular structures whose density and homogeneity depend on the deposition factors. Turgut et al. [33] have studied the pressure effect on the morphology of the deposited NiO with bunsenite crystal phase, proving that increasing the working pressure from 0.6 to 2 mTorr leads to changing the nano-pyramidal shape (30–150 nm of size) to the nano-spherical shapes (60 nm) which exhibit more compact surface at high pressure, formed with very small and coalesced granules when compared to the sample grown under moderate pressure (See Figure 5).

The substrate temperature has also impacted the morphology of deposited NiO films. Jamal et al. [34] have investigated its effect on the structural properties by SEM, as shown in Figure 6. However, high temperatures can degrade the crystal quality of the film by decomposing the NiO atoms.
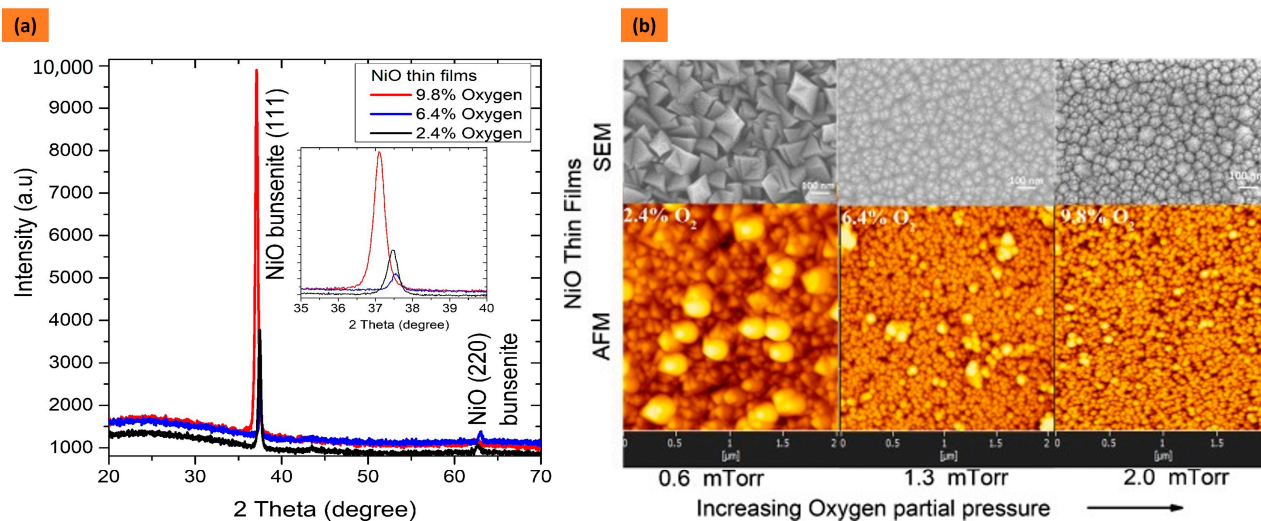
**Figure 5.** XRD patterns (**a**) and SEM-AFM characterization (**b**) of NiO films on glass substrate at various pressures, reproduced from reference [33] Elsevier publisher (Copyright 2018).



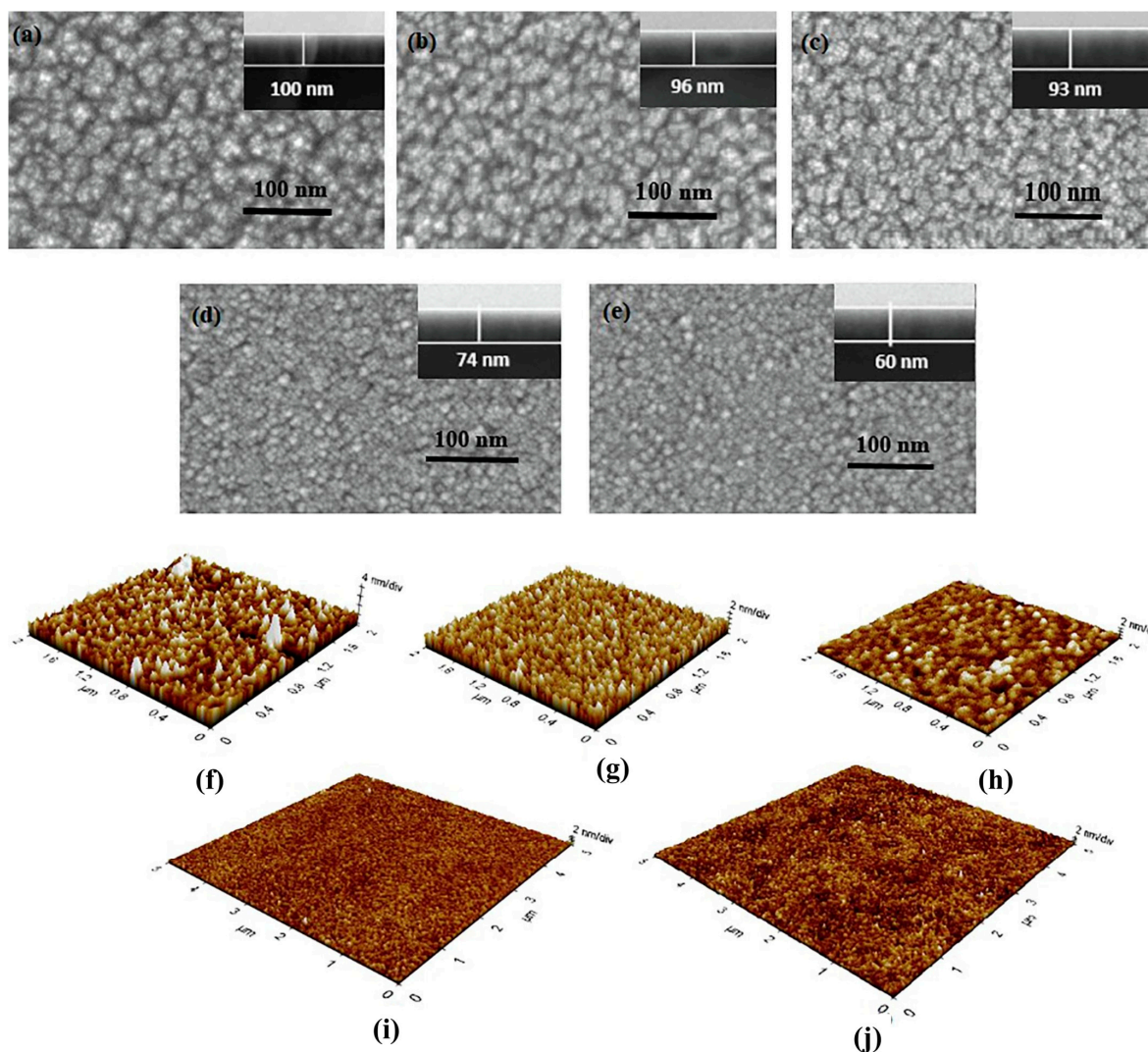**Figure 6.** SEM and SPM micrographs of NiO sputtered at different temperatures: (**a**,**f**) RT; (**b**,**g**) 100 °C; (**c**,**h**) 200 °C; (**d**,**i**) 300 °C; (**e**,**j**) 400 °C, reproduced from reference [34] Elsevier publisher (Copyright 2019).

In another work [35], the growth of sputtered NiO films at 1 Pa on different substrates is reported, showing (111), (200), and (220) diffraction peaks and different texture coefficients, as mentioned in Figure 7a–d. The choice of 1 Pa as a total sputtering pressure is devoted to realizing fiber-textured structures with lower stress. Increasing the oxygen flow led to reach higher fiber texture for NiO thin films deposited on alumina compared to that deposited on glass whose structure has more random texture. TEM images show an epitaxial growth of NiO on alumina with a sharp interface (See Figure 7e–g). In contrast, the deposition of NiO on silicon is non-epitaxial, and the presence of nanocrystals (4 nm) is observed in Figure 7h–j.
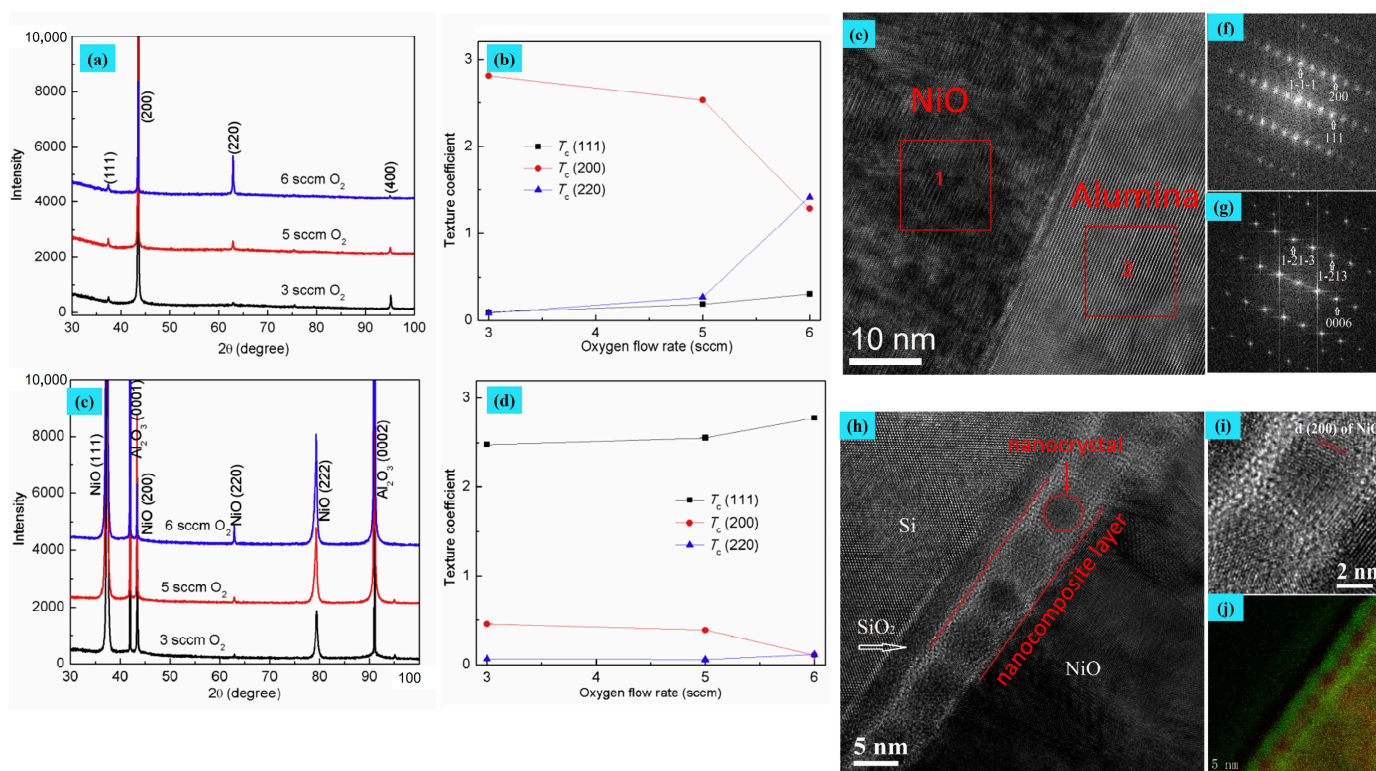


**Figure 7.** (**a**,**b**) XRD patterns and (**c**,**d**) texture coefficient as a function of oxygen flow rate of NiO deposited on glass and alumina, (**e**–**g**) HRTEM and EFTEM images of NiO film and nanocrystals grown on alumina, and (**h**–**j**) HRTEM and EFTEM images of NiO film grown on on silicon, reproduced from reference [35] Elsevier publisher (Copyright 2019).

### 2.1.2. Thermal Evaporation–Condensation

Thermal evaporation–condensation is a common technique for the growth of one-dimensional metal oxide nanostructures. In this technique, a source material, typically in the form of a solid or powder, is heated to its vaporization temperature within a controlled environment. The evaporated material then migrates to a cooler substrate, where it undergoes condensation and nucleation processes. As the vapor contacts the substrate, it condenses and forms nanowires due to the presence of nucleation sites, which can be naturally occurring defects on the substrate (Vapor–Solid process) or intentionally introduced seeds (Vapor–Liquid–Solid process).

Vapor–Liquid–Solid (VLS) growth: In this process, a catalyst material, such as gold (platinum, palladium, etc.), is deposited onto a substrate and then heated in the presence of vapor of the source material, such as a metal or metallic oxide. The source material then dissolves into the catalyst, forming a liquid alloy. As the temperature increases, the alloy becomes supersaturated, and nanowires begin to grow from the liquid–solid interface. The nanowires grow in the direction perpendicular to the substrate surface and are typically single-crystalline [36].

Vapor–Solid (VS) growth: In this process, the source material is heated in a vacuum chamber, causing it to evaporate and condense onto a heated substrate. As the vapor condenses, it forms nanowires on the substrate surface. The nanowires grow in the direction parallel to the substrate surface and are typically polycrystalline [36].

The properties of the nanowires depend significantly on the properties of the source material, the presence of a catalyst, the substrate temperature during the deposition, the evaporation temperature and rate, the deposition time, the pressure, the gas composition, etc. [37–40].

Optimizing these parameters is critical to obtaining high-quality nanowires with the desired properties, and adjustments may be necessary depending on the specific application and material being used.

This vapor-transport technique has been commonly used to grow nanostructures of various materials, including nickel oxide nanowires. The choice of process depends on the desired properties of the nanowires, such as their crystal structure, diameter, length, and density. N. Kaur et al. have prepared NiO nanowires on alumina by VLS process, well described in Figure 8 below.
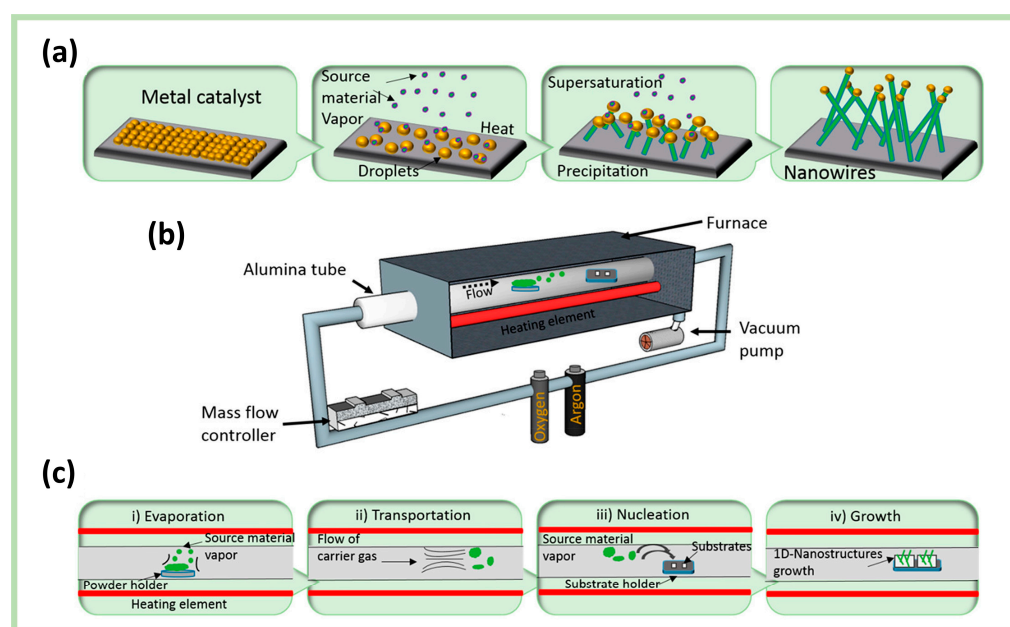


**Figure 8.** Thermal evaporation set-up following the VLS process: (**a**) growth mechanism, (**b**) schematic illustration of the furnace used for the synthesis of NiO material, and (**c**) necessary processes for evaporation-condensation of NiO powder on the substrate, reproduced from reference [41] ACS publisher (Copyright 2020).

VLS growth of NiO structures is realized in such work [42] using different seed layers and substrate temperatures under different argon flows and evaporation temperatures. Kaur et al. show how the density and the shape of nanowires strongly depend on the evaporation conditions. At 1400 °C and 1 mbar, the formation of nanowires is denser and more confined for Au-catalyst than Pt-catalyst. Increasing the substrate temperature led to growing nanowires longer and denser.

### 2.1.3. Thermal Oxidation

Thermal oxidation is a controlled process serving to grow metal oxide compounds using a solid phase source. The material source could be pure metal, or an alloy deposited onto the substrate using techniques like chemical vapor deposition (CVD) or physical vapor deposition (PVD). A high-temperature furnace or reactor able to withstand high temperatures and maintain a controlled atmosphere into which the metallic layer is placed

is recommended for thermal oxidation. Gradually increasing the temperature inside the chamber to the desired level enables the oxidation reaction to progress, where a layer of metal oxide begins to grow on the surface of the metallic layer. This growth occurs at the interface between the metal and the oxidizing atmosphere. The growth rate and thickness of the oxide can be controlled by adjusting parameters like temperature, pressure, time, and gas flow. This method is widely used to obtain metal oxides with different morphologies depending on the temperature, the ramp rate, the pressure, the oxidation time, the metallic layer properties, and the surrounding environment [43–46].

Nickel oxidation has been the subject of several studies to attend NiO structures with adjustable properties.

The formation of NiO on Ni metallic film in a high-temperature regime by varying the oxidation temperature from 600 to 1200 °C implies various morphological aspects [47]. At temperatures exceeding 800 °C, a continuous NiO scale envelops the surface, with its grain size augmenting proportionally to the temperature increment. At temperatures below 700 °C, the surface shows irregularities. Some parts have a thin layer of NiO, and streaks of NiO are visible along the polished surface steps [47]. However, low temperatures ranging from 50 to 150 °C can oxidize only a few monolayers of NiO after Ni exposure to an oxygen atmosphere for 100 to 1000 h, as mentioned in Pinnel's work [48].

The process of oxidation of nickel is believed to occur through the transfer of electrons across the interface, leading to the formation of a monolayer of oxygen ions on the surface of the metal and the diffusion of oxygen anions into the metal film. Structural defects like dislocations, grain boundaries, and impurities act as nucleation sites for the growth of NiO oxide islands, which expand laterally [49]. The oxide islands rapidly grow, forming a NiO film that partially protects the Ni surface from air. The growth of the oxide film is accelerated by diffusion of Ni cations into the NiO layer at temperatures above 350 °C [50]. The penetration of oxygen into the NiO layer through cracks and microchannels is also possible, which is promoted by metal diffusion at higher temperatures. Valladares et al. [50] have studied Nickel oxidation in air, proving that the coexistence of Ni and NiO phases is detected at 400 °C and that the oxidation rate depends on the annealing temperature and on the thickness of the oxide layer. They have reported that the complete oxidation of the Ni films occurs at high temperatures such as 700 °C (See Figure 9). Thermal oxidation also affects the morphology of the film, making it granular, as can be seen in Figure 10. It is worth noting that oxidation is a self-stabilizing process at a temperature not exceeding 627 °C [49].



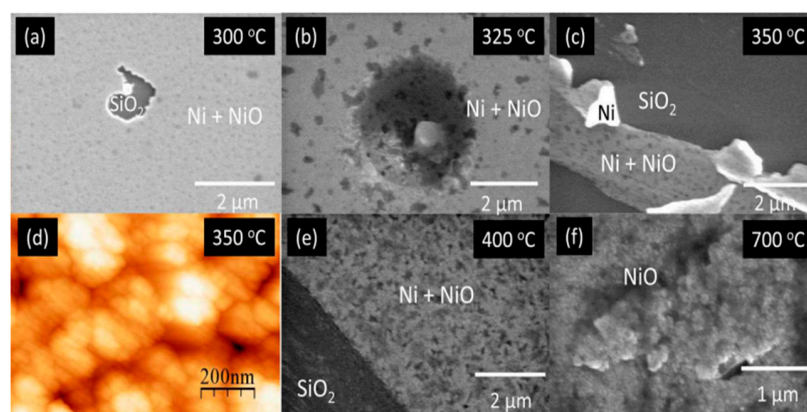**Figure 9.** (**a**–**f**) SEM images of nickel films on Si/SiO$_2$ substrates at different temperatures, (**d**) AFM image of the surface of the sample annealed at 350 °C shown in (**c**), reproduced from reference [50] AIP publishing (Copyright 2014).
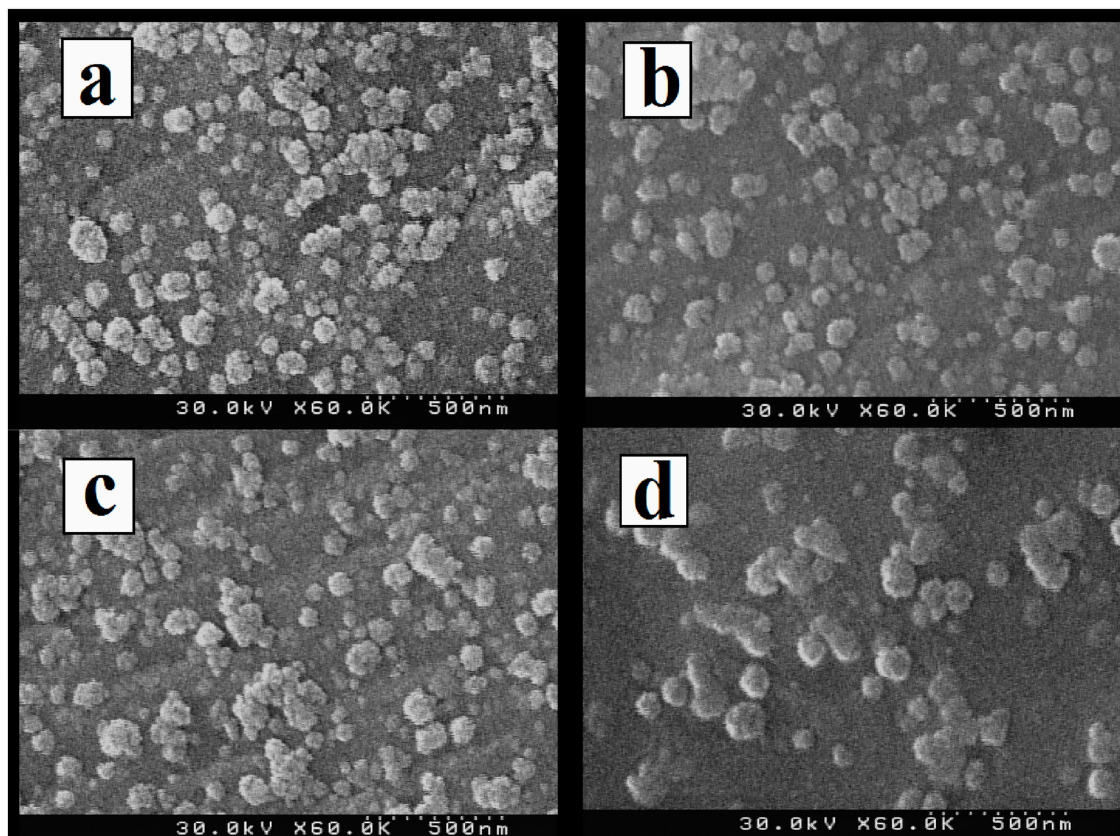
**Figure 10.** SEM imaging of NiO at different oxidation temperatures (**a**) 500 °C, (**b**) 600 °C, (**c**) 700 °C, and (**d**) 800 °C, reproduced from reference [49] Elsevier publisher (Copyright 2023).

In Table 2, we summarize the thermal oxidation conditions of NiO with associated morphologies and crystallite size that help in predicting the crystallite size and gas sensing properties.

**Table 2.** Parameters for thermal oxidation of NiO films.

| Structure | Temperature (°C) | Duration (min) | Crystallite Size (nm) | Pressure (mbar) |
|---|---|---|---|---|
| Granular films with the formation of cracks when increasing temperature [51] | 500 | 240 | 17 | NA |
| | 600 | 240 | 21 | NA |
| | 700 | 240 | 41 | NA |
| | 800 | 240 | 45 | NA |
| Cellular and porous structure [52] | 700 | ~17 | N/A | 1013.25 |
| Granular film [49] | 500 | 240 | 31 | NA |
| | 600 | 240 | 38 | NA |
| | 700 | 240 | 52 | NA |
| | 800 | 240 | 73 | NA |
| Compact morphology with columnar and facetted NiO grains [52] | 1100 | ~2000 | N/A | 1013.25 |
| Coarse-grained structure [53] | 1400 | ~1200 | N/A | 1 |
| Nanosized granular surface [54] | 400 | 60 | N/A | NA |
| Nano-rings [54] | 600 | 60 | N/A | NA |
| Slightly porous film with pseudospherical particles [54] | 800 | 60 | N/A | NA |
| Nanoplates of NiO with an average thickness of 17 nm [54] | 500 | 240 | N/A | NA |

In recent work, Dastan et al. [49] have oxidized the Ni foil at different temperatures, leading to granular films where the nanoparticles tend to agglomerate and enlarge the grain size at higher oxidation temperatures, as described in Figure 10. However, the atomic ratio is out of stoichiometry in NiO samples (oxygen-deficiency). At 800 °C, NiO is almost stoichiometric (Ni:O = 56.65:43.35) with large grains and irregular distribution on the surface.

Starting from ready Ni foil, like reference [49], nickel plates oxidized at 400 °C show nanoring-like particles predominantly composed of metallic Ni with an aggregation aspect. By increasing heating to 600 °C, the atomic ratio is close to stoichiometry, with the appearance of NiO plates not-well developed. At 800 °C, NiO crystallites are larger and indicate a slightly higher oxygen content than stoichiometric NiO (extra oxygen for charge compensation due to the formation of $Ni^{3+}$ at high temperatures) [54].

It is worthy to conclude that high oxidation temperature enhances stoichiometry for NiO, but further increases in temperature can induce the formation of $Ni_2O_3$. Also, the nature of Ni foils, the oxidation time, and additional treatment, such as immersing the Ni plate in an aqueous solution of $Ni(CH_3COO)_2$ [54] can highly influence the morphology of NiO structures, despite keeping the same oxidation temperature.

One can also note the discrepancy in NiO morphologies and crystallite size between references [49,51], despite keeping the same oxidation temperature and time, which can be related to the sputtered Ni layers on quartz substrate distinguished from Ni foils which can highly influence the morphological aspects of NiO after oxidation.

Following step-wise oxidation of Ni nanowires electrodeposited into anodic aluminum oxide (AAO) membranes, Ren et al. [55] have proved the formation of NiO nanotubes with uniform wall thickness by working in a low oxidation temperature regime and using chemical etching (See Figure 11).

In their work, the oxidation behavior of Ni nanowires was investigated, and two distinct temperature regimes were identified. The low-temperature regime was found to be driven by the field-driven oxidation mechanism and rapid vacancy diffusion, resulting in the formation of NiO–Ni heterojunctions. In contrast, the high-temperature regime (above 650 °C) was dominated by the Kirkendall effect, whereby $Ni^{2+}$ ions diffused through the oxide layer due to the thermally enhanced diffusion rate. Interestingly, the step-wise oxidation behavior of Ni resulted in the formation of bamboo-like structured NiO nanotubes due to the fast vacancy diffusion at the initial ramp-up stage of annealing. However, it was found that uniform NiO nanowires or nanotubes could not be obtained through conventional annealing/oxidation processes. Instead, a simple method was proposed for obtaining NiO nanotubes with relatively uniform wall thickness by utilizing the step-wise oxidation mechanism. This involved oxidizing Ni nanowires in the low-temperature regime (around 400 to 450 °C) followed by wet-chemical etching to remove the residual Ni metal core. Overall, these findings shed light on the complex oxidation behavior of Ni nanowires and provide a promising method for the synthesis of uniform NiO nanotubes.

Thermal oxidation is a commonly used method for growing metal oxides, as it is relatively easy to perform. However, it requires pre-fabrication of the metallic film using techniques such as sputtering or thermal evaporation. To obtain the desired morphology and physical properties of the oxide film, careful selection of parameters such as temperature, pressure, duration, and environment is crucial. The appropriate conditions for thermal oxidation must be determined to ensure successful and reproducible results. With proper control of these parameters, thermal oxidation can provide a straightforward method for growing high-quality metal oxide films.
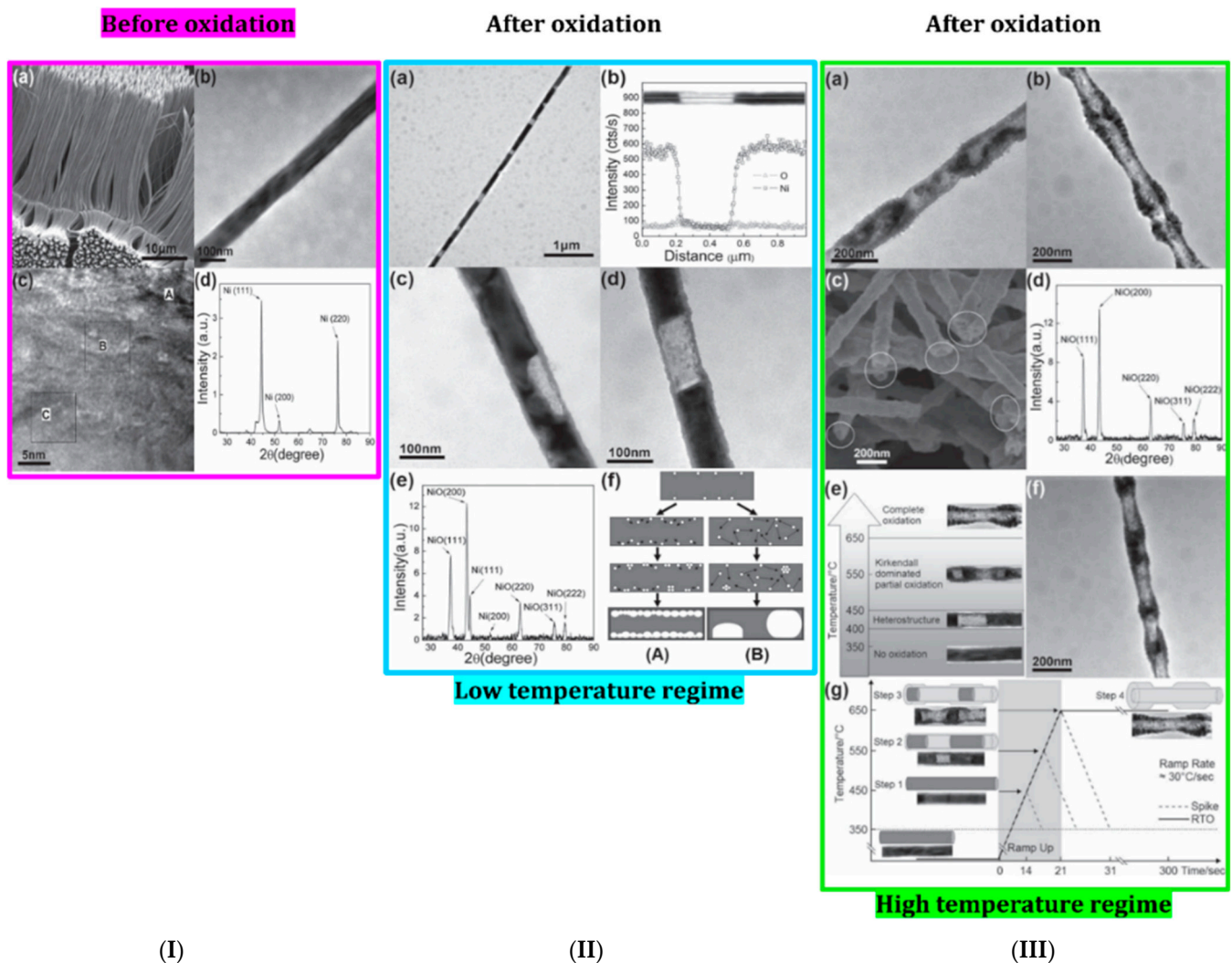
**Figure 11.** (**I**) Before oxidation: (**a**) SEM image (**b**) HRTEM image at 100 nm scale, (**c**) HRTEM image at 5 nm scale: A, B, and C represent three regions with different grain orientations and (**d**) XRD of Ni nanowires; (**II**) After oxidation at low temperature: (**a,c,d**) TEM images, (**b**) EDX mapping, and (**e**) XRD of Ni nanowires annealed at 450 °C for 10 h with (**f**) schematic of two types of (**A**) vacancy generation diffusion and (**B**) rapid diffusion of vacancies and their agglomeration during the oxidation of Ni nanowires; (**III**) After oxidation at high temperature: (**a,b,f**) TEM images, (**c**) SEM image, (**d**) XRD image, (**e**) representation of different nanowires oxidized at 550 °C and 650 °C for 5 min, respectively, (**g**) illustration of step-wise manner of Ni nanowires evolution with the ramping rate, reproduced from reference [55] John Wiley and Sons publisher (Copyright 2010).

### 2.1.4. Levitation–Jet Synthesis (LJS)

LJS is one of the advanced powder technologies that allows tuning the size, shape, and phase composition of the desired material. It is based on condensing the metal vapor in helium (argon) gas flow with injected gaseous oxygen (air) under reduced pressure. Vorotyntsev et al. have described the apparatus of levitation–jet synthesis, as illustrated in Figure 12.
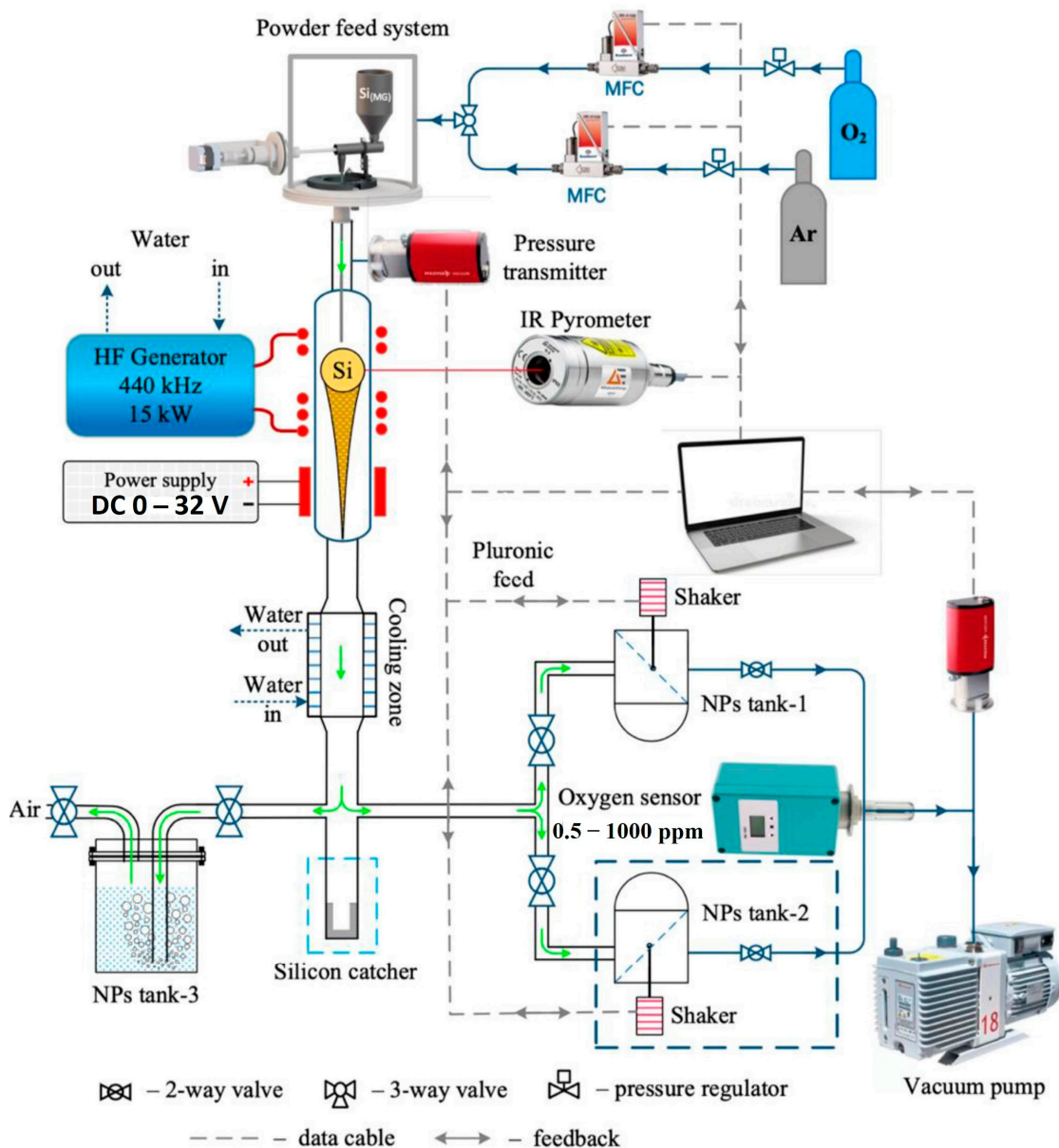
**Figure 12.** Schematic representation of levitation–jet synthesis method, reproduced from reference [56] Elsevier publisher (Copyright 2022).

The levitation–jet system is composed of a quartz tube in which the nickel wire is suspended and heated up to be melted by using a high-frequency counter-current inductor. After its evaporation, the nickel atoms will be cooled and then condensed in the particle's container with nano sizes, recovered after passing through a tissue filter. The adjustment of carrier gas flows (He (Ar)–$O_2$ (air)) plays a pivotal role in ensuring the melting, evaporation, and condensation processes to form the nickel nano-powder [57].

In fact, the condensation is governed not only by the magnitude of the applied electric field but also by the oxygen content, which in turn is undergone by the combined mode (introduced in the He (Ar) gas stream) and the post-formation of nickel atoms mode (introduced after producing the atomized nickel stream) [57].

The full regulation of the synthesis method, the capping/surfactant agent independence, and the one-pot processing make the LJS promising for material engineering by simultaneously controlling the shape and size of the metal particles.

They have compared the nanoparticles' shape by TEM characterization. Indeed, the formation of nanoparticles is primarily influenced by the electric field, which creates a

condensation zone defining the characteristic size of the particles. TEM imaging shows that the application of a field leads to a decrease in the average particle size and a narrowing of the size distribution, as well as the formation of pronounced cubic shapes in Ni nanoparticles. While spheroidal chainlike morphology dominates in nanoparticles prepared without a field, the TEM micrograph shows localized crystallization points of small cubic nanocrystals. The transition from spheroidal to cubic morphology cannot be solely attributed to the external field, but it accelerates the process. However, in a combined mode of helium–oxygen flow, a cubic shape is observed before and after the application of the electric field. This can be explained by the sufficient oxygen molecules present in the total flow of the nanoparticles' synthesis. The increase in NiO content under the external electric field was observable and was attributed to oxygen ionization processes and additional energy. The formation and evolution of oxide domains were mainly dictated by surface oxygen dynamics and strongly depended on the applied electric field, noting that more increases in the electric field lead to a more uniform surface coverage. In contrast, the activation energy barriers for ionic migration ensured lower oxygen surface mobility at zero field.

Figure 13 represents TEM images of Ni/NiO nanostructures prepared by the LJS method with cubic morphology and average particle sizes (<100 nm).
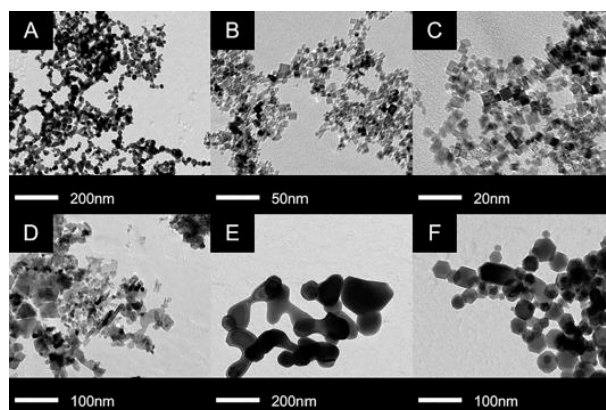


**Figure 13.** TEM micrographs of LJS-prepared Ni/NiO nanoparticles at different conditions: (**A**): He—500 L/h, Ni—1 g/h, (**B**): He—1000 L/h, O$_2$—200 L/h, Ni—1 g/h, (**C**): He—1000 L/h, O$_2$—100 L/h, Ni—0.4 g/h, (**D**): commercial NiO, (**E**): commercial NiO (Aldrich), (**F**): He—500 L/h, air—9 L/h, Ni—2 g/h, Fe—3.5 g/h, reproduced from reference [58] Elsevier publisher (Copyright 2019).

### 2.1.5. Molecular Beam Epitaxy

Molecular beam epitaxy (MBE) is a unique technique for synthesizing high-quality oxide thin films and heterostructures that is dedicated to fundamental studies and fabrication of nanoscale devices. This growth method has recently been adapted to the realization of diverse multicomponent oxide materials. Initially, MBE systems were designed for the growth of semiconducting compounds. However, over time, the technique was modified for the deposition of metals and insulators as well. Due to the use of ultrahigh vacuum chambers in the MBE process, the highest level of material purity is attained, and in situ surface-sensitive tools are available for monitoring the growth process. In recent times, MBE has been further adapted to enable the synthesis of oxides and nitrides by introducing suitable reactive gases into the growth chamber [59]. Regarding its working principle, the method utilizes an ultrahigh vacuum chamber in which a beam of atoms or molecules is directed toward a heated substrate. The substrate temperature is precisely controlled to ensure that the incoming atoms or molecules condense onto its surface, forming a single crystal layer with precise thickness and orientation. MBE typically employs one or more effusion cells or valved sources, which are used to produce atomic or molecular beams. By adjusting the relative fluxes of the beam species, the composition of the growing film can

be precisely controlled. The MBE process also allows for in situ monitoring of the growth process using various surface-sensitive techniques, such as reflection high-energy electron diffraction (RHEED) or Auger electron spectroscopy (AES), enabling real-time feedback control of the deposition process. The formation of the correct phase, the presence of long-range crystallinity, and the coherence of the film/substrate interface are very important in the growth of metal oxides.

Budde et al. have used plasma-assisted MBE to prepare NiO and on (00.1)-oriented gallium nitride templates, consisting of $\alpha$-Al$_2$O$_3$ substrate, AlN buffer layer, and GaN layer, under oxygen-rich conditions at different growth temperatures [60].

Ni epitaxial films have been deposited on (001) MgO substrates [61] by MBE at a temperature of 300 °C. The experimental results showed that Ni grows epitaxially on MgO, with a cube-on-cube orientation relationship from the early stages of growth, as confirmed by RHEED. Interestingly, we also observed a weak uniaxial anisotropy in the epitaxial Ni growth, although not as strong as in the (001) case. The origin of this anisotropy is not fully understood yet, but it could be related to surface features such as steps or screw dislocations or shape anisotropy. It is worth noting that there is no effect of NiO distortion in this configuration, as it should be perpendicular to the (111) plane. These findings provide valuable insights into the epitaxial growth of Ni on MgO and its potential applications in various fields.

Co-deposition is also allowed in the MBE setup, where the oxide components were evaporated from the individual sources simultaneously. For instance, lanthanum nickel oxide is grown by deposition of both nickel and lanthanum at the same rate to ensure the correct stoichiometry [62].

The phase formation process results from a chemical reaction between the evaporated Ni and La atoms and the oxygen species at the surface of the substrate. When a coherent interface is established, the lattice mismatch between the substrate and the epitaxial film can generate several strain states and may result in the formation of metastable compounds. As the nickel has different oxidation states, the LaNiO$_3$ phase diagram is dependent on it. So, the adjustment of pressure and temperature should be appropriately made to avoid the film decomposition into NiO and La$_2$NiO$_4$ due to low (high) pressure (temperature) that shift the chemical equilibrium of the oxidation reaction toward lower oxidation states and may reduce the adatoms' mobility resulting in island growth mode that increases the surface roughness and generates more structural defects when lowering the growth temperature [63].

### 2.1.6. Metal–Organic Chemical Vapor Deposition

The metal–organic chemical vapor deposition (MOCVD) process begins with the preparation of a substrate, which is typically a silicon wafer or a glass slide. The substrate is first cleaned to remove any impurities and then coated with a thin layer of a metal-organic precursor. This precursor is typically a volatile organic compound containing the metal of interest, such as metal alkoxides, beta-diketonates, or metal carboxylates. The reactor is then heated to a high temperature, typically between 400 and 900 °C, to decompose the metal-organic precursor and produce the metal oxide film on the substrate (the decomposition can occur thermally, photochemically, or by plasma). During the deposition process, the metal oxide film grows layer by layer on the substrate, with the thickness of the film controlled by the duration of the deposition process. The growth rate and thickness of the film can be controlled by adjusting the temperature, pressure, and flow rate of the reactants [64–68]. One of the advantages of MOCVD is its ability to produce high-quality metal oxide films with precise control over the thickness and composition of the film. The process also allows for the growth of complex metal oxides with tailored properties, such as multi-layered films, alloys, and doped materials. In addition, the use of metal-organic precursors allows for the growth of films at lower temperatures, reducing the risk of substrate damage. However, MOCVD also has some limitations. The technique requires a high level of expertise and specialized equipment, which can be expensive

to maintain. Additionally, the process can be time-consuming, with typical deposition times ranging from a few minutes to several hours. Lo Nigro et al. [69] have fabricated epitaxial NiO thin films on an AlGaN/GaN template using Metal Organic Chemical Vapor Deposition (MOCVD) at two different temperatures (500 °C and 750 °C) and a range of oxygen flow values (50 to 500 sccm). A nickel β-diketonate adduct known as Ni(tta)2.tmeda was the precursor introduced in an alumina boat and heated at 160 °C. Its vapors were transported to the deposition chamber using 150 sccm of Ar flow and different lows of oxygen with an operative pressure of 399.97–533.29 Pa and time deposition of 20 min. The resulting films were found to be uniform in thickness, adherent, and possess smooth surfaces. Varying deposition temperatures and oxygen flow values led to morphological differences in the films. The optimized deposition conditions were determined to be a deposition temperature of 500 °C, 200 sccm oxygen flow, a 45° tilted substrate position, and a slow cooling rate of 1 °C/min post-deposition. XRD and TEM analyses revealed that the films were epitaxial and exhibited a high-quality film/substrate interface, as shown in Figure 14. These findings provide insights into the fabrication of high-quality NiO films for potential applications in various electronic devices.
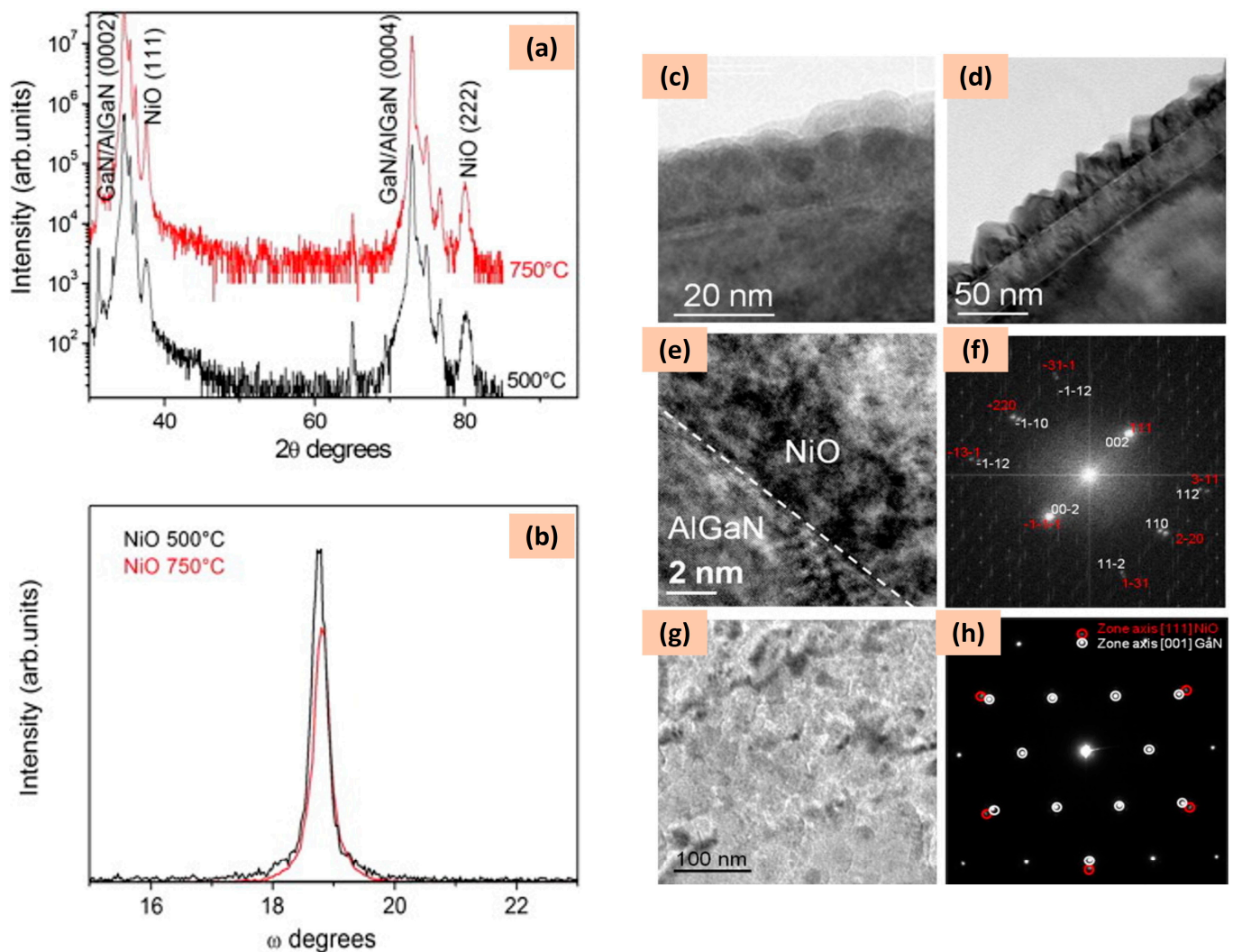


**Figure 14.** (**a**,**b**) XRD patterns of NiO deposited on AlGaN/GaN at 500 °C and 750 °C and TEM cross-sections of NiO films grown at (**c**) 500 °C and (**d**) 750 °C, (**e**) High resolution TEM image of the NiO/AlGaN interface and (**f**) its relative Fast Fourier Transform image, (**g**) TEM in-plane image of NiO deposited at 500 °C, (**h**) relative electron diffraction patterns from the substrate (white circles) and from the NiO film (red circles), reproduced from reference [69] Elsevier publisher (Copyright 2014).

### 2.1.7. Atomic Layer Deposition

As the MOCVD technique mentioned above requires extremely high temperatures and involves toxic and volatile substances, another chemical process is introduced and known as atomic layer deposition (ALD). This deposition can be a good opportunity to use substrates that cannot withstand high temperatures. This thin film deposition is based on sequential surface reactions between precursor gases and the substrate surface. In ALD, the substrate is exposed to a pulse of precursor gas, which chemically reacts with the surface. After the reaction, the unreacted precursor is purged from the reaction chamber using an inert gas. The substrate is then exposed to a second pulse of a different precursor gas, which reacts with the remaining unreacted sites on the surface. The process is repeated in a cyclic fashion until the desired film thickness is achieved.

ALD is a highly controlled and precise technique that can be used to deposit a wide range of thin films, including metal oxides, nitrides, and other materials. The technique is particularly useful for depositing films with high uniformity, conformality, and purity. The thickness of the film can be precisely controlled at the atomic level by adjusting the number of deposition cycles. One of the major advantages of ALD is its ability to deposit films with excellent conformality, even on complex three-dimensional structures with high aspect ratios. This is due to the self-limiting nature of the surface reactions, which ensures that the thickness of the film is determined by the number of reaction cycles rather than the thickness of the film deposited in each cycle. ALD can also be used to deposit films with controlled composition, enabling the precise tuning of material properties [70].

Figure 15 represents the ALD process to grow alumina film from trimethylaluminum (TMA) and water [71].
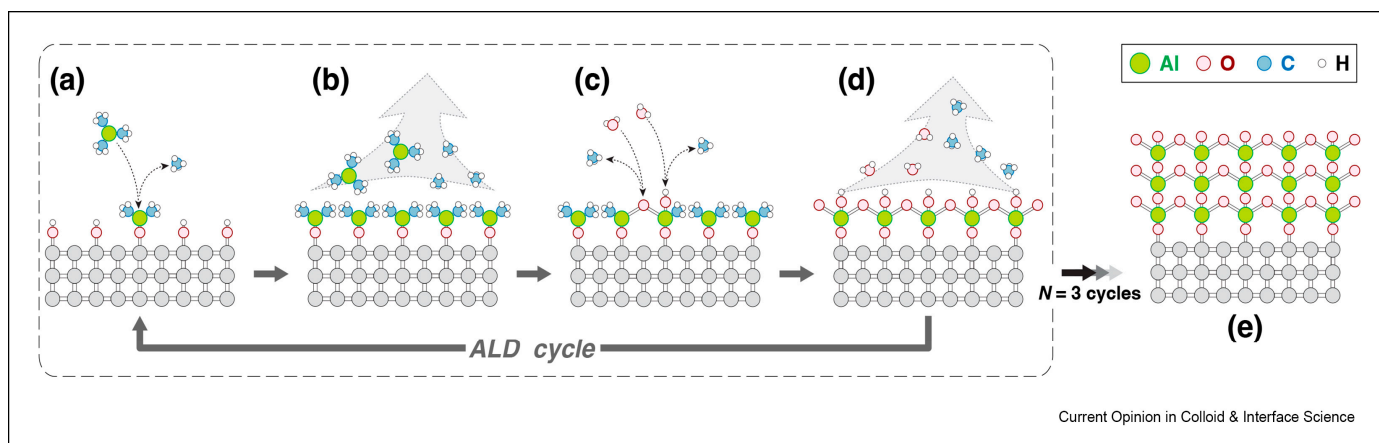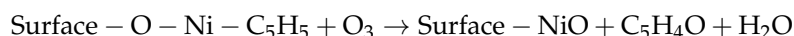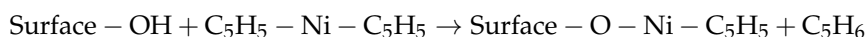


**Figure 15.** ALD process of alumina: (**a**) pulse of the precursor (trimethylamine) and chemisorption process, (**b**) purging and pumping of the by-products (excess of precursor), (**c**) pulse of $H_2O$ molecules reacting with the remaining precursor ligands, (**d**) purging and pumping of the by-products (excess of water molecules), and (**e**) the alumina surface after three cycles of ALD, reproduced from reference [71] Elsevier publisher (Copyright 2023).

ALD has found widespread use in a variety of applications, including gas sensors. Pan et al. [72] have deposited ultrathin films of sub-50 nm NiO on $SiO_2/Si$ wafers to enhance the detection of triethylamine (TEA). The deposition is based on the following chemical reactions:

$$Surface - OH + C_5H_5 - Ni - C_5H_5 \rightarrow Surface - O - Ni - C_5H_5 + C_5H_6$$

$$Surface - O - Ni - C_5H_5 + O_3 \rightarrow Surface - NiO + C_5H_4O + H_2O$$

They have reported a nanometric film of NiO with a large number of closely aggregated nanoparticles, observed by SEM imaging, giving an undulating aspect to the surface whose

roughness is measured by AFM to be 0.874 nm. In addition, TEM imaging revealed a high crystallinity of $Ni_2O_3$ along (002) with a lattice spacing of 0.28 nm.
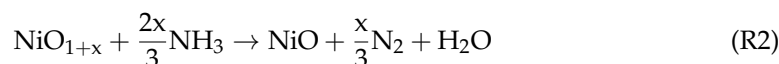
*2.2. Liquid-Phase Deposition*

The liquid film deposition has been developed as a quick, simple, low-cost, easy scaling up, uniform, less hazardous, and a non-vacuum required route for thin film coating. The most used and emerging techniques are chemical bath deposition, electrodeposition, electrospinning, spin coating, dip coating, spray coating, and inkjet printing, described in the following.

2.2.1. Chemical Bath Deposition (CBD)

Forming solids from a solution or a gas using an aqueous precursor solution is realizable thanks to the chemical bath deposition. This method is based on immersing the substrate in a liquid solution containing the precursor material, where chemical reactions are responsible for depositing the thin film onto the substrate. The chemical reactions can be initiated by heat, light, or other chemical agents [73–75].

The solution for CBD of NiO reported in the literature [76] was prepared by mixing 40 mL of 1 M nickel sulfate, 30 mL of 0.25 M potassium persulfate, 10 mL of 28–30% aqueous ammonia, and 20 mL of deionized water using a 5 cm magnetic stir bar rotating at 200 rpm, at room temperature. The initial reaction, denoted as reaction 1, comprised the deposition of nickel oxide with a higher valency state. This resulted in the formation of mixed valency states, specifically, valency states 2 and 3. The subsequent step, reaction 2, involved the reduction of the higher valence nickel species by ammonia to attain the normal oxidation state. This process demonstrated the ability to manipulate the oxidation state of nickel species using simple chemical methods.

$$NiSO_4 + xK_2S_2O_8 + 2x(1+x)OH^- \rightarrow NiO_{1+x} + xK_2SO_4 + (1+x)SO_4^{2-} + (1+x)H_2O; \qquad (R1)$$

$$NiO_{1+x} + \frac{2x}{3}NH_3 \rightarrow NiO + \frac{x}{3}N_2 + H_2O \qquad (R2)$$

Microstructural analysis of the deposited NiO demonstrates the deposition of 180 nm-thin film showing porous structure, which is well defined after annealing.

2.2.2. Electrodeposition

Electrodeposition is a widely used technique for the synthesis of various materials, and it involves several steps, including the transport of the metal ions to the electrode surface, their reduction at the electrode, and the formation of a metal deposit on the electrode surface. The mechanism of electrodeposition is highly dependent on the reaction conditions, such as the type of electrolyte, electrode potential, current density, and deposition time. The initial step of electrodeposition is the transport of the metal ions to the electrode surface. The metal ions can be transported by diffusion or migration under the influence of an applied electric field. The diffusion mechanism depends on the concentration gradient of the metal ions, whereas the migration mechanism depends on the electrical field strength and the charge of the metal ions. Once the metal ions reach the electrode surface, they are reduced to form a metallic deposit. The reduction of the metal ions occurs through the transfer of electrons from the electrode to the metal ions, resulting in the formation of a metal atom or cluster on the electrode surface. The reduction process can be influenced by the electrode potential, which is the electrical potential difference between the electrode and the electrolyte. The electrode potential can affect the kinetics and thermodynamics of the reduction reaction, leading to changes in the morphology and properties of the deposited material [77,78]. The deposition time also plays a crucial role in the electrodeposition mechanism. It affects the amount and thickness of the deposited material, as well as its uniformity and morphology. Long deposition times can lead to the formation of larger

and more complex structures, whereas short deposition times can lead to the formation of thinner film but with non-uniform coverage, whether the growth time is insufficient [78–80].

Zhang et al. [81] have employed this technique to grow NiO nano-flowers on an ITO glass substrate. The electrodeposition was performed at a constant current ($-0.5$ mA) using a three-electrode setup, with the ITO glass as the working electrode, nickel plate (99.9 wt%) as the counter electrode, and saturated calomel as the reference electrode. The electrolyte contained 0.05 mol/L $NiSO_4 \cdot 6H_2O$ (pH = 5) and deionized water as the solvent. The NiO film was deposited for a duration of 200 s at $20 \pm 3\,°C$. The final deposits were rinsed with ethanol and deionized water, oxidized at $350\,°C$ for 2 h in air, and then allowed to cool to room temperature naturally to form the rose-type structure NiO nanoparticles [81].

Shahzad et al. [82] have also used electrodeposition to prepare NiO film. The synthesis of one-dimensional nickel nanowires (Ni-NWs) using anodic aluminum oxide (AAO) templates is described in Figure 16. The electrolyte solution used for the electrodeposition process was prepared by dissolving nickel sulfate hexahydrate in deionized water to make a 1 M solution, which was buffered with 0.2 M boric acid and adjusted to pH = 3 with 0.1 M sulfuric acid. The Ni-NWs were electrodeposited by using a pure nickel wire as the anode and the coated side of the AAO template as the cathode, with a pure Cu sheet attached to the backside of the conducting layer for support and electric current. The deposition time was fixed at 120 min, and the deposition potential and current density were adjusted to 2.1 V and 1.5 $mA/cm^2$, respectively. The green color in Figure 16a represents the development of pure Ni-NWs grown preferably along (220) orientation as proved by XRD (See Figure 16b), which were formed because of the reduction of $Ni^{2+}$ ions in the electrolyte and their deposition into the pores of the AAO template.
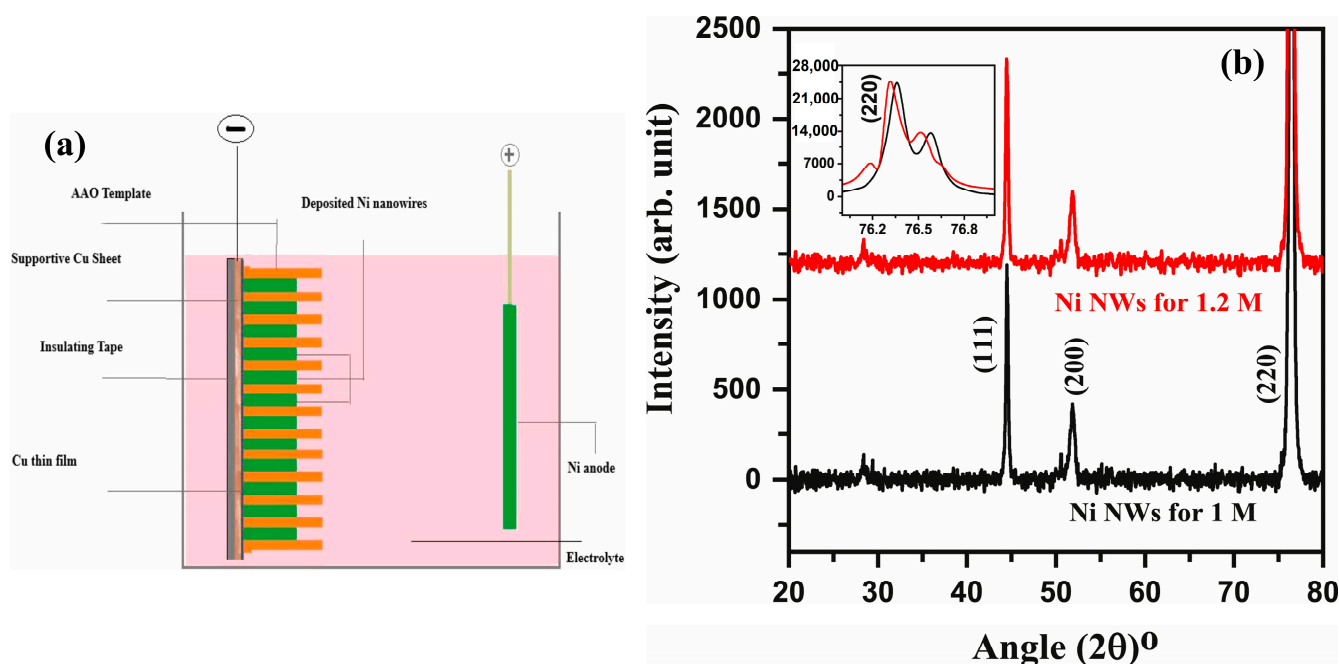


**Figure 16.** (**a**) Electrodeposition setup for NiO synthesis on AAO template characterized by (**b**) XRD, reproduced from reference [82] Elsevier publisher (Copyright 2023).

2.2.3. Electrospinning

The electrospinning process has emerged as a technique used for the growth of fibers at submicron to nanometer scales. It involves the use of an electric field to generate a charged polymer solution, which is then ejected through a spinneret to produce a jet of fluid. The jet is then subjected to an electric field that causes the formation of a Taylor cone, from which a charged droplet is ejected. As the droplet moves towards the collector, it undergoes stretching and bending due to the electric field, causing the formation of fibrous

material which is collected on a substrate, forming a nanofiber mat [83]. By incorporating metal oxide precursors into the polymer solution, metal oxide nanofibers can be produced by electrospinning. Calcining the as-spun nanofibers can introduce pores and increase the specific surface area [84], making them suitable for gas sensing.

The electrospinning process is influenced by several parameters that can affect the morphology and characteristics of the resulting nanofibers. These parameters include the polymer solution properties (viscosity, surface tension, conductivity), the electrospinning conditions (applied voltage, distance between the spinneret and collector, and flow rate of the polymer solution), the environmental factors (higher temperature and lower humidity can lead to faster solvent evaporation and smaller fiber diameter). The design of the electrospinning apparatus, such as the shape and size of the spinneret and collector, can also influence the as-spun material. Different designs can produce different morphologies of nanofibers. Optimizing these parameters is important for controlling the morphology and properties of the nanofibers and for achieving the desired characteristics for specific applications.

The electrospinning process for the growth of metal oxide nanofibers typically involves the electrospinning of metal precursor with a carrier polymer to obtain salt/polymer structure, followed by calcination of the as-spun materials in air to remove the polymer from the metal oxide fibers. During the first step, the metal precursor is typically dissolved in a polymer solution, and an electric field is applied to create a charged jet of the solution that is collected on a substrate to form nanofibers. The resulting nanofibers are then heated in air to remove the polymer and convert the metal precursor into a metal oxide. The calcination process can be optimized to control the morphology and properties of the metal oxide with fibrous morphology [83]. In an interesting work, Ercolano et al. [85] have prepared one-dimensional Ni-based as-spun nanofibers using different Ni precursors, carrier polymers, solvents, target distances at different voltages and flow rates, thermally treated in various atmospheres. They have obtained nickel with possible phases of nickel oxide, nickel nitride, metallic nickel, nickel/carbon, and other mixed phases and possible structures such as nanoribbons, nanofibers, and sponge-like architecture. Figure 17 shows the SEM pictorial representation of different structures at different experimental conditions.

The nickel nitrate used as Ni precursor dissolved in water/ethanol using poly(vinyl alcohol) (PVA) polymer demonstrated an average diameter of 58 nm for the nanofibers, which is three-fold smaller than the fibers prepared in other solvents and can be explained by the high dynamic viscosity, the high surface tension, and the high conductivity of the solution (water/ethanol). The calcination in air allowed the formation of NiO nanofibers from Ni/salt polymer. However, there is an alternative process to modify their morphological aspect, which is the reduction process and the thermal decomposition at high temperatures to change the NiO into $Ni_3N$ for investigation in supercapacitors, Li-ion batteries, and photovoltaic applications [86].

In another experiment, a PolyVinylPyrrolidone–Nickel acetate (PVP)/$Ni(CH_3COO)_2$ solution was electrospun to fabricate NiO nanofibers on a glass substrate. The electrospinning was performed using a syringe pump to continuously provide the PVP/$Ni(CH_3COO)_2$ solution at a flow rate of 20 L/h. A high voltage of 9 kV was applied to the nozzle, and a grounded steel substrate was used as the cathode for the electrospinning process. A glass slide with patterned Au electrodes was attached to the steel substrate to collect the electrospun nanofibers. After collection, the nanofibers were sintered in air at 480 °C for 1 h to remove the PVP and obtain NiO nanofibers on the glass substrate, devoted to gas sensing application [87].
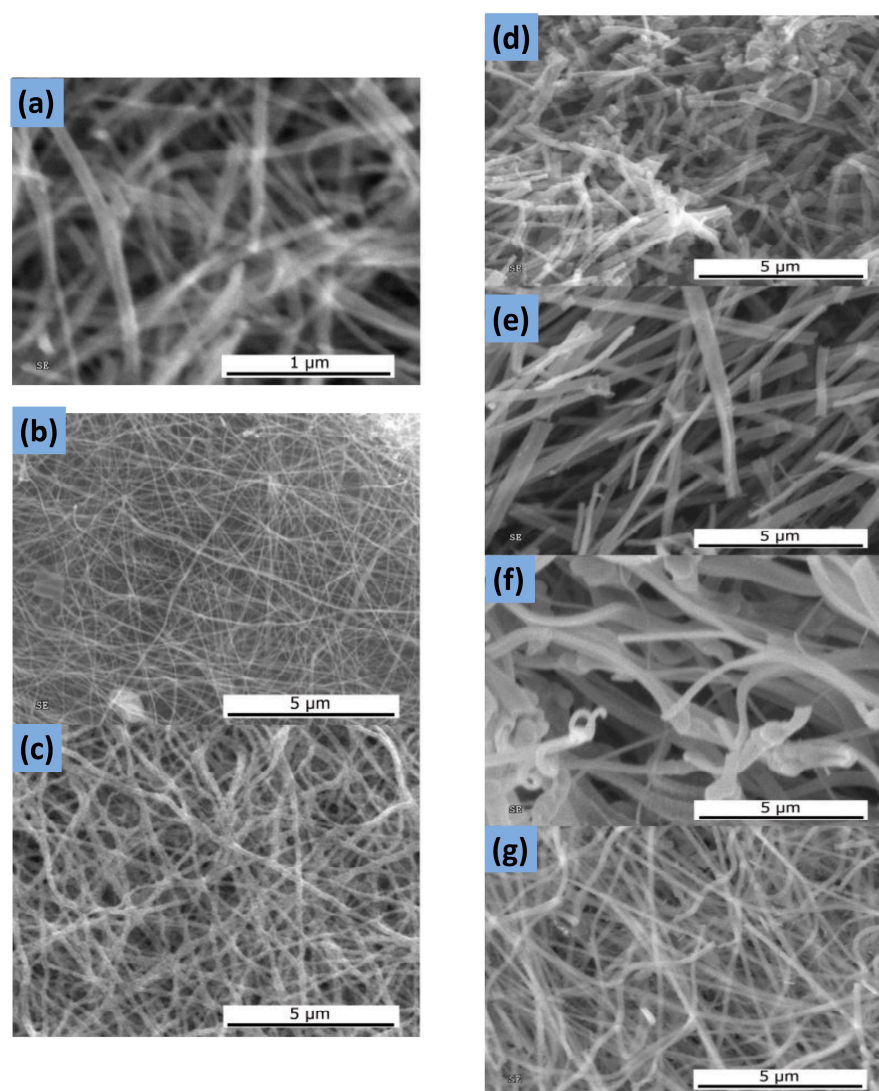
**Figure 17.** SEM micrographs of (**a**) 12 wt% PVA and 12 wt% nickel acetate in water, (**b**) 11 wt% PVA and 11 wt% nickel nitrate in water/ethanol and (**c**) 9 wt% PVA and 9 wt% nickel nitrate in DMF/ethanol, (**d**–**f**) 9, 10, 11 wt% PVP and 9, 10, 11 wt% nickel acetate in pure ethanol and (**g**) 10 wt% PVP and 10 wt% nickel acetate in ethanol:DMF (7:3 vol) prepared by electrospinning, reproduced from reference [85] MDPI publisher (Copyright 2016).

Electrospinning of NiO was also investigated by using a slurry poured into a clinical syringe connected to a needle and collector. The collector was a copper wire mesh, and an electric field was generated between the needle and the mesh. The fibers were formed between the needle and collector at a voltage of 18 kV for 1 h. The resulting fiber films were sintered at temperatures ranging from 500 to 1400 °C. Factors such as viscosity, conductivity, and surface tension of the precursor solution could affect the fiber morphology by changing the diameter. The nanoparticle and polymer content in the solution were varied, while the concentration of nanoparticles was adjusted between 0 and 2 wt% with PVP content of 6 wt%. Figure 18 represents four SEM images of the nanofiber film of NiO-8YSZ using different nanoparticle contents [88].
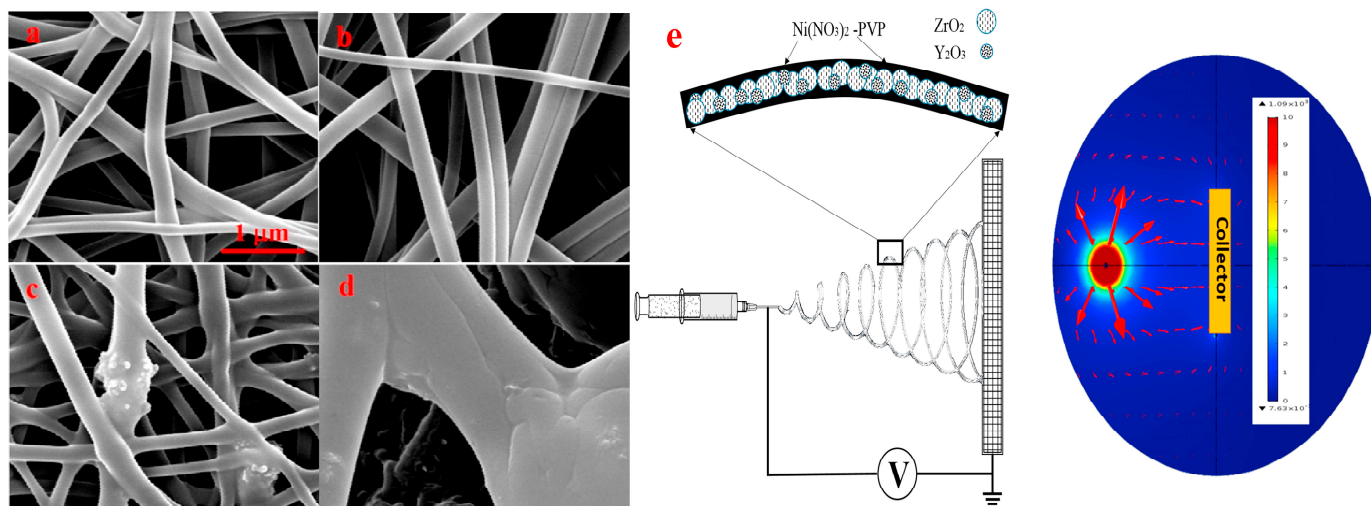
**Figure 18.** SEM microstructures of nanofiber film with different nanoparticle contents: (**a**) 0 wt%, (**b**) 0.5 wt% and (**c**) 1 wt% and (**d**) 2 wt%, prepared by (**e**) electrospinning method (schematic illustration), reproduced from reference [88] Elsevier publisher (Copyright 2017).

### 2.2.4. Spin Coating

Spin coating is a liquid-deposition technique that involves the application of a liquid precursor material onto a substrate, followed by spinning the substrate rapidly to spread the liquid precursor material evenly over the substrate surface. The spinning process helps to remove excess solvent and create a uniform thin film. The widespread use of spin coating in nanotechnology and organic electronics refers to its quick and simple processing to apply a uniform thin film to substrates. Its working area ranges from a few millimeters square to one meter square or more. The film thickness varies from a few nanometers to a few microns. Its general concept is based on dispensing the precursor solution at high speed over the edge of a solid surface driven by the centrifugal forces, the viscous forces, and the surface tension forces. Once the solution is spread and evaporated, we obtain a uniform coating of the substrate by a thin film of 1–10 µm in thickness [62].

There are three main stages governing the spin coating process and repeated several times to coat the substrate: (1) static/dynamic spin deposition, (2) Spin up and off, and (3) evaporation.

Indeed, the solution is suspended onto the substrate, which is already spinning (dynamic) or set on spin after the deposition (static). By speeding up the rotation disc with well-defined velocity and making the solution also spin at different rates, the centrifugal forces balance the rotational acceleration, resulting in producing a fluid layer driven by viscous forces, which fling off the substrate surface and is influenced by interference phenomenon that changes the film color and reveals the dry aspect. Thereby, the evaporation of the solvent occurs to enable the thinning of the coating, depending on the temperature, pressure, and volatility of the solvent.

Haider et al. [89] have prepared the NiO colloid by sol–gel method to be deposited on a glass substrate via spin coating at 3000 rpm for 40 s, followed by thermal annealing at 450 °C and 500 °C of two thin films of 120 nm in thickness, [15–30 nm] in grain size and [8–12 nm] in roughness coefficient. The schematic of their spin coating of NiO is shown in Figure 19.
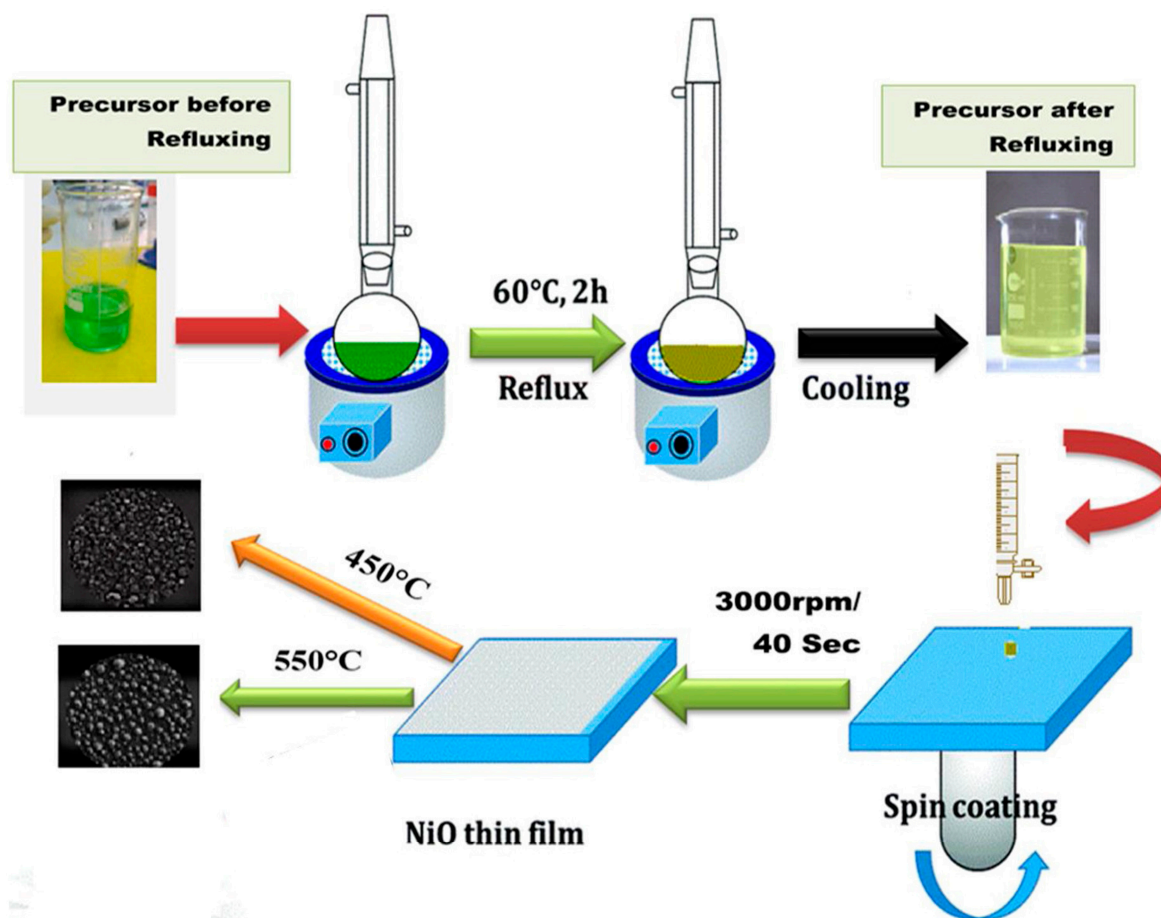
**Figure 19.** Spin coating of NiO thin film on glass substrate reproduced from reference [89] Elsevier publisher (Copyright 2019).

Using the same technique, Chtouki et al. investigated NiO thin film deposited on a glass substrate at 3600 rpm for 30 s, dried at 150 °C for 15 min, and annealed at 350 °C for 45 min. Its microstructural analysis reveals a cubic phase crystallinity and a roughness coefficient of 7.76 nm [90].

The deposition of nickel oxide (NiO) was carried out by two methods: thermal evaporation and spin-coating. For thermal-NiO, NiO granules were evaporated at a low deposition rate under high vacuum conditions to deposit a 5 nm thick film. The thermal-NiO was grown with different thicknesses. Spin-NiO, on the other hand, was deposited by spin-coating a solution of NiO nanoparticles and annealing the film at 300 °C for 30 min in air. The microstructural analysis of the two grown-NiO is shown in Figure 20, proving a higher surface area of spin-NiO than that of thermal-NiO. These deposition techniques and thickness optimization studies are important for improving the structural properties of NiO and its performance [91].

Despite the fast, sharp, and low-cost deposition of a uniform thin film with good quality, spin coating is unfit for large substrates due to the difficult spinning at high speeds and still suffers from the lack of material efficiency; the coating defects related to centrifugal forces, the high solubility of the layers after the deposition of a multi-layered film, etc. [92].
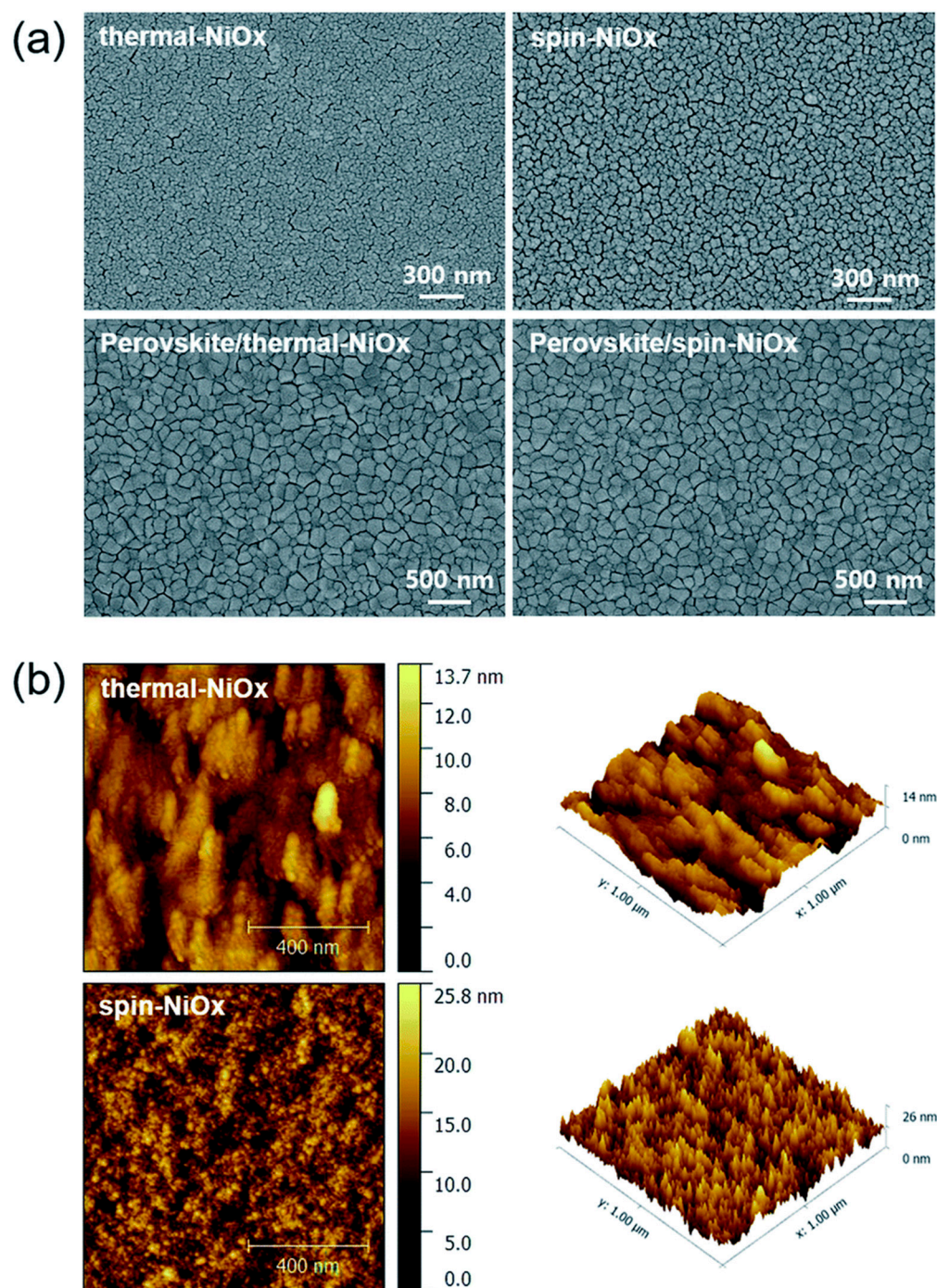
**Figure 20.** Comparative representation of thermal-NiO and spin-NiO morphologies using (**a**) SEM and (**b**) AFM microscopes reproduced from reference [91] Royal Society of Chemistry publisher (Copyright 2020).

### 2.2.5. Dip Coating

Dip coating is a widely used and versatile coating method in both laboratory and industrial settings. The process involves immersing a substrate into a solution containing the precursor of the desired material and then withdrawing it at a controlled rate. This results in the deposition of a liquid phase onto the surface of the substrate, which is then evaporated to create a dry film. The thickness and morphology of the film depend on various factors, including substrate surface, solution density and viscosity, surface tension, immersion time, withdrawal speed, dip-coating cycles, and evaporation conditions. Photo-

assisted dip-coating is also used to control the evaporation process and improve film disposition. The process typically involves four stages: immersion, dwelling, withdrawal, and drying, as shown in Figure 21. It is worth noting that withdrawal and drying stages are critical for determining the properties of the final film, as different sets of forces (entraining forces and draining forces) interact with the solution residues on the substrate surface. In addition to the conventional dip-coating technique, photo-assisted dip-coating is utilized to improve the control over the evaporation process of the coated solution and facilitate the film disposition. Multi-layered dip-coating is also applied to increase the uniformity and thickness of the film [62,93].
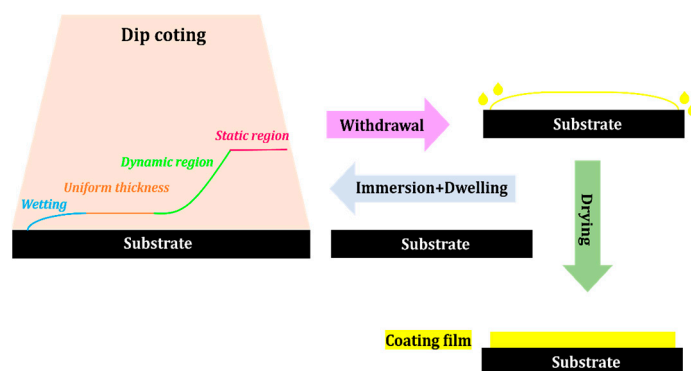


**Figure 21.** Schematic representation of dip coating process.

Simiari et al. has deposited NiO on a glass substrate via the dip coating method [94]. They dissolved 2.489 gr of nickel acetate tetrahydrate ($C_4H_6NiO_4\cdot4H_2O$) in 20 mL of 2-methoxyethanol at 70 °C for 15 min. Then, they immersed the substrate vertically and removed it out of the solution several times at a speed of 100 mm/min. The deposited film was dried at 300 °C for 15 min each cycle until it reached the desired thickness, and then it was annealed in an air environment for 1 h at 600 °C. The roughness, the wetting behavior, and the crystallinity of the coating film are investigated in reference [94]. The AFM allows measuring the surface roughness of NiO film RMS = 6.57 nm. The wettability of NiO was also studied, proving a hydrophilic characteristic as the water contact angle is 57° < 90°. The XRD patterns show a cubic structure with crystal lattice planes of (111), (200), and (220), in good agreement with JCPDS No.73–1519.

### 2.2.6. Spray Coating

Spray coating is a versatile and widely used technique in the field of materials science for depositing thin films of metal oxide onto a substrate. The process involves the atomization of a metal oxide precursor solution into fine droplets, which are then directed onto a substrate by means of a spray gun utilizing a jet stream of carrier gas. The evaporation of the solvent in the droplets is linked to several factors. The rate at which they dry depends on variables such as the size of the droplets, the boiling point of the solvent within them, the temperature of the substrate, and the environmental conditions of the surrounding air. These elements collectively dictate the time it takes for the droplets to transition from a liquid to a solid state, thereby influencing the final characteristics of the thin film coating that is formed [95].

Spray coating is a highly controllable and adaptable process that can be used to deposit metal oxide coatings onto a wide range of substrate materials, including glass, ceramics, and metals. It is commonly used in the production of a range of functional coatings, including photocatalytic, anti-corrosion, and gas-sensing coatings. Some of the critical parameters that impact the spray coating process can be the precursor solution composition, solvent type and properties, spray parameters, substrate properties, distance from the nozzle to the substrate, etc. [95–97].

The spray deposition method, such as electrostatic spray, ultrasonic spray, or airbrush spray, can also influence the coating's morphology, thickness, and uniformity.

Desai et al. have prepared NiO with a thickness of 530 nm by spray pyrolysis technique using nickel nitrate as precursor dissolved in water to be deposited on ITO-coated glass heated at 370–420 °C following four steps: (i) separation of water from Ni nitrate; (ii) partial decomposition of Ni nitrate; (iii) decomposition to oxide; (iv) decomposition of oxide to nickel oxide. The optimization of the spray parameters for the preparation of NiO film led to a substrate temperature of 460 °C, an aqueous solution concentration of 0.1 M, a nozzle-to-substrate distance of 25 cm, a total spray time of 210 s, and a solution flow rate of 10 mL/min in an air carrier gas environment at 250 kPa [98]. J.D. Desai used the same spray technique to deposit NiO film by changing the precursor to nickel acetate [97]. Using the nickel acetate as precursor demonstrates good coverage of the whole surface of the substrate by smooth NiO, whereas the use of nickel nitrate reveals closely packed, nanosized grains with irregular shapes but nearly uniform sizes, which is rougher than the latter one. Each research work shows the cubic phase of NiO (Bunsenite). However, the use of nickel acetate precursor results in a coating film 165 nm thinner than the film prepared by nickel nitrate precursor (530 nm).

The XRD patterns and SEM image are shown in Figure 22, proving the cubic crystallinity of the NiO film.
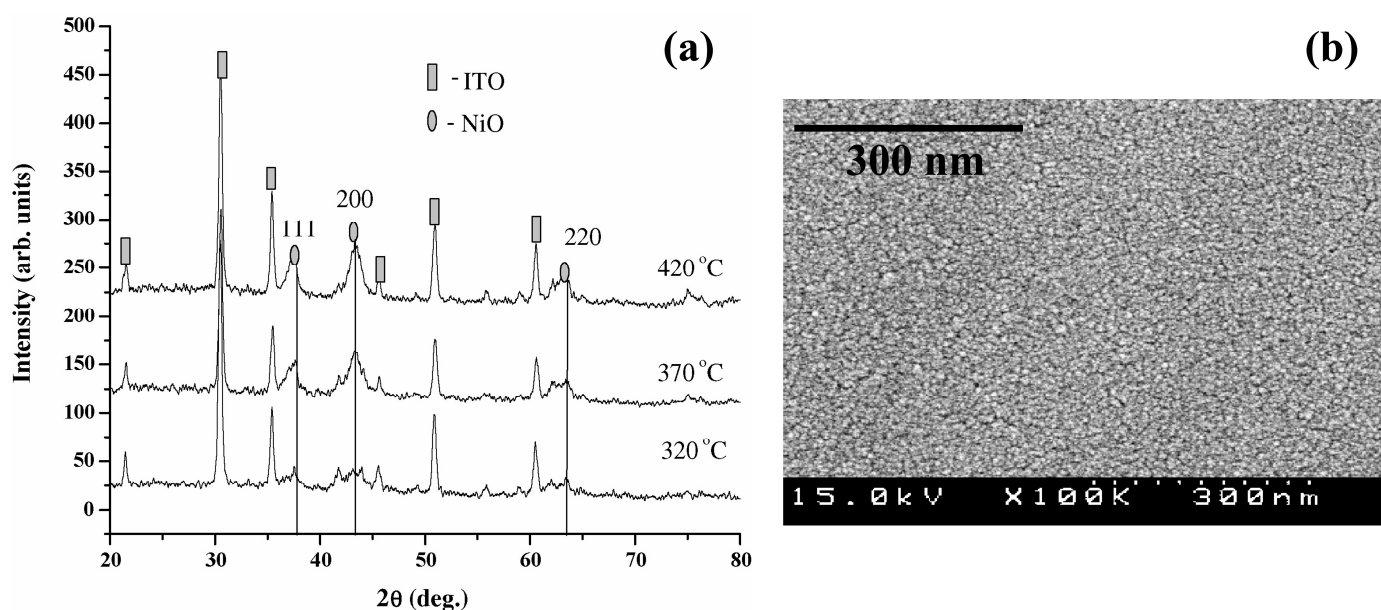


**Figure 22.** (**a**) XRD patterns and (**b**) SEM image of NiO coating film using nickel acetate as precursor reproduced from reference [98] Elsevier publisher (Copyright 2006).

The properties of the resulting coatings can be finely tuned by adjusting the composition of the precursor solution, the spray parameters, and the annealing conditions. By controlling these parameters, researchers can tailor the properties of the metal oxide coatings to achieve the desired functionality for various applications.

### 2.2.7. Inkjet Printing

Growing films over large areas is one of the most advantageous properties of inkjet printing technology, compared to spin coating. The inkjet printer deposits precise amounts of ink under atmospheric pressure at room temperature that results in uniform and continuous film using two approaches: thermal approach and piezoelectric approach. Figure 23 illustrates the schematic representation of an inkjet printer where a low-viscous ink should fill the chamber till reaching the nozzle by keeping high surface tension to avoid the dripping phenomenon. Then, ink droplets can be produced by heat to make volume

expansion–contraction or by piezoelectricity by applying voltage pulses to change the volume via mechanical forces [99]. After their ejection, the droplets will spread, allowing their fusion with neighboring droplets, and evaporate until drying, thereby producing the formation of the desired thin film. During the inkjet processing, the substrate is monitored by moving it along a specific direction and speed to ensure its coating by ink droplets according to the optimal conditions. The well-definition of printed films depends on surface tension and viscosity of ink, and droplet velocity and volume, which, in turn, depend on the nozzle size, the pulse amplitude and width (piezoelectric approach) and the temperature (thermal approach) [62].
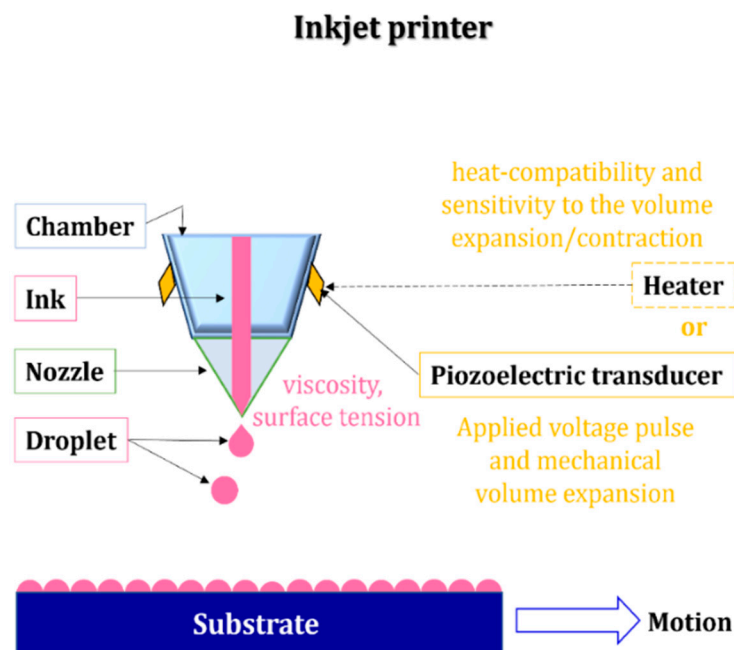


**Figure 23.** Schematic representation of inkjet printing setup.

In an interesting work, Huang et al. have produced NiO by inkjet printing for temperature sensing applications, as illustrated in Figure 24 [100]. They mixed 0.5 g of NiO nanopowder (particles' diameter of 50 nm) with 1 g of ethylene glycol and 9 g of deionized water, resulting in an aqueous mixture sonicated for 10 min. A suspension of the NiO nanoparticles in 10 wt% ethylene glycol aqueous solution at pH = 6 to form a stable particle ink. A centrifugation at 3000 rpm for 10 min is performed to remove the aggregation of large particles and to prepare the ink that will be printed with a viscosity of 5.92 cP and surface tension of 63.4 mN/m. The NiO inkjet printing onto polyimide films or glass plates is developed at room temperature using a piezoelectric configuration where the droplets with a diameter of 55 μm are ejected at a speed of 2.5 m/s. It is noteworthy that the printing was made at a speed of 0.025 m/s with dot spacing of 50 μm, followed by thermal annealing at 200 °C of NiO film for calcination. The printing of square NiO thin film in between two parallel conductive tracks on polyimide or film glass plates shows great sensitivity to temperature and applicability for flexible and miniaturized temperature sensors [100]. SEM characterization demonstrates a granular and compact thin film of 13.5 and 16 nm in thickness with NiO nanoparticles of 50 nm in diameter. (See Figure 24).
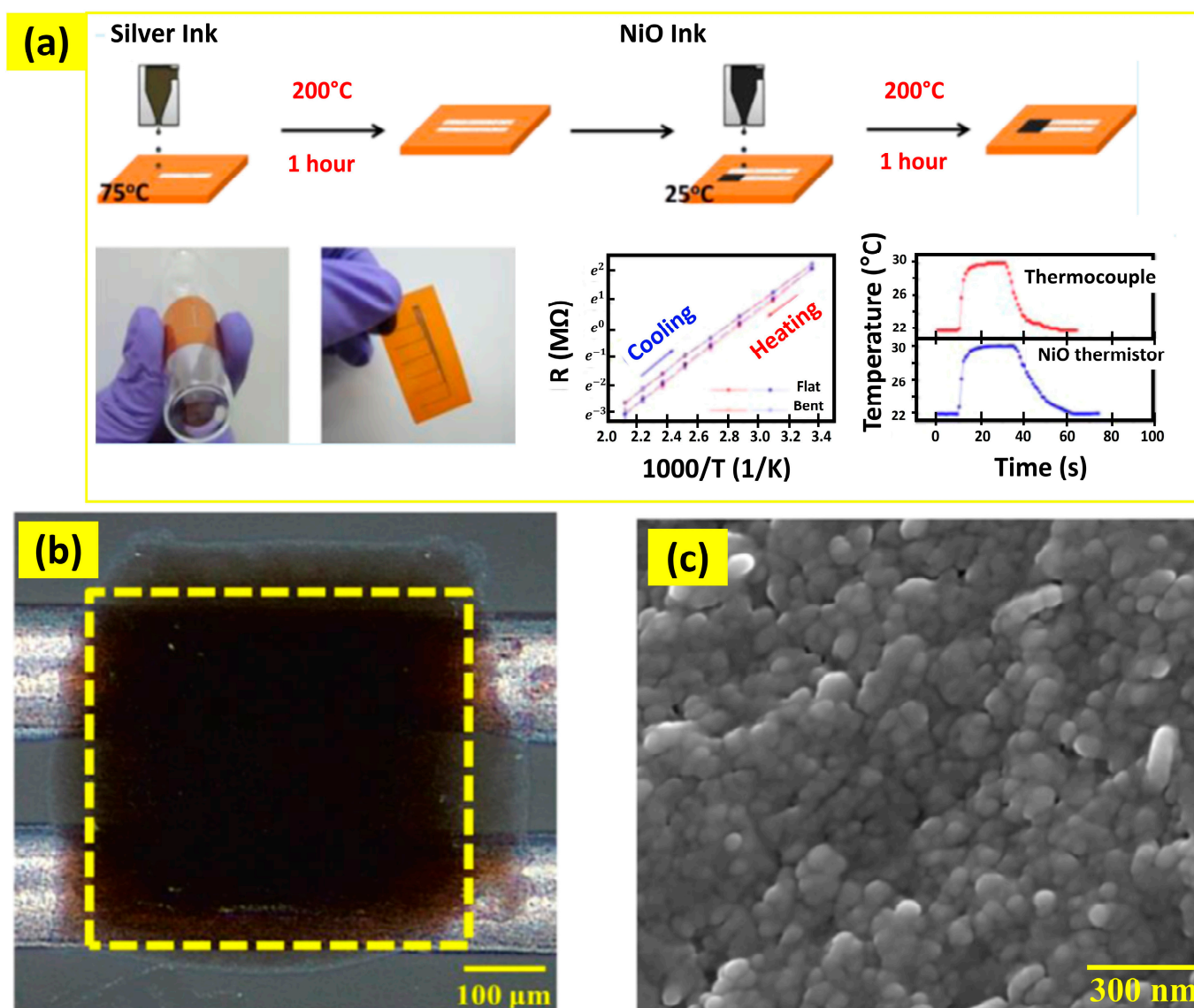
**Figure 24.** (**a**) Inkjet printing of NiO, (**b**) printed NiO film over silver tracks on a glass plate at 25 °C, and (**c**) SEM image of NiO film, reproduced from reference [100] ACS publisher (Copyright 2013).

## *2.3. Solution Processing*

### 2.3.1. Hydrothermal

Hydrothermal processes refer to the chemical reactions that take place in water under high temperatures and pressure. These processes occur naturally in the Earth's crust, where they play a significant role in the formation of minerals and rocks [101]. Hydrothermal processes also have a wide range of industrial applications, such as the production of nanomaterials and the treatment of waste materials [102,103].

The high temperature and pressure alter the properties of water, making it an excellent solvent for many substances. This condition also increases the rate of chemical reactions by accelerating the collision frequency between molecules. The main mechanisms of hydrothermal processes include hydrolysis and condensation reactions [104,105].

Hydrolysis is a chemical reaction in which water is used to break down a compound into two or more components. This mechanism is essential in hydrothermal processes because it helps to dissolve minerals in water, leading to the formation of new minerals. For example, the hydrolysis of silicate minerals can lead to the formation of clay minerals [106]. However, condensation is a process in which dissolved substances in a solution form solid particles. It occurs when the concentration of dissolved minerals exceeds their

solubility limits. The solubility of the precursors increases with temperature, leading to supersaturation of the solution. As the temperature and pressure are lowered, the solubility decreases, resulting in the nucleation and growth of the solid phase. These reactions can be controlled by varying the temperature, pressure, reaction time, and precursor concentration. In addition, the resulting particles' size and morphology can be tailored by adjusting the reaction conditions, including the use of surfactants or templates to direct the crystal growth.

Calcination can be a subsequent step in the hydrothermal process for the synthesis of various nanomaterials. It involves heating the material in air to remove any organic or inorganic impurities and promote crystal growth. The temperature and duration of the calcination process play a crucial role in determining the physical and chemical properties of the final product. During the calcination process, the organic ligands, surfactants, or capping agents used in the synthesis process are removed, resulting in a pure inorganic material. Calcining at specific temperatures can facilitate the formation of interparticle bonds and promote grain growth, leading to the formation of a crystalline material [107–109]. Moreover, the calcination temperature [110] and ramping rate [111] affect the degree of crystallinity, phase composition, and particle size distribution of the synthesized material. Therefore, careful optimization of the calcination conditions is essential to obtain the desired morphology, crystal structure, and size of the material.

NiO nanostructures were synthesized using the hydrothermal method by Mokoena et al., employing nickel nitrate and hexamethylenetetramine (HMT) as precursors. Initially, 2.908 g of nickel nitrate hexahydrate was dissolved in 50 mL of deionized water, while 4.206 g of HMT was prepared in another 50 mL of DI water. The two solutions were mixed and stirred for 4 h to obtain a uniform solution, which was then poured into Teflon-coated stainless-steel autoclaves. The autoclaves were subjected to 150 °C for 14 h, followed by washing with ethanol and DI water several times. The collected powders were dried in an oven at 80 °C for 15 h and then calcined at 400 °C for 2 h in air. The calcination process was carried out at various ramping rates ranging from 1 to 3 °C/min. The resulting NiO nanostructures were obtained in the form of powder, suitable for further analysis and use in various applications (refer to Figure 25a for the graphical representation of the synthesis process) [111].
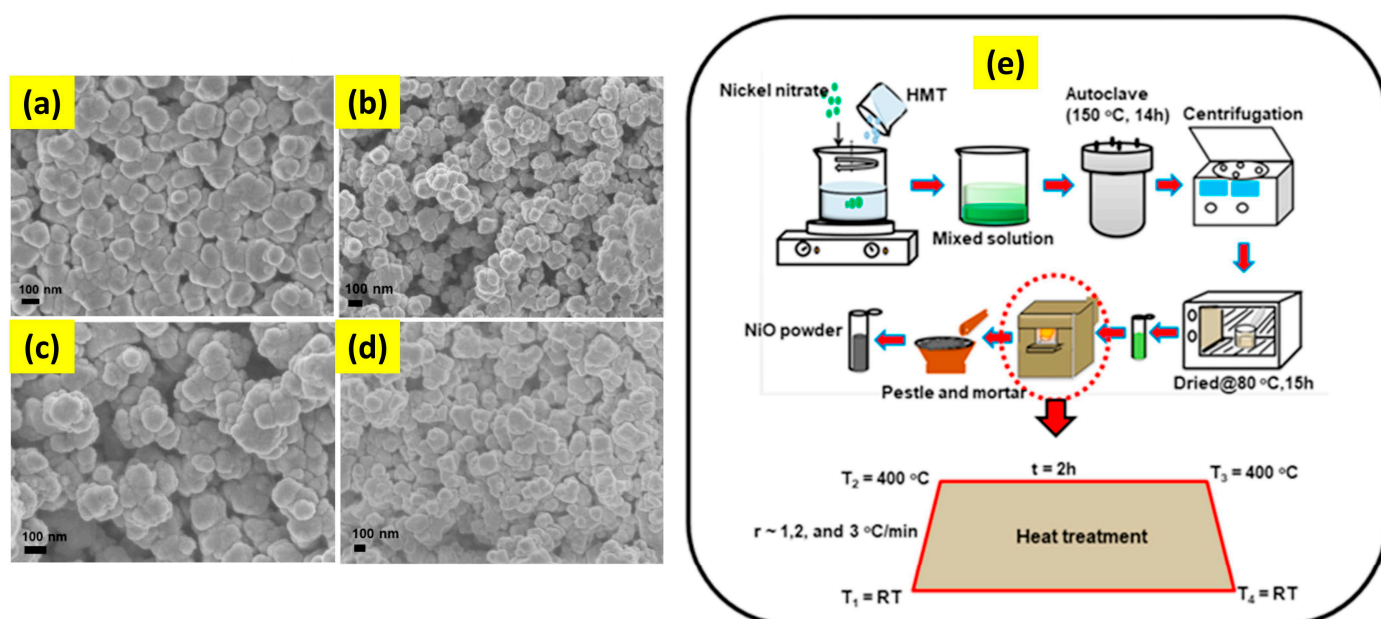


**Figure 25.** SEM images of NiO powder calcined at 400 °C for different ramping rates (**a**) 0 °C/min, (**b**) 1 °C/min, (**c**) 2 °C/min, and (**d**) 3 °C/min, (**e**) schematic illustration of hydrothermal growth, reproduced from reference [111] Elsevier publisher (Copyright 2020).

The morphology of NiO nanostructures calcined at various ramping rates was investigated using SEM micrographs, as shown in Figure 25a–d. The as-grown sample exhibited agglomerated nanoparticles, whereas the samples calcined at 400 °C showed smaller nanoparticles at various ramping rates. These results indicate that heat treatment and/or ramping rate can alter the properties of nanomaterials. Specifically, the size and agglomeration of nanoparticles were found to be dependent on the ramping rate during calcination. These findings highlight the importance of carefully controlling the heat treatment conditions to achieve the desired morphological properties in nanomaterials.

The effects of different ramping rates on the size, shape, and distribution of particles in NiO were studied. It was observed that the sample annealed at a slow ramping rate of 1 °C/min had the most uniform distribution of particles in terms of both size and shape. Furthermore, the smallest particle size showed minimal variation with different ramping rates. On the other hand, the sample annealed at a faster ramping rate of 3 °C/min exhibited more cracks on its surface. Additionally, a relatively non-uniform distribution of the size and shape of particles was observed at this ramping rate despite an improvement in the crystallinity of the sample when compared to other ramping rates. These findings suggest that the ramping rate during calcination plays a critical role in determining the uniformity of the particle size and shape in the sample, as well as the quality of its crystallinity.

2.3.2. Sol–Gel

The sol–gel method involves the preparation of a sol, which is a colloidal suspension of a precursor in a liquid solvent. This is followed by aging, gelation, and drying to obtain the final product. For metal oxide synthesis, metal alkoxides are used to form the solution. In the first step, the metal alkoxides are dissolved in a suitable solvent, such as water or organic solvents, and stirred for several hours to form a clear solution. The molar ratio of metal precursor to solvent should be tuned based on the desired properties of the final product. In the next step, the sol is subjected to gelation by adding a suitable gelation agent such as ammonia, acetic acid, or hydrogen peroxide. The gelation time and temperature are varied to optimize the size and morphology of the resulting metal oxide particles. The gel is then washed, dried, and calcined to obtain the final product in the form of a powder [112,113].

Aerogels, xerogels, and cryogels are all types of solid gels, but they differ in how they are formed and their physical properties [112].

Aerogel is formed by extracting the liquid from a gel at a supercritical state, which means that the liquid is heated and pressurized to a point where it has the properties of both a gas and a liquid. The resulting material is a highly porous and lightweight solid that has excellent thermal insulation properties.

Xerogel, on the other hand, is formed by evaporating the liquid from a gel at room temperature. This process leads to the formation of a solid material that has a high surface area.

Cryogel is formed by freezing a gel and then removing the ice by sublimation. This results in a highly porous and interconnected solid material that is used for a variety of applications, including tissue engineering, drug delivery, gas sensing, and catalysis.

Figure 26 represents the different solid gels formed by the sol–gel technique [114].

Several key parameters influence the outcome and properties of materials produced using the sol–gel derived materials, including precursor chemicals (metal alkoxides, chlorides, etc.), solvent type (affects the solubility of precursors and the reaction kinetics), catalyst/surfactant (control reaction rates, homogeneity, particle size, surface area, dispersion), pH level of the solution (influence the hydrolysis and condensation reactions), stirring and mixing, aging time, reaction temperature during gel formation, drying method (type of the gel), and calcination at specific temperatures and durations [115–118].

The precise control and optimization of these parameters allow researchers to tailor the properties of materials synthesized via the sol–gel method to meet specific application requirements.
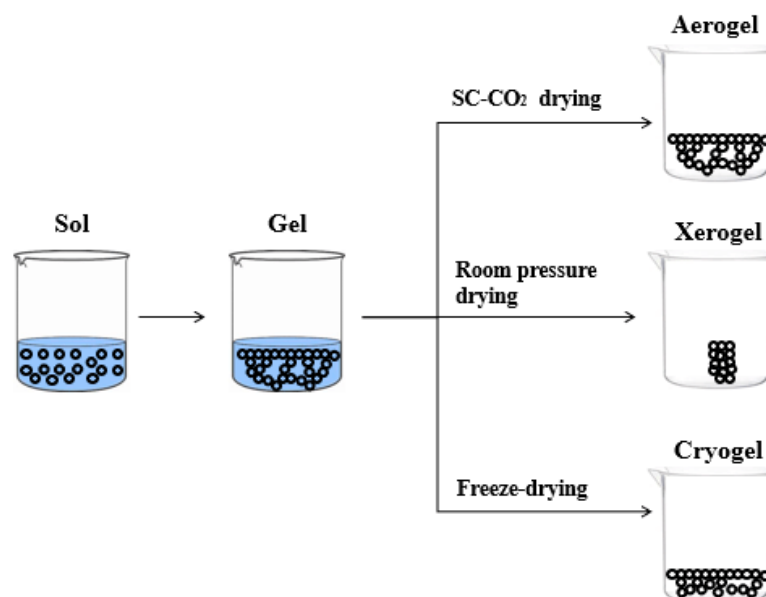
**Figure 26.** Schema of various solid gels, reproduced from reference [114] MDPI publisher (Copyright 2021).

Babei et al. [119] synthesized NiO gel by dissolving 2.0 g (8.41 mmol) of $NiCl_2$ $6H_2O$ in 13.5 mL of absolute ethanol, resulting in a homogeneous and clear solution. Next, 5.37 g (92.5 mmol) of propylene oxide was added dropwise to the solution while stirring, resulting in a PO:Ni molar ratio of 11:1. The solution was stirred for 10 min and then transferred into a syringe. After approximately 30 min, a uniform, light green opaque nickel oxide gel was formed. The wet gel was then aged for 24 h under ambient conditions. The gels were kept in a $CO_2$ dryer chamber at a pressure of 110 bar and a temperature of 50 °C for 3 h, followed by releasing the pressure at a rate of 6 bar/min to be dried. Then, they were calcined for 4 h at different temperatures (250–600 °C) with a heating rate of 3 °C/min. The as-synthesized gels were dried at room temperature for 30 days/80 °C overnight. On the other hand, xerogels have been calcined at the same temperatures. SEM characterization reveals spherical NiO nanoparticles that agglomerate to form larger particles (See Figure 27a–f). Xerogels were found to have a more compact structure compared to aerogels, which was reflected in their lower mesopore volume and specific surface area. However, aerogels had a more porous structure and smaller particle sizes than xerogels. This was attributed to the collapse of the pore structure during the evaporation drying process that led to the formation of dense clusters of xerogel particles and loss of specific surface area and pore volume. This collapse was caused by the formation of a liquid–vapor interface within the gel during evaporation that generated surface tension, leading to pore shrinkage. However, this effect was avoided when the solvent was removed under supercritical conditions, which allowed for the gel to be dried without pore shrinkage. The calcination process of both nickel oxide aerogels and xerogels resulted in the formation of a pure NiO phase with characteristic peaks that corresponded to the (111), (200), (220), (311), and (222) crystal planes, as indicated by the JCPDS card 04-0835 (See Figure 27g). As the calcination temperature was increased from 300 °C to 600 °C, the XRD reflections became narrower and sharper, indicating the sintering of small NiO nanoparticles. One can note that sintering is less pronounced for NiO aerogels compared to xerogels despite having almost similar peak intensities.
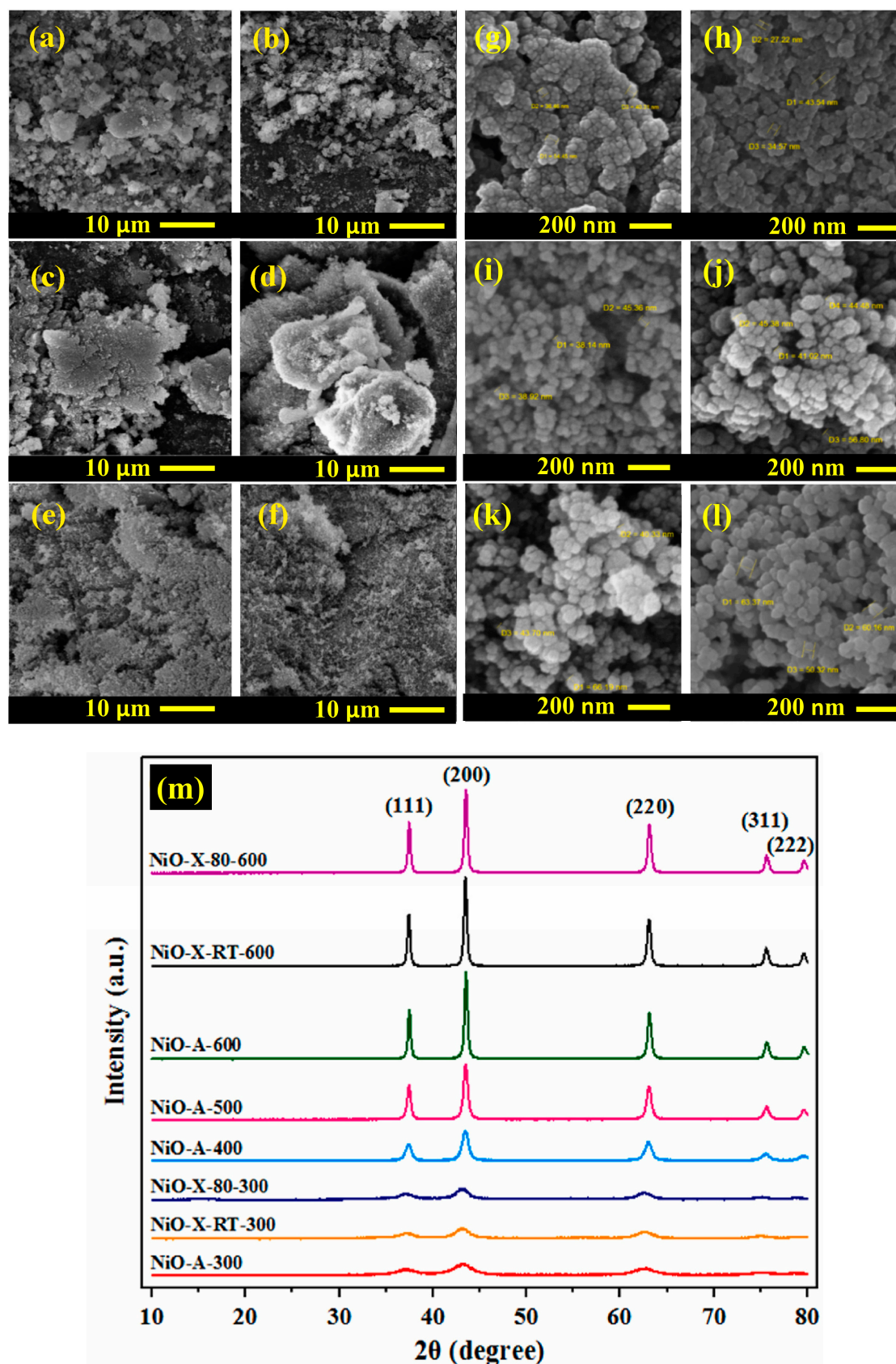
**Figure 27.** SEM micrographs of NiO xerogels: (**a**,**f**) at 10 μm, (**g**,**l**) at 10 nm and NiO aerogels: (**b**–**e**) at 10 μm, (**h**–**k**) at 10 nm, calcined for 4 h at different temperatures, and (**m**) XRD patterns of NiO xerogels and aerogels calcined at various temperatures, reproduced from reference [119] Elsevier publisher (Copyright 2022).

### 2.3.3. Micro-Emulsion

In a micro-emulsion system, a surfactant is used to form micelles in a solution of water and oil or other organic solvents. The micelles act as nanoreactors, allowing the precursors to diffuse into the core of the micelle, where they can undergo chemical reactions to form nanoparticles. By controlling the size and shape of the micelles, it is possible to control those of the resulting nanoparticles. At a macroscopic level, the mixture of oil, water, and surfactant appears homogeneous, seamlessly combining these components. However, at a microscopic scale, it reveals a captivating structure comprising water or oil droplets intricately enveloped by a layer of surfactant molecules [120].

The micro-emulsion technique offers several advantages over other methods, including the ability to produce monodisperse nanoparticles with a narrow size distribution, high yields, and the ability to tune the properties of the nanoparticles by varying the reaction conditions [121,122]. It has been successfully applied to the synthesis of a wide range of nanomaterials, including metals and metal oxides, making it an important tool for nanoparticle synthesis with a typical size of between 30 nm and 100 nm [122–124].

Several parameters can influence the properties of the synthesized nanoparticles, such as surfactant, which is crucial for forming the micelles (it should be chosen such that it can stabilize the micelles and prevent conglomerate and coalescence during the reaction [125]), solvent (it depends on the solubility of the precursors and surfactants), water-to-surfactant molar ratio (it can influence the stoichiometry of the reaction, leading to differences in the composition, size, and morphology of the nanoparticles), temperature and reaction time (they can influence the kinetics of the reaction and affect the size, the morphology and the crystallinity of the nanoparticles produced [126]) [120]. Finally, the choice of co-surfactants, pH, and ionic strength can also influence the micro-emulsion technique's outcome [127,128]. The addition of co-surfactants can affect the micelle size and shape and, hence, the resulting nanoparticles. The pH and ionic strength can influence the electrostatic interactions [129] between the reactants and surfactants, leading to differences in the size and morphology of the nanoparticles.

Figure 28 shows a diagram of the micro-emulsion setup.
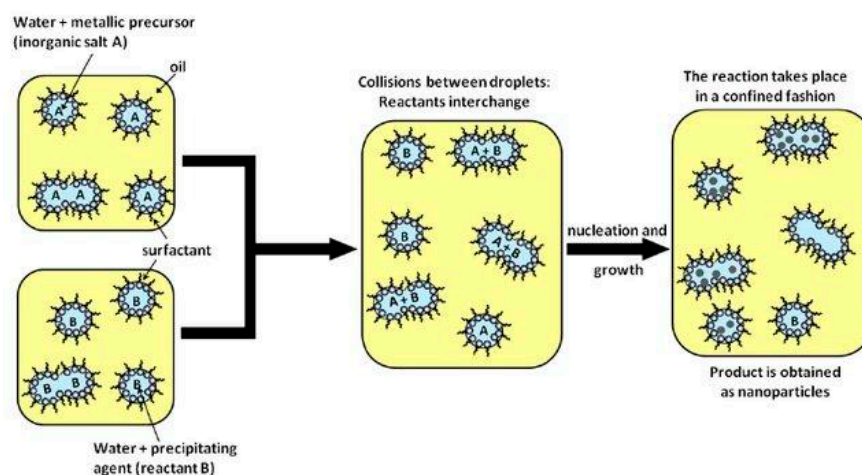


**Figure 28.** Schematic representation of micro-emulsion setup, reproduced from reference [130] Intech publisher (Copyright 2012).

T. Elayampallayam used ethylene glycol to dissolve 2.5 mM of $NiCl_2$. Hydrazine and NaOH were added as a reducing agent and as a catalyst, respectively, to form nickel ions. The resulting mixture was stirred well. At a temperature exceeding 90 °C, a bluish-green-colored precipitate slowly changed to black, indicating the formation of Ni nanoparticles related to reducing $Ni^{2+}$ ions to $Ni^{(0)}$. The NiO nanoparticles' size is averaged to 12 nm with FCC crystallinity [131].

In another work, the synthesis of nickel oxide involves two steps: the synthesis of nickel oxalate dihydrate nanoparticles and their subsequent thermal decomposition. To synthesize the nickel oxalate dihydrate, two micro-emulsions (I and II) were prepared. Micro-emulsion (I) contained cetyltrimethylammonium bromide (CTAB) as the surfactant, n-butanol as the co-surfactant, isooctane as the hydrocarbon phase, and a 0.1 M nickel nitrate solution as the aqueous phase. Micro-emulsion (II) contained the same constituents except for having 0.1 M ammonium oxalate instead of nickel nitrate as the aqueous phase. The weight fractions of the various constituents in these micro-emulsions were carefully controlled. After slow mixing and stirring overnight, the precipitate was separated from the solvent and surfactant by centrifugation and washing with a 1:1 mixture of methanol and chloroform. The resulting precipitate was then dried at 120 °C for 1 h. Finally, the precursor was heated in air at 450 °C for 6 h to yield monophasic nickel oxide nanoparticles [132]. XRD patterns show growth preferability along the (200) orientation of NiO powder, whereas the TEM and electron diffraction prove homogeneous NiO nanoparticles of 25 nm with narrow size distribution.

### 2.3.4. Successive Ionic Layer Adsorption and Reaction Method (SILAR)

The SILAR method involves the deposition of ionic species onto a substrate in alternating cycles of adsorption and reaction. The adsorption step involves immersing the substrate in a solution containing a metal precursor, followed by rinsing with a suitable solvent. The reaction step involves exposure to a second solution containing a reactive agent, followed by rinsing. The process is repeated for several cycles until the desired thickness of the metal oxide film is achieved [133,134].

Taşdemirci et al. have deposited NiO films on a glass substrate using the SILAR method, described in Figure 29 [135]. The SILAR cycle for the fabrication process involved four stages. In the first stage, the glass substrate was immersed in the ([Ni(NH$_3$)$_4$]$^{2+}$) solution for 30 s. In the second stage, the substrate was removed from the solution and kept in hot water, boiling at 90 °C for 7 s. In the third stage, the substrate was air-dried for 60 s. In the fourth stage, the substrate was rinsed in pure water for 30 s, and the large and weakly bonded NiO particles were removed from the surface. The cycle was repeated until the entire surface was homogeneously coated with the NiO thin films.
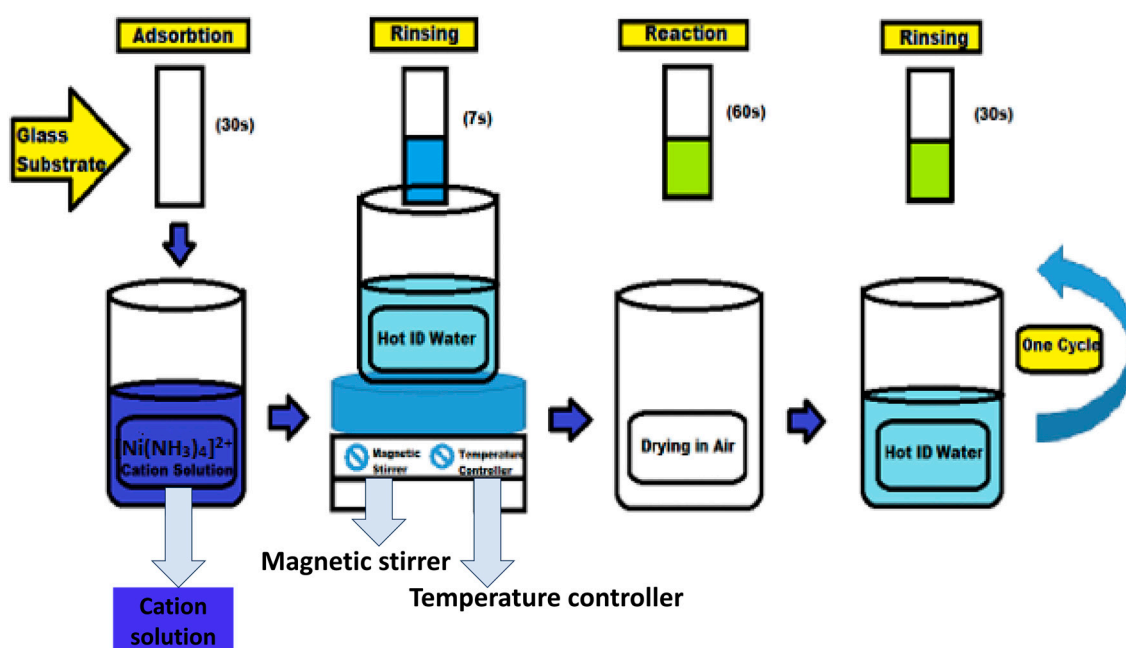


**Figure 29.** Schematic of SILAR technique, reproduced from reference [135] Elsevier publisher (Copyright 2019).

The microstructure analysis obtained by SEM reveals properly coated films. The as-grown NiO shows a uniform coating, whereas the annealed NiO at 200 °C and 300 °C keeps the structure homogeneous. Whilst annealing NiO at 400 °C disrupts the structure by creating cracks on the surface. The surface roughness was also examined by AFM, proving that annealing made the sample smoother.

## 3. Gas Sensing Mechanism

Gas sensors based on semiconductor metal oxides operate by monitoring the change in electrical resistance of the sensing material in response to the presence of chemical compounds in the vapor phase. The physical and chemical processes involved in detecting the target gas are complex and include charge carrier transfer, surface reactions, gas transport, and diffusion. Despite significant research efforts, the sensing mechanisms of metal oxide gas sensors have not been fully understood. However, some models have been proposed to explain the mechanisms, such as the surface reaction model, the bulk diffusion model, and the spillover model [136,137].

Regarding NiO gas sensors, they operate by controlling mobile charge carriers to detect changes in their conductivity. When exposed to air, oxygen molecules are adsorbed and oxidized on the surface of the NiO by capturing conduction band electrons, forming $O_2^-$ (T < 100 °C), $O^-$ (100 °C < T < 300 °C), and $O^{2-}$ ions (T > 300 °C). This transfer of electrons generated holes, causing the resistance to decrease. In the presence of reducing gases, the chemisorbed oxygen anions on the surface of NiO may react with the gas, removing the anions and oxidizing the gas. The gas-sensing mechanism can be elucidated using Figure 30: Initially, oxygen molecules are adsorbed onto the surface of NiO, leading to the formation of adsorbed oxygen. Then, an electron accumulation layer (EAL) is created on its surface, thereby increasing the surface barrier. When NiO is exposed to a reducing gas like hydrogen, $H_2$ molecules release electrons that subsequently combine with the existing holes within the NiO material. This interaction results in a narrower EAL and an elevation in the barrier height. Consequently, the resistance of the NiO material increases. This change in resistance can be measured and utilized to detect the presence or concentration of hydrogen gas. However, a decrease in the NiO resistance is recorded under exposure to oxidizing gases, which reduces the nickel ions from (II) to (I) by donating electrons to the NiO lattice [138,139].

Wang et al. [140] tried to study the gas sensing mechanism of the NiO (100) surface by examining its energetic and electronic properties after exposure to $NO_2$, $H_2S$, and $NH_3$ gases, based on density functional theory (DFT) calculations (See Figure 31). It was found that the chemisorption of $NO_2$ on the NiO surface is stronger than that of $H_2S$ and $NH_3$, so the removal of $NO_2$ molecules from the surface is very difficult compared to the other gases, which can lead to prolonged recovery time and incomplete recovery, as proven in many research works [141–144]. However, NiO exhibits full recovery when testing against ammonia and hydrogen sulfide [145,146].

### 3.1. Impact of Growth Method on Gas Sensing Performances

The gas sensing performance of metal oxides is highly influenced by morphology and low dimensionality of materials due to several key factors. First, the surface-to-volume ratio increases as the size of the material decreases, resulting in a larger active surface area available for interaction with gas molecules. This surface enhancement results in good sensitivity to gas adsorption and improves the overall sensing response. Second, morphology, including the shape and structure of the metal oxide nanoparticles, plays a crucial role in determining the gas-sensing properties. Different morphologies can offer various surface sites and crystal facets, affecting the adsorption and desorption of gas molecules. This can lead to improvements in selectivity and sensitivity towards specific gas species. Additionally, low-dimensional nanomaterials, such as nanowires, nanotubes, or nanosheets, exhibit unique electronic and structural properties. These features can contribute to more efficient charge transfer and better interaction with gas molecules,

resulting in better sensitivity. One can note that the growth method, which is primarily responsible for obtaining specific structure and morphology (as mentioned in Section 2), plays a crucial role in tuning the gas-sensing properties of metal oxides.
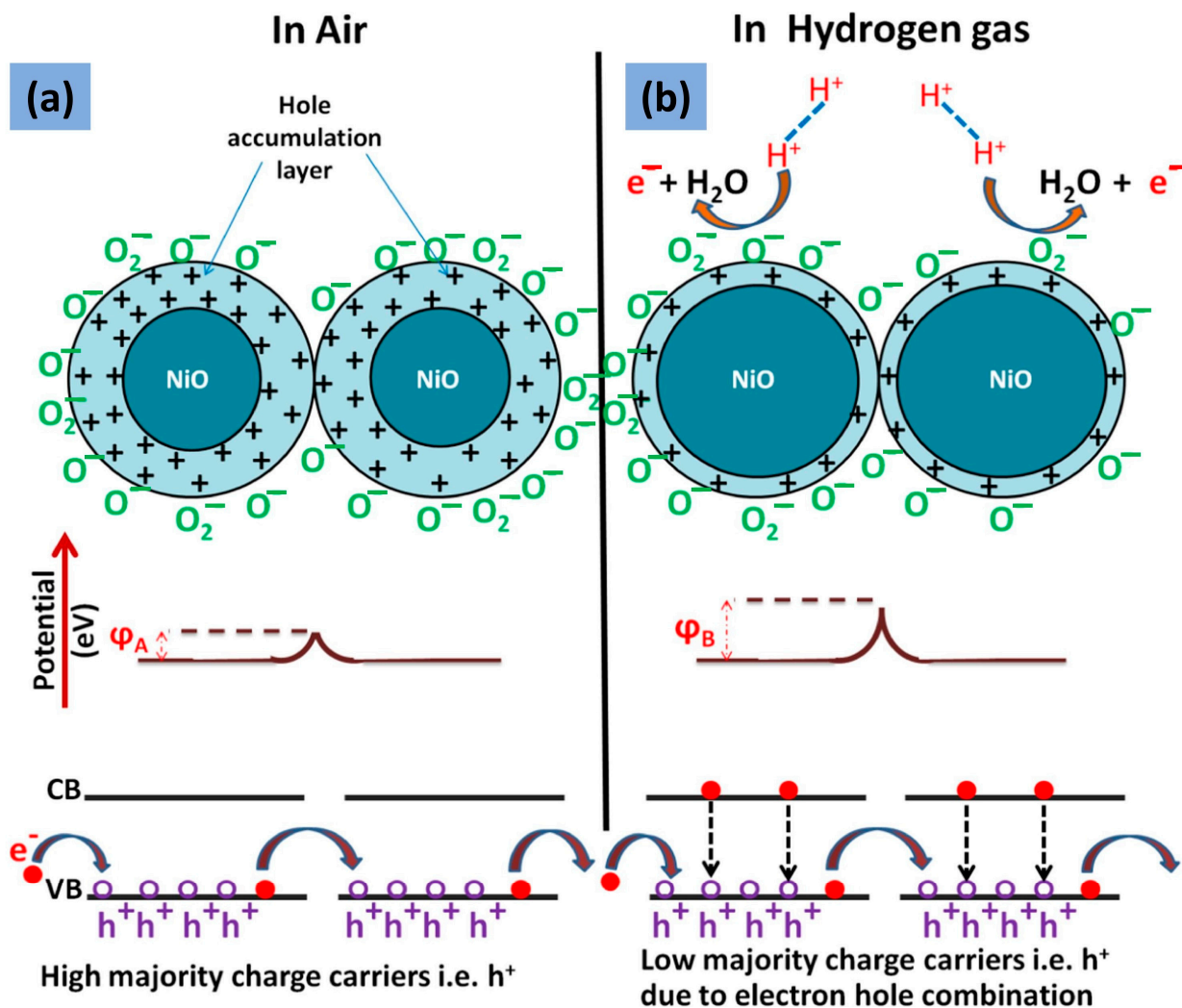


**Figure 30.** Gas-sensing mechanism (**a**) in air and (**b**) in hydrogen gas environment, reproduced from reference [139] Elsevier publisher (Copyright 2020).

The morphology of NiO structures strongly impacts the sensing performances, such as sensitivity, selectivity, response time, and working temperature, as mentioned in the literature [147,148]. Consider the case of pure and hydrothermally grown NiO nanostructures [149]; three distinct structures are derived through the following:

- Dissolving tri-sodium citrate dihydrate (0.588 g) and nickel chloride hexahydrate (0.475 g) in 40 mL of deionized water and stirring them vigorously until reaching a clear green solution into which 20 mL of ethanol was added under stirring to make a transparent mixture that is transferred to the lined-autoclave at 190 °C for 8 h and 12 h, resulting in NiO solid spheres.
- Dissolving the same amount of nickel chloride with urea (0.6 g) in 40 mL of deionized water and 10 mL of ethanol to which 0.002 mol of CTAB agent was added and stirred until the solution was clear and transferred to the autoclave at 200 °C for 8 h and 12 h, resulting in NiO porous spheres.
- Dissolving the same amount of nickel chloride with urea (3.5 g) in 20 mL of deionized water and 20 mL of ethanol under stirring to obtain a clear blue solution that is transferred to the autoclave at 140 °C for 8 h and 12 h, resulting in NiO hollow spheres.
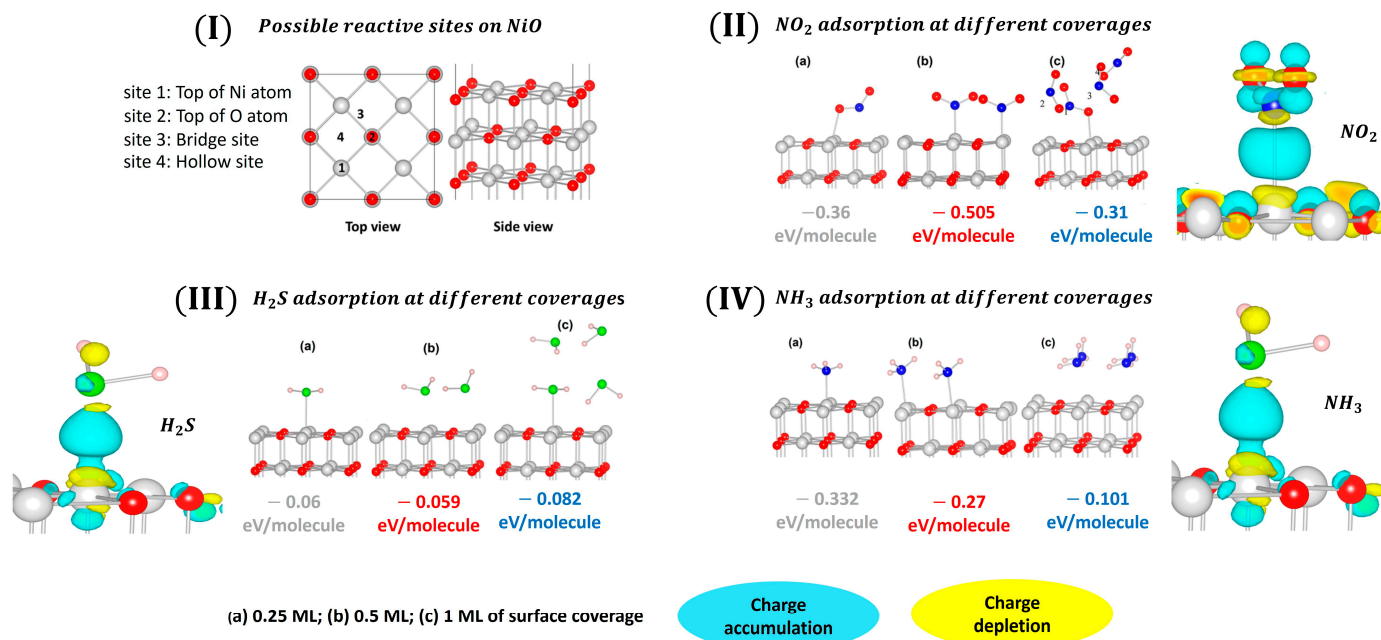
## DFT calculations of gas adsorption on NiO surface



**Figure 31.** DFT calculations of various gases' adsorption on NiO surface with the indication of (**I**) the possible reactive sites on NiO and the adsorption energy of (**II**) $NO_2$ gas, (**III**) $H_2S$ gas, and (**IV**) $NH_3$ gas at different surface coverages: (**a**) 0.25 monolayer (ML), (**b**) 0.5 monolayer (ML), and (**c**) 1 monolayer (ML), reproduced from reference [140] ACS publisher (Copyright 2012). Colors associated to atoms: Grey: Nickel, Red: Oxygen, Navy blue: Nitrogen, Light violet: Hydrogen, Green: Sulfur.

The 2 h-calcination of the products is performed in air at 400 °C for solid and porous spheres and 500 °C for the hollow spheres to transform $Ni(OH)_2$ to pure NiO.

The gas testing of these structures reveals that hollow spheres provide the highest response toward 400 ppm of ethanol at an optimum temperature of 350 °C. Porous structure also presents a higher response than solid spheres. This enhancement is ascribed to the increased specific surface area and smaller Debye length associated with the porous and hollow structures. Notably, the investigation shows that ethanol molecules can efficiently penetrate the interior of the NiO hollow sphere (or pores within the microsphere) where the adsorption sites' density is higher, facilitating complete gas-sensing reactions and enhancing the ethanol response.

Other NiO nanostructures grown by hydrothermal process show sensitivity to $H_2S$ gas with high selectivity at 250 °C [150]. 11.64 g of $Ni(NO_3)_2$ 6 $H_2O$ and 2 g of NaOH were dissolved in 40 mL distilled water for 10 min before being transferred into a 50 mL Teflon-lined stainless-steel autoclave. The mixture was subsequently aged at 185 °C for varying durations (2, 4, 6, and 8 h). The resulting $Ni(OH)_2$ nanoplates were then subjected to centrifugation and washed with distilled $H_2O$ and ethanol multiple times. The obtained powders were dried at 60 °C for 24 h, followed by calcination at 600 °C. They proved the presence of local p–n homojunction in hexagonal-annular NiO material by positron annihilation experiments after calcining the β-$Ni(OH)_2$ nanoplates for 5 h. One can see the morphological transformation of the precursor in Figure 32a. Annealing for 1 h allows the formation of discrete, small hollows within the β-$Ni(OH)_2$ plates while maintaining their initial hexagonal shape. With a 3 h annealing time, these small hollows expand and concentrate around the central region, evolving into larger hollows. Intriguingly, increasing the time to 5 h leads to the disappearance of small hollows, replaced by an open-hexagonal hollow at the particle's center. The initial hexagonal shape remains, but the inner and

outer hexagons align parallelly, resulting in a symmetrical hexagonal NiO with a local p–n homojunction: NiO is conventionally known as a p-type semiconductor, attributed to the deficiency of metal ions in the material (p), whereas the number of $V_O$ exceeds that of $V_{Ni}$, suggesting a potential n-type semiconductor behavior (n). The identification of these vacancy clusters containing both $V_O$ and $V_{Ni}$, with an average size of approximately 11 atoms within NiO nanostructures, is shown in Figure 32d. The authors suggest that the active sensing site for interaction with $H_2S$ molecules in the annular NiO sensor is the O-deficient vacancy clusters. The heightened sensitivity and superior selectivity to $H_2S$, in comparison to other hexagonal NiO nanostructured sensors, may be attributed not only to higher specific surface area but also to the increased concentration of vacancy clusters within the hexagonal-annular NiO architecture. Additionally, the formation of a local p–n homojunction in NiO likely contributes as another crucial factor in enhancing the $H_2S$-sensing capabilities.



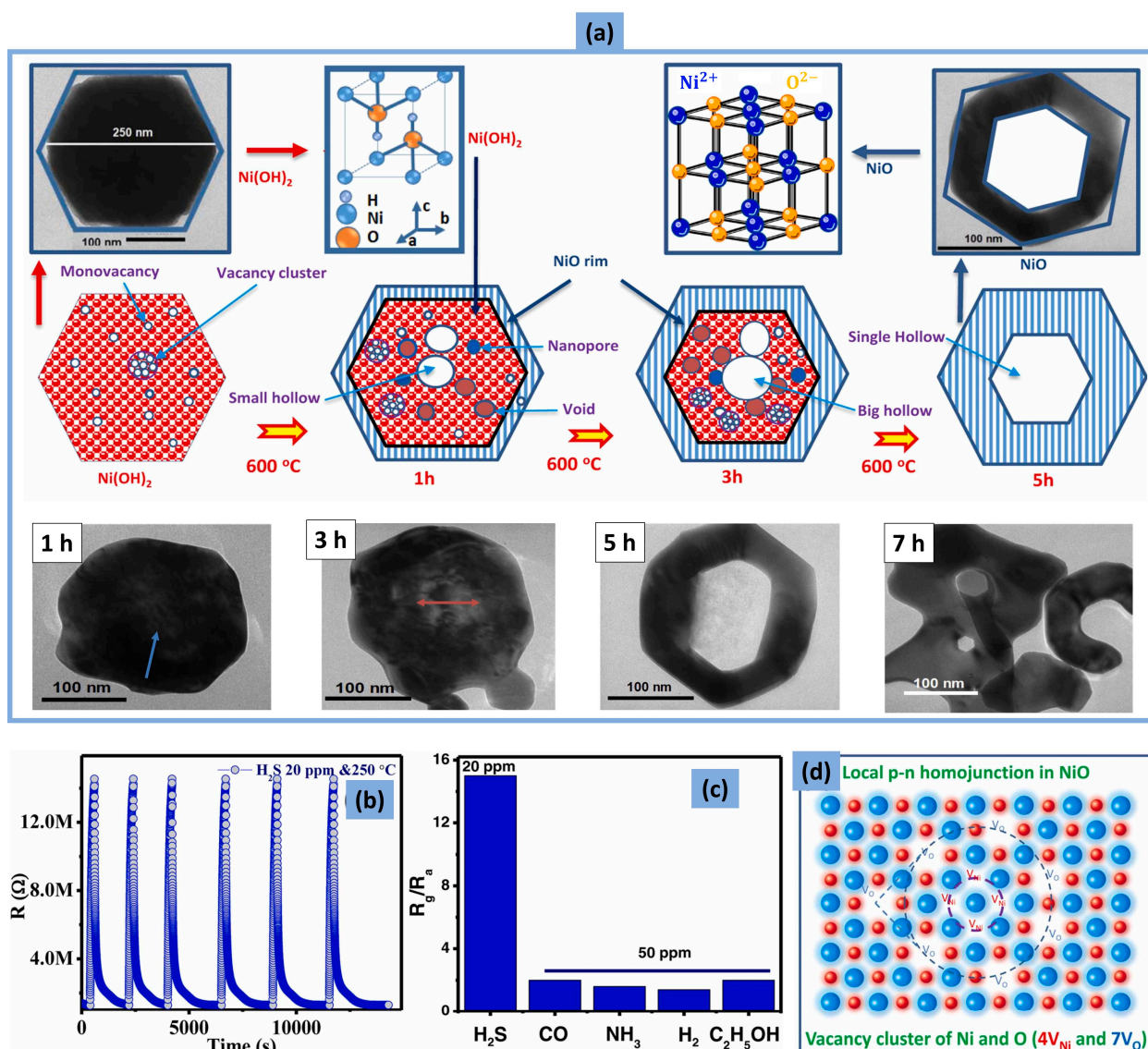**Figure 32.** (**a**) Transformation of NiO structure from $\beta$Ni(OH)$_2$ nanoplates to hexagonal annular-NiO nanoarchitecture through calcination. (**b**) Dynamic curves for $H_2S$ detection and (**c**) selectivity measurements of the NiO sensor at 250 °C are shown, and (**d**) is a schematic illustration of vacancy clusters' distribution of in NiO, reproduced from reference [150] Elsevier publisher (Copyright 2023).

The solution processing methods, such as the hydrothermal approach, result in various morphologies of NiO at the microscale and nanoscale, including hierarchical structures. This allows the enhancement of specific surface area and gas-sensing properties [151–153].

Zhao et al. prepared NiO nanomaterials from one dimension to three dimensions through the hydrothermal method, resulting in NiO nanowires, nanosheets, 'nanobulks', and nanospheres when varying the active agents PEG, EG, and glycine. Their sensing response to ethanol gas are ranked in descending order as follows: NiO nanowires, nanospheres, nanosheets, and 'nanobulks' due to the porosity and large surface area that nanowires provide over other structures which can adsorb more gas molecules [154].

However, this method is time-consuming and requires concentrated chemicals, high temperature, and pressure. On the other hand, sol–gel provides high control and high surface area at low temperatures and can be environment-friendly by adapting green synthesis. Despite its cost-effectiveness, sol–gel method is sensitive to reaction conditions, needs post-treatments like rinsing, centrifuge process, drying, and calcination [152], and does not show high porosity or hierarchical structures for NiO material [155,156] without combination with other approaches, which can drastically affect the efficiency of gas sensors.

The electrodeposition technique can provide NiO hierarchical structures, such as flower-like morphologies, where its control is ensured easily by adjusting the applied current and the reaction time. Two flower-like NiO sensors show sensitivity toward 5 ppm of ethanol at 250 °C with responses of 6.5 (current: −0.5 mA; time: 200 s) [81] and 3.75 (current: −0.6 mA; time: 150 s) [157]. This variation is due to the short reaction time that inhibits the nanosheets from completing their assembling and increasing their distribution on the surface area [158].

Table 3 reports the variation of sensing properties toward hydrogen and ethanol gases as an example, using different growth techniques.

**Table 3.** Gas sensing response to hydrogen and ethanol using different growth techniques.

| Gas Species | Gas Concentration (ppm) | Experiment | Morphology | Operating Temperature | Sensitivity ($\frac{\Delta R}{R}$) or Gas Response |
|---|---|---|---|---|---|
| Hydrogen | 200 | Hydrothermal approach [159] | Nanoparticles | 250 °C | 97.2% |
| | 50 | Ultrasonic spray pyrolysis [160] | Angular grains | 250 °C | ~17 |
| | 5000 | Sputtering + Plasma oxidation [21] | Nanobeam | 25 °C | ~45% |
| | 5000 | Sputtering + thermal oxidation [21] | Nanobeam | 25 °C | ~9 |
| Ethanol | 5 | DC reactive magnetron sputtering [20] | Granular film | 250 °C | 6% |
| | 5 | Electrodeposition [81] | Nano-roses | 230 °C | 9.11 * |
| | 100 | Solvothermal reaction [161] | Nanorod-flowers | 200 °C | 1.9 * |

* Gas response: $R_{gas}/R_{air}$

The thermal evaporation–condensation process (VLS) provides unique nanowire morphology for NiO material, as reported in the literature. Kaur et al. have demonstrated high response to $NO_2$ analyte with sensitivity of 54.8 (1 ppm) at 200 °C that outperforms sol–gel spin coated NiO's sensitivity of 0.233 (200 ppm) at 200 °C, hydrothermal NiO nanosheets' sensitivity of 0.8 (20 ppm) at 250 °C, and sputtered NiO film's sensitivity of 2.6 (5 ppm) at 160 °C [162]. VLS process can also ensure the growth of heterojunction materials such as NiO/ZnO (p–n type), NiO/WO$_3$ (p–n type), NiO/NiWO$_4$/WO$_3$ (p–p–n–type) that exhibit sensitivity toward different gases with changing selectivity and sensitivity. These last parameters are influenced not only by the morphology of NiO, surface area, and heterojunction effects but also by the operating temperature of the sensor device, which modulates gas species adsorption/desorption and charge–carrier transport, the analyte nature (reducing or oxidizing) [162–164]. It is worth noting that the operating temperature

can enhance the NiO nanowires selectivity that changes from hydrogen at 300 °C to acetone at 500 °C [42]. The same NiO nanowires show selectivity toward $NO_2$ with optimum response at 200 °C [162].

The gas response and selectivity of the NiO-based sensors depend on various factors, including the gas itself, the type of crystal structure, its surface area, particle size, morphology, operating temperature, surface modification, and composition moderation, as will be discussed in the following.

*3.2. Inorganic Composites NiO–X*

3.2.1. X = ZnO

Recent research into heterogeneous oxide sensors composed of ZnO and NiO has shown that these sensors exhibit superior gas-sensing performance when compared to their individual counterparts. One such example is a gas sensor that utilizes ZnO–NiO heterojunction microflowers, which demonstrated a larger sensing response to formaldehyde than a gas sensor composed solely of pristine ZnO microflowers [165]. In addition, ZnO nanorod arrays have shown an improved response to $H_2S$ gas-sensing when decorated with NiO [166]. These studies have shown the potential for ZnO–NiO heterogeneous oxide sensors to be used in a wide range of gas-sensing applications due to their enhanced performance when compared to individual oxide sensors.

By using the sol–gel method, Zhou et al. [167] prepared ZnO–NiO composites with different molar ratios of Ni/Zn. The ratio $x_{Ni/Zn}$ plays a pivotal role in modulating the n-type or p-type concentration in p–n composite where the gas sensing test against CO and $H_2$ shows n-type for $x_{Ni/Zn} < 0.425$ (dominated by n–n homojunctions) and p-type for $x_{Ni/Zn} > 0.425$ (dominated by p–p homojunctions), obeying to the model of depletion layer and the model of the accumulation layer, respectively. However, the ratio $x_{Ni/Zn} = 0.425$ represents opposite responses to CO and $H_2$; therefore, it can accurately differentiate individual CO and $H_2$, hence enhancing the poor discriminability of ZnO. Including NiO in the gas sensing layer of ZnO at this concentration forms heterojunctions at the interfaces between ZnO and NiO, resulting in a potential barrier through which electrons flow from n-type ZnO to p-type NiO, reaching the same Fermi energy level. These electrons transfer back into the conduction band of ZnO and NiO, causing the potential barrier height of both ZnO and NiO to decrease. The thickness of the electron depletion layer and the accumulation layer becomes thinner, allowing a decrease in the hole concentration of NiO and an increase in the electron concentration of ZnO. The abnormal sensing behavior of the ZnO–NiO composite ($x_{Ni/Zn} = 0.425$) can be explained by the different adsorbability of CO and $H_2$ on the surface of ZnO and NiO, leading to a discrepancy in content changes between the hole concentration decrease on the surface of NiO and the electron concentration increase on the surface of ZnO. It is worth noting that the sensing response of pristine ZnO is higher than the composite one due to the preferability of $H_2$ adsorption on ZnO. In addition to the molar ratio, post-annealing and operating temperature can also influence the sensitivity of this composite against reducing gases, as mentioned in Figure 33.

In another work, the co-sputtered thin film of ZnO–NiO as a heterogeneous composite gas sensor is investigated toward several gases at 300 °C and proves higher responsiveness to ethanol when compared to pure NiO responsiveness with good repeatability and stability [168].

Moreover, Zhao et al. [169] fabricated a nanostructured ZnO–NiO composite that demonstrates high sensitivity towards ethanol, a fast response/recovery rate, good reversibility, reproducibility, and robustness towards humidity at an optimum temperature of 300 °C, as can be seen in Figure 34.
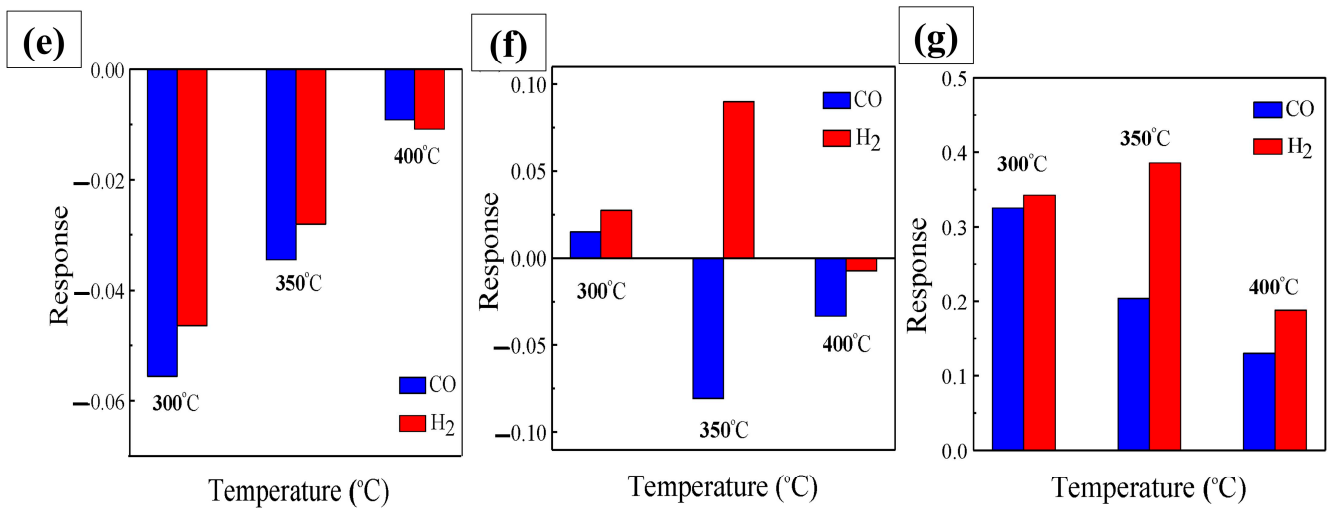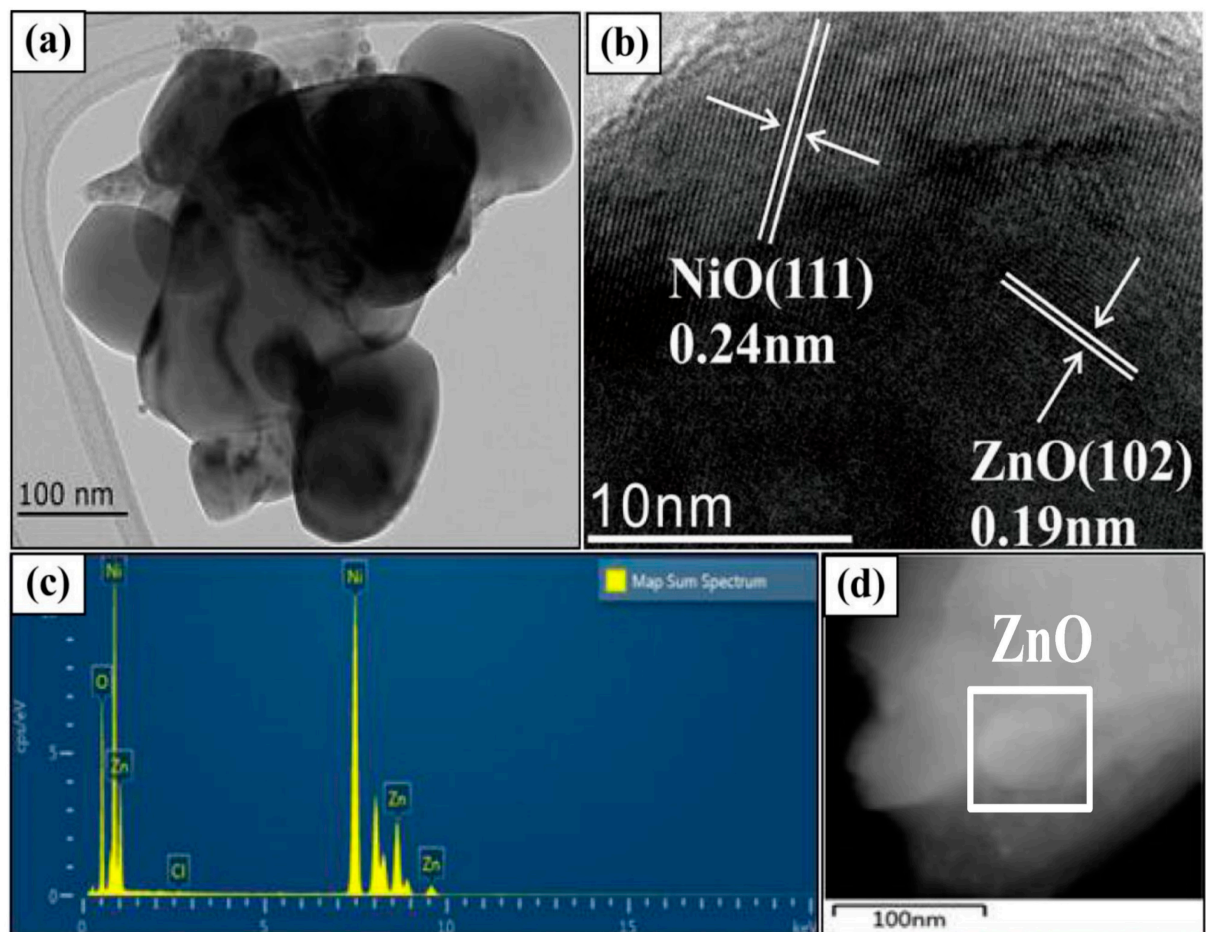
**Figure 33.** (**a**) TEM, (**b**) HRTEM, (**c**) EDS, (**d**) TEM-EDS dark-mapping scan and sensing properties of ZnO–NiO composite ($x_{Ni/Zn}$ = 0.425) at different operating temperatures after annealing at (**e**) 500 °C, (**f**) 550 °C, and (**g**) 600 °C, reproduced from reference [167] MDPI publisher (Copyright 2020).
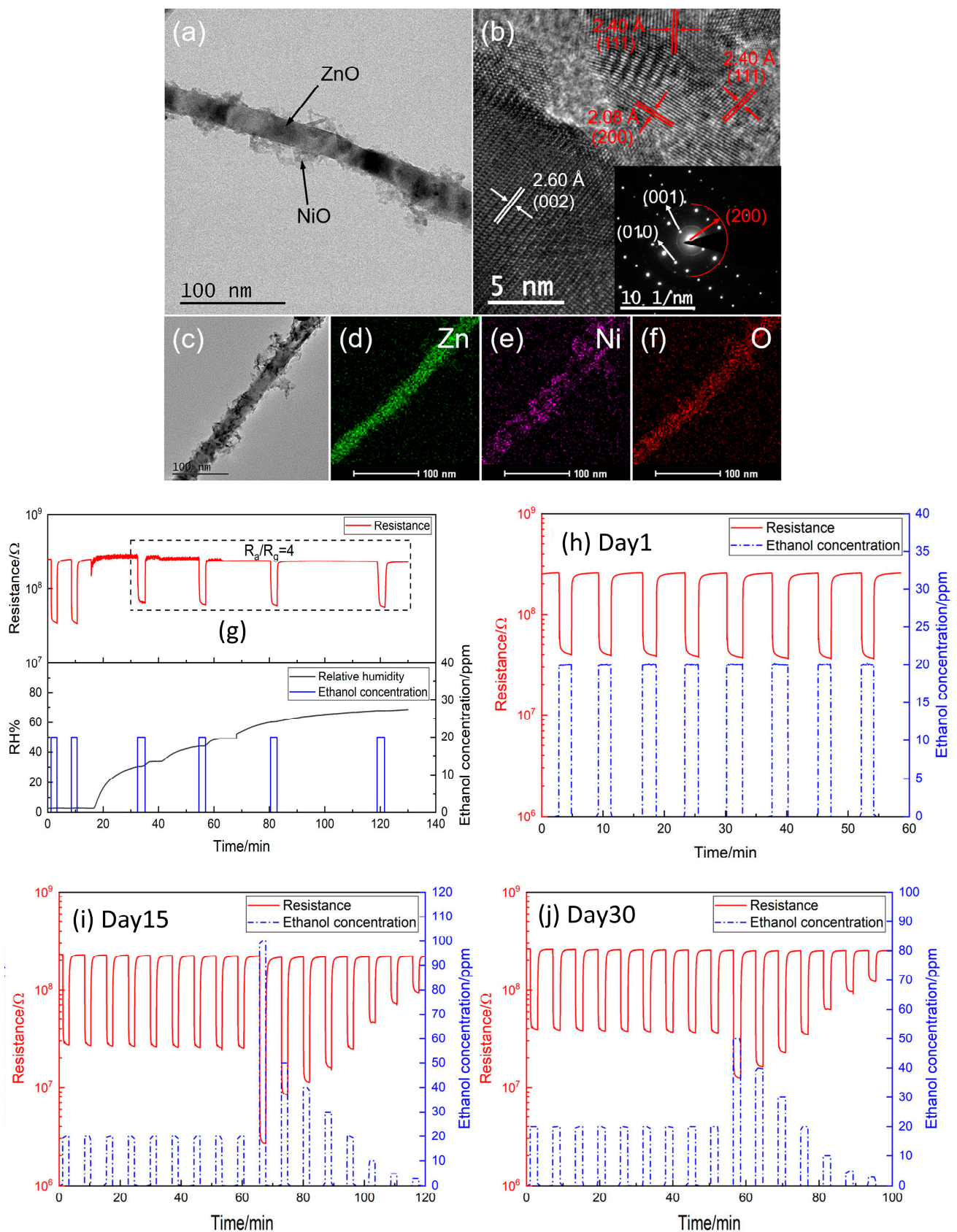
**Figure 34.** (**a**–**f**) TEM characterization of ZnO–NiO composite, and (**g**) dynamic response of NiO–ZnO gas sensor to 20 ppm ethanol under different humidity levels at 300 °C and (**h**–**j**) stability performance of the sensor trough 30 days at different ethanol concentrations, reproduced from reference [169] Elsevier publisher (Copyright 2021).

Hydrothermal preparation of pristine NiO and ZnO–NiO composite devoted to testing their gas sensitivities are reported in the literature and described in Figure 35, indicating that the composite is highly more efficient than the pristine NiO with the highest sensitivity and suitable selectivity towards acetone [170].
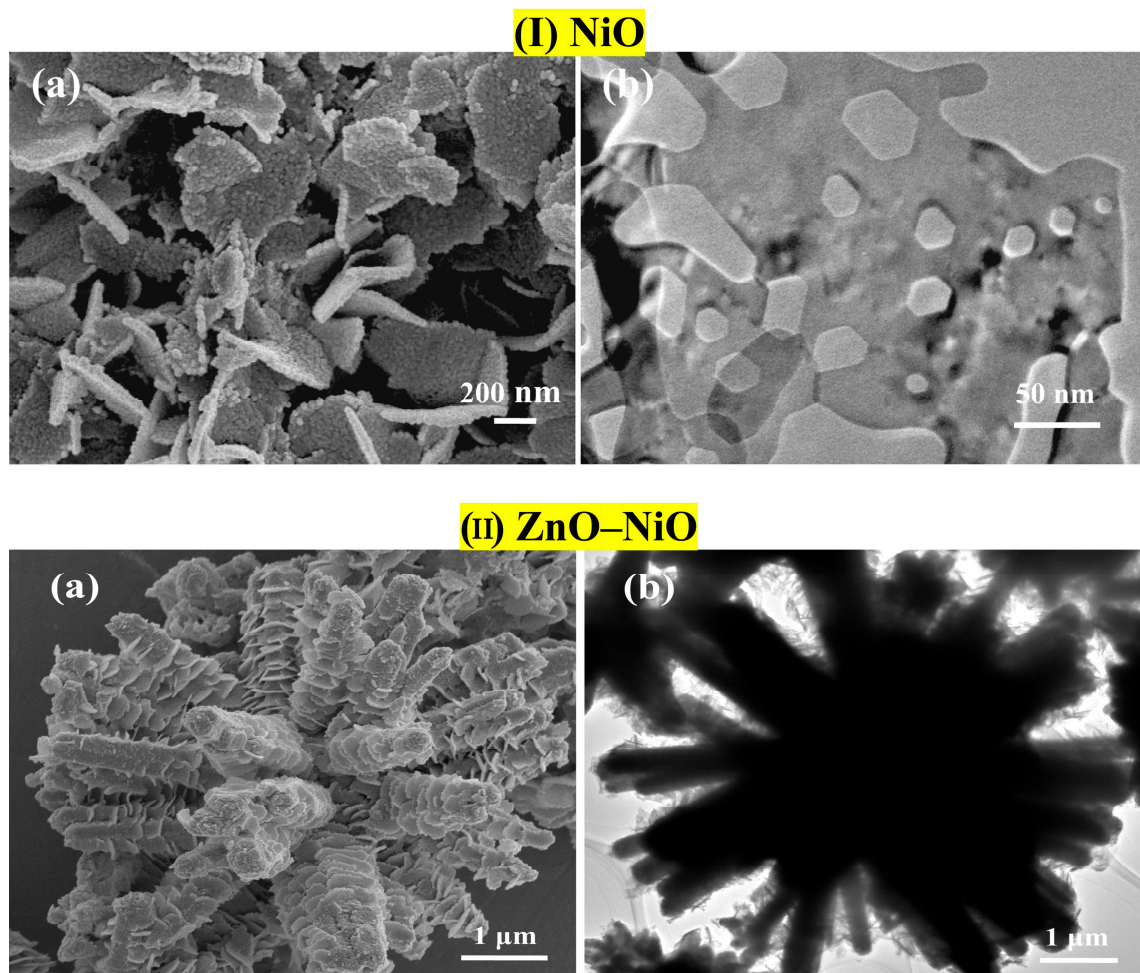


**Figure 35.** (**a**) SEM images and (**b**) TEM images of (**I**) pristine NiO and (**II**) ZnO–NiO composite, reproduced from reference [170] Elsevier publisher (Copyright 2017).

3.2.2. X = $SnO_2$

The hydrothermal growth of $SnO_2$_NiO nanocomposite has been made by Wei et al. [171] for gas sensing applications. They have demonstrated that the addition of tin dioxide allows reducing the operating temperature of pristine nickel oxide from 320 °C to 230 °C and enhances its sensitivity towards $NO_2$ 11-fold. This excellent response proves efficiency when increasing the gas concentration and good stability for 30 days, as shown in Figure 36.

Sputtering mixed composite of $SnO_2$–NiO on a glass substrate for sensor device fabrication is investigated in the reference [172], showing high sensing performances towards $NO_2$ at 200 °C, high selectivity against CO and $NH_3$, good reproducibility, and cyclic response stability over its single layer counterpart (NiO) (see Figure 37).
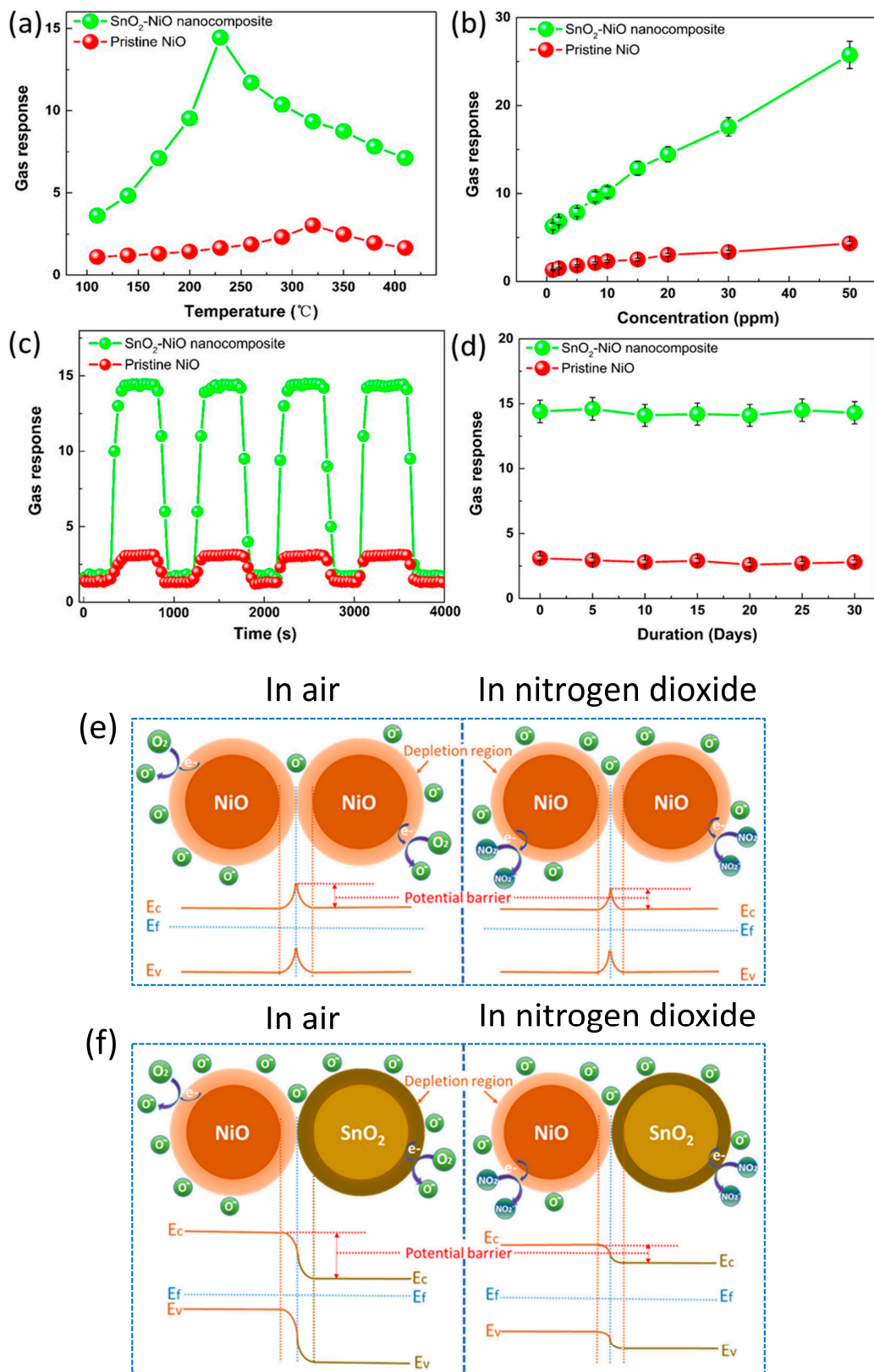
**Figure 36.** Sensing properties of pristine NiO and SnO$_2$–NiO composite: (**a**) gas response towards 20 ppm of NO$_2$ at different operating temperatures, (**b**) gas response at 230 °C to different gas concentrations, (**c**) dynamic curves at 230 °C under exposure to 20 ppm of NO$_2$, (**d**) stability test of the samples for 30 days, and schematic description of the sensing mechanism in the samples (**e**) NiO and (**f**) SnO$_2$–NiO in air and in gas with representation of band bending diagram, reproduced from reference [171] MDPI publisher (Copyright 2019).
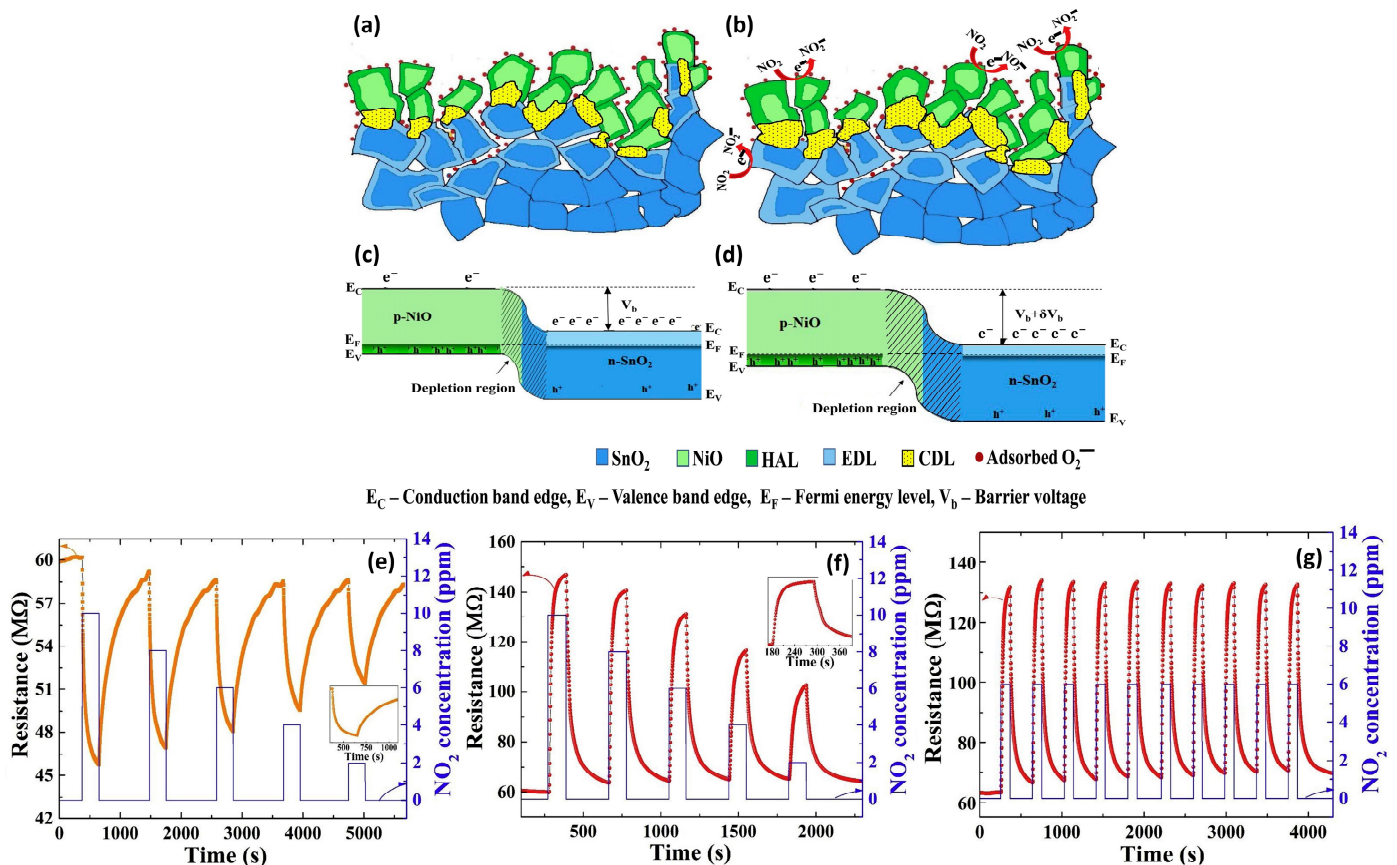
**Figure 37.** Schematic illustration of (**a,b**) sensing mechanism in the heterogeneous $SnO_2$–NiO composite and (**c,d**) band bending at the heterointerface in air and oxidizing gas environment, (**e**) gas response towards various concentrations of $NO_2$ at 200 °C for (**e**) NiO, (**f**) $SnO_2$–NiO composite, inset describes the sensing profile for a single $NO_2$ concentration and (**g**) its cyclic dynamic curves at 6 ppm, reproduced from reference [172] Elsevier publisher (Copyright 2020).

Another study reported an improvement in NiO sensitivity by changing its structure from pristine to $SnO_2$–NiO composite [173]. It demonstrates that the response of the composite is higher than the pristine NiO towards triethylamine (TEA). The widening of the depletion layer at the interface between the two oxides (NiO and $SnO_2$) has been found to increase the composite resistance in air. However, when the composite is exposed to TEA gas, a chemical reaction occurs where the adsorbed oxygen ions on the material surface react with gas molecules, releasing electrons and causing a decrease in interface depletion. This results in a reduction in the composite resistance. These findings suggest that the interaction between the composite and TEA gas can be utilized to control the electrical properties of the material and thus optimize its sensitivity towards gas species [173].

### 3.2.3. X = $In_2O_3$

Indium trioxide is sensitive to a variety of gases, including CO, $H_2$, $NO_x$, and VOCs. Gas sensing with $In_2O_3$ typically involves the measurement of changes in electrical conductivity upon exposure to the target gas. The high electron mobility and low electron trapping in $In_2O_3$ result in a high sensitivity to changes in gas concentrations. The combination of $In_2O_3$ and NiO results in a composite material that exhibits high sensitivity toward both reducing and oxidizing gases, making it a suitable material for gas-sensing applications in various environments. Yan et al. have investigated such composite and have revealed higher sensitivity against ethanol, compared to NiO, as mentioned in Figure 38 [174].
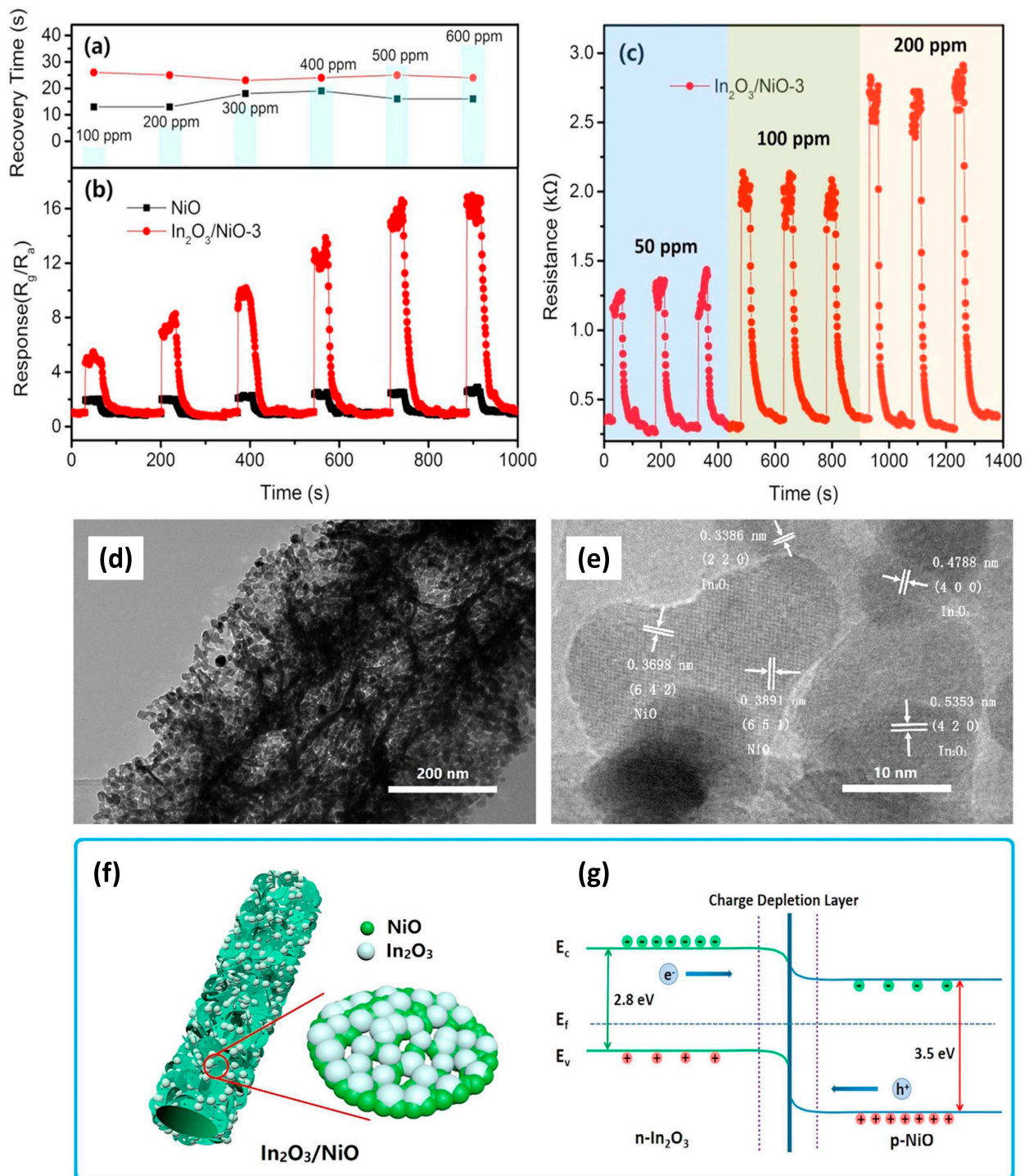
**Figure 38.** (**a**) Recovery time and (**b**) sensing response of pristine NiO and $In_2O_3$–NiO composite towards various concentrations of ethanol, (**c**) repeatability of composite sensor operating at 380 °C to 50 ppm, 100 ppm, and 200 ppm of ethanol, (**d**) TEM and (**e**) HRTEM images of the composite, and schematic illustration of (**f**) $In_2O_3$ nanoparticles on NiO nanosheets and (**g**) energetic diagram at the heterointerface $In_2O_3$–NiO, reproduced from reference [174] Elsevier publisher (Copyright 2022).

Another research group has studied the $In_2O_3$–NiO composite and has recorded higher sensitivity towards TEA when combining NiO with $In_2O_3$ with good repeatability, as mentioned in Figure 39 [175]. The excellent sensitivity of the composite is due to the larger specific surface area, which is 3.9 times higher than that of the pure NiO, and abundant mesopores contribute to enhancing the gas adsorption and diffusion.
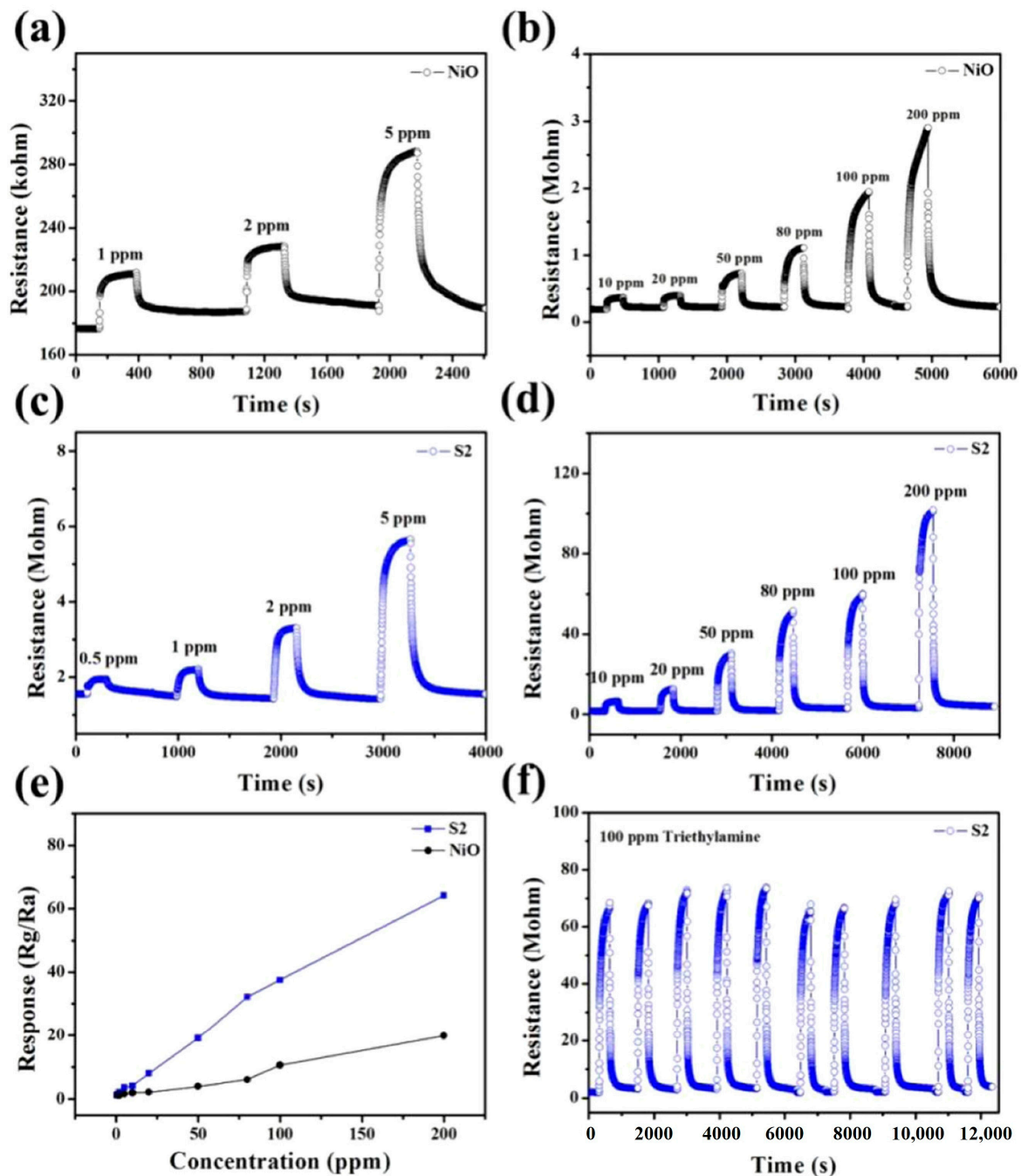
**Figure 39.** Transient resistance curves under exposure to various concentrations of TEA gas at 200 °C for (**a**,**b**) pristine NiO and (**c**,**d**) In$_2$O$_3$–NiO composite whose repeatability is evaluated in (**f**) and sensitivity is compared to the NiO sensitivity in (**e**), reproduced from reference [175] ACS publisher (Copyright 2021).

### 3.2.4. X = CeO$_2$

Ceria also proves its promotion in gas sensing applications [176] by operating at relatively low temperatures (100–150° C) and detecting different gases such as H$_2$, NO$_2$, CO$_2$, etc. [177,178]. Thanks to its properties, researchers devoted their studies to combining it with other materials, we mention here nickel oxide. Kabure et al. [179] have studied CeO$_2$–NiO composite, grown by microwave-assisted sol–gel synthesis, that shows high sensitivity towards NO$_2$ at 125 °C, in contrast with pure NiO that presents lower sensitivity and operates at higher temperature (175 °C). (See Figure 40).
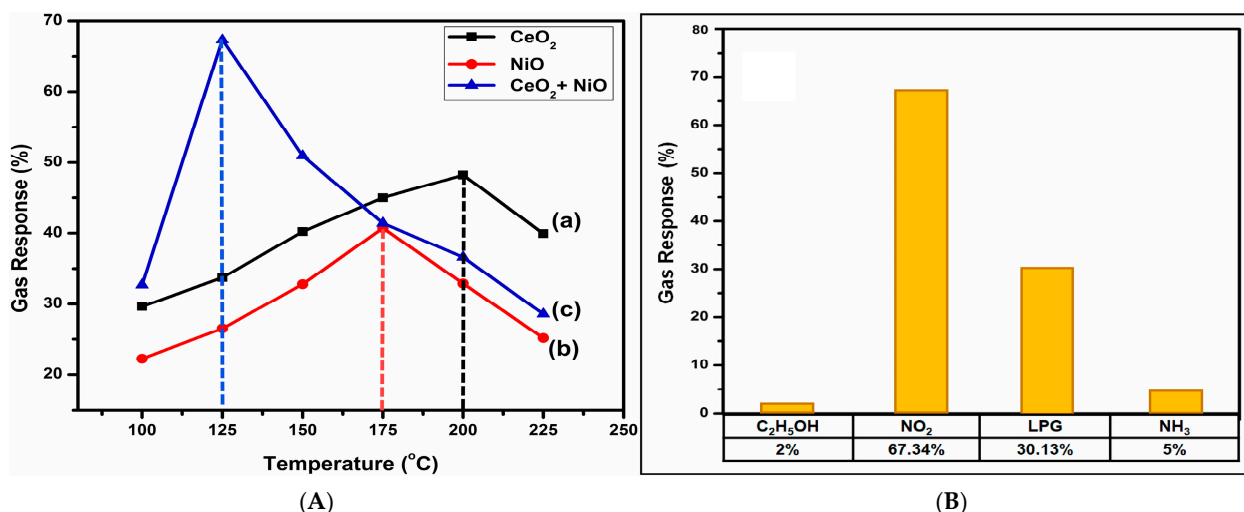
**Figure 40.** (**A**) Gas responsiveness of (a) $CeO_2$, (b) NiO, and (c) their composite towards $NO_2$ at different operating temperatures, and (**B**) (d) selectivity of $CeO_2$–NiO composite towards different gases at 125 °C, reproduced from reference [179] Elsevier publisher (Copyright 2022).

The as-spun $Ce_{1-x}Ni_xO_2$ nanocomposite led to the conception of a proficient gas sensor that is ultra-sensitive to propane with limited responsiveness to CO and $CH_4$ and operates at extremely high temperatures with an n-type sensing aspect. Its high selectivity is proved when compared to pure ceria and pure NiO and boosted by the independence of NiO on propane gas concentration. The selective $C_3H_8$ detection implies that the reaction kinetics with propane species is very fast. In such a reducing environment, the composite's resistance decrease indicates the n-type of $Ce_{1-x}Ni_xO_2$ [180].

Liu et al. give an interpretation to make the sensing mechanism more understandable. Under the first exposure to propane, the nanocomposite releases the adsorbed oxygen species and reduces the cerium and nickel ions to $Ce^{3+}$ and $Ni^0$, leading to highly reduced ceria and partially reduced NiO in the backbone with the formation of Ni nanoparticles on the surface of the sensing material when further expose it to reducing gases which can demonstrate its high responsiveness. Increasing the exposure time allows the material species reduction in the opposite direction and maintains a relatively high sensitivity towards all three gases.

3.2.5. X = $Fe_2O_3$

Iron oxide is a prominent example of n-type metal oxides that have garnered significant attention in gas sensing applications [181,182]. Its inclusion can substantially augment the sensitivity and performance of NiO-based sensors, making it a valuable component in the quest for enhanced gas detection capabilities. Pan et al. [183] have improved the sensitivity towards n-butanol of NiO sample three-fold by loading $Fe_2O_3$ nanosheets that also enhance the selectivity of such material towards several gases: ethanol, methanol, formaldehyde, TEA, acetone, $NO_2$, and n-butanol, decrease the detection limit of n-butanol from 296 ppb to 48 ppb, reduce the operating temperature from 230 °C to 200 °C due to surface activity improvements, and maintain high stability and good reproducibility at 200 °C (see Figure 41).

The $Fe_2O_3$–NiO composite, hydrothermally-grown, has also been investigated in Wang's work [184], showing high responsiveness towards toluene at 300 °C. Compared to the NiO sensor, the composite's sensitivity is 19-fold higher (See Figure 42). This can be attributable to the high surface area, the good permeability, and the p–n junction formation that creates a hole depletion layer and hence increases the adsorbed oxygen species, leading to releasing back the electrons to the composite.
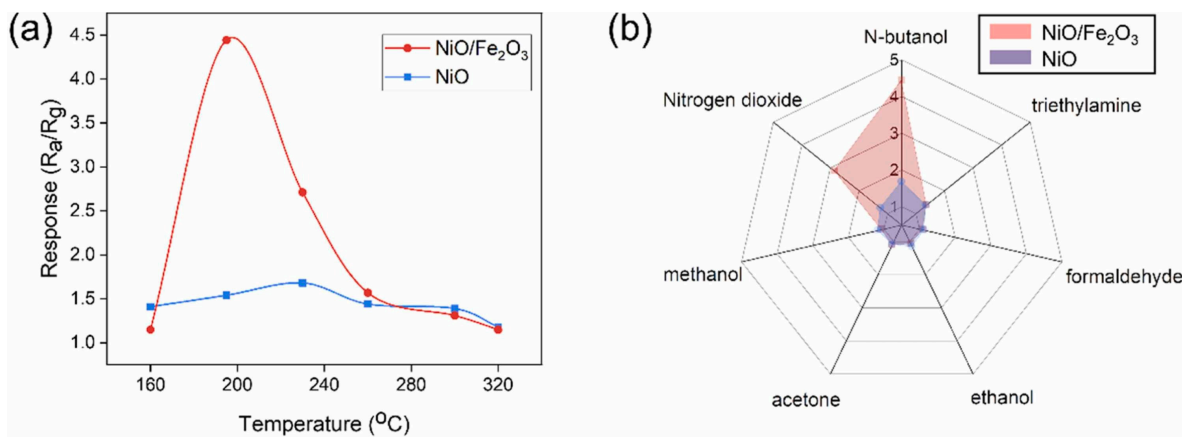
**Figure 41.** (**a**) Responsiveness to 10 ppm of n-butanol of NiO and $Fe_2O_3$-NiO sensors at different operating temperatures, and (**b**) selectivity towards different gases, reproduced from reference [183] Elsevier publisher (Copyright 2022).
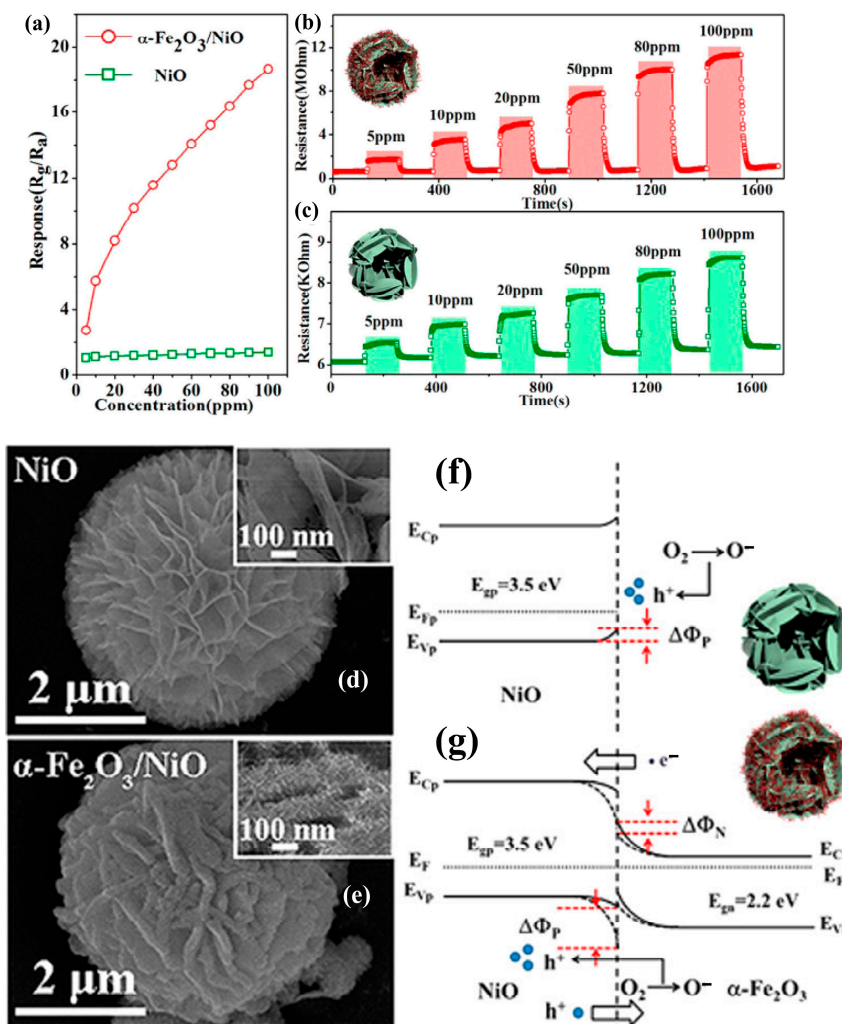


**Figure 42.** (**a**) Response to toluene of pure NiO and $Fe_2O_3$–NiO composite under different concentrations at 300 °C. Dynamic response of the $Fe_2O_3$–NiO composite (**b**) and the pure NiO (**c**) to different concentrations of toluene. (**d**,**e**) SEM images and schematic representation of carrier transport at the interface for (**f**) NiO and (**g**) $Fe_2O_3$–NiO composite, reproduced from reference [184] ACS publisher (Copyright 2014).

Using LJS, Hernández et al. prepared a nanocomposite of Fe–Ni oxide that shows good sensitivity towards acetone, ethanol, and toluene, behaving as n-type metal oxide. However, under its exposure to 200 ppb concentrations of $NO_2$, the composite $NiFe_2O_4$ shows noisy responsiveness that might be related to the poor connectivity of the nanoparticles [58].

### 3.2.6. X = $Co_3O_4$

To our knowledge, the catalytic effect and the abundant oxygen adsorption of several p-type metal oxides promote the selective oxidation of volatile organic compounds, especially the oxidizing gases, and ensure better sensitivity at low operating temperatures [185]. Therefore, making cobalt oxide and nickel oxide in the composite will enhance the sensitivity toward various gases, as can be seen in Figure 43 [186]. In fact, the isotype p–p heterojunction is more favorable than the p–n heterojunction as it allows the spatial separation of charge carriers and keeps the majority of the carriers' densities unvaried, maximizing the gas interaction with the sensing layer and improving its responsiveness [187]. In the $Co_3O_4$–NiO composite, the Ni ions provide electrons to $Co_3O_4$; hence, the density of electrons will be enhanced, leading to higher sensitivity.



**Figure 43.** Responsiveness of pure NiO, $Co_3O_4$, and their composites towards ethanol (**a**) at different operating temperatures and (**b**) at various concentrations at 250 °C, (**c**) Dynamic resistance of the composite towards 100 ppm of ethanol, and (**d**) its selectivity against several gases, reproduced from reference [186] Elsevier publisher (Copyright 2022).
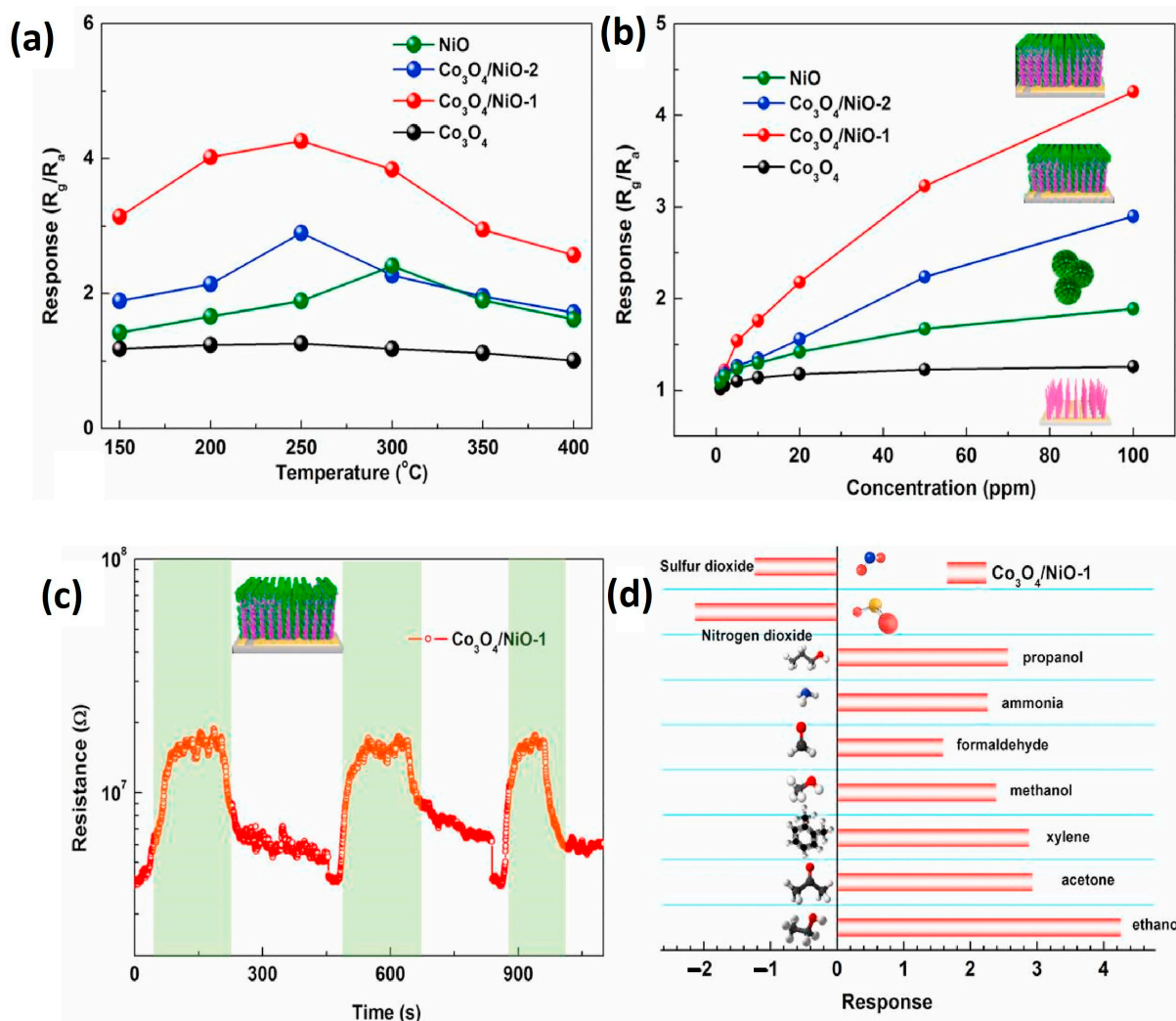
Another work has designed hierarchical nanostructures of NiO, $Co_3O_4$, and their composite to evaluate their responsiveness toward hydrogen [188]. Govindhan et al. have proved high $H_2$ sensitivity for nickel–cobalt oxide sensors working at elevated temperatures in contrast to the two pure oxides. They have ascribed this excellent performance to the architecture, the nanosized pores, and the large surface area of the p-type composite that also shows high selectivity toward $H_2$. The surface-dependent sensing mechanism is subject to the chemisorption of oxygen and hydrogen on the composite oxide's surface, allowing its resistance to increase. Further increases in temperature (up to 600 °C) induce donor-like oxygen vacancies in NiO and change the p-type doping to n-type doping so that the isotype heterojunction is transformed to p–n heterojunction with high sensitivity and selectivity toward hydrogen, which can provide practical functionality for advanced combustion monitoring. Such properties are exhibited in Figure 44.
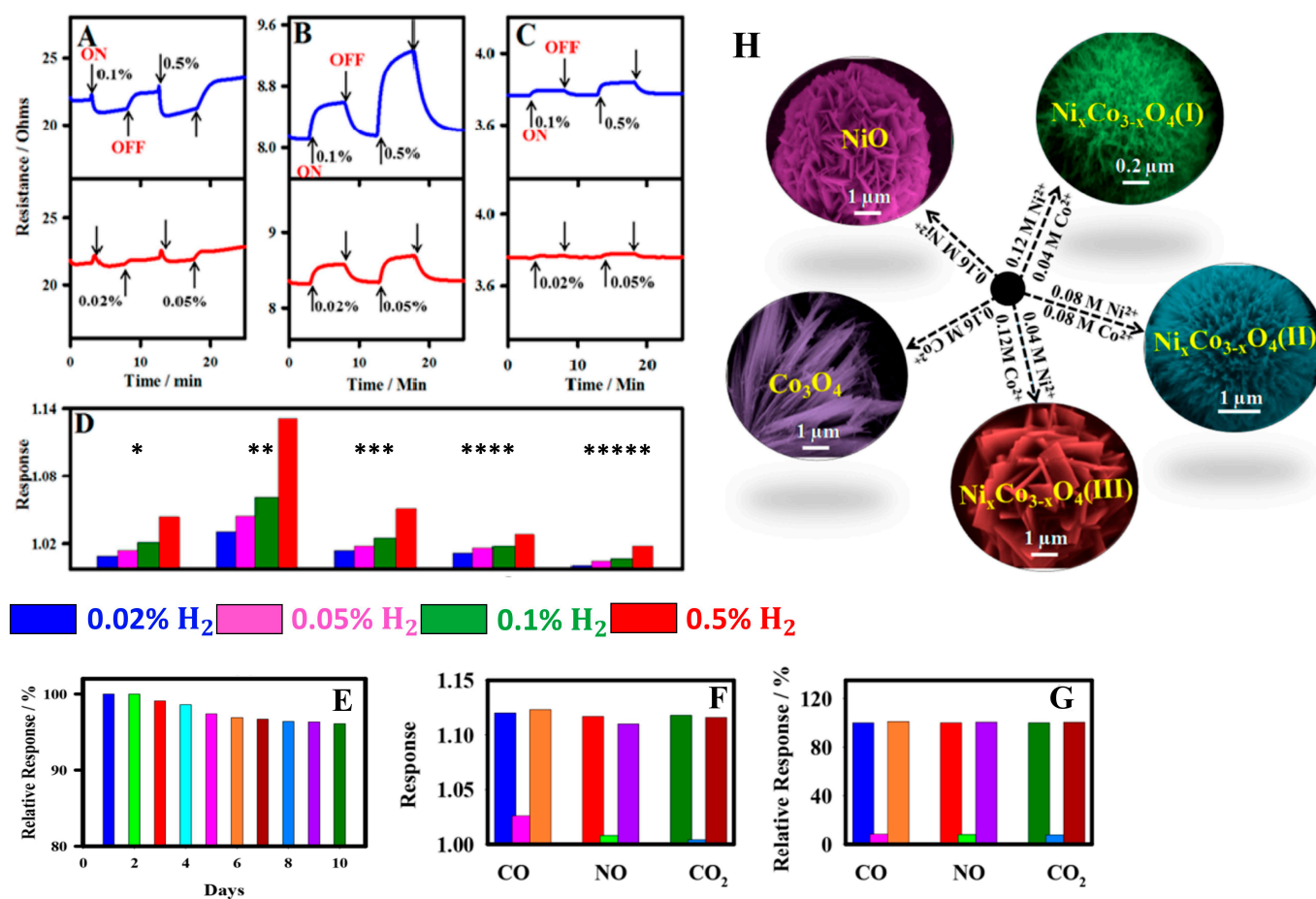


**Figure 44.** Sensing performances of hierarchical Ni–Co composite oxide, hydrothermally grown, reproduced from reference [188] ACS publisher (Copyright 2018). Sensor response to $H_2$ with different concentrations at 600 °C for (**A**): NiO, (**B**): $Ni_xCo_{3-x}O_4$ (I), and (**C**): $Co_3O_4$, (**D**): histogram representation of sensing response to different gas concentrations at 600 °C for * NiO, ** $Ni_xCo_{3-x}O_4$ (I), *** $Ni_xCo_{3-x}O_4$ (II), **** $Ni_xCo_{3-x}O_4$ (III), and ***** $Co_3O_4$, (**E**): stability performance of $Ni_xCo_{3-x}O_4$ (I), (**F**): gas response toward CO, NO, and $CO_2$, (**G**): relative response toward CO, NO, and $CO_2$, and (**H**): schematic illustration of hierarchical nanostructured $Ni_xCo_{3-x}O_4$ materials prepared by hydrothermal and calcination methods.

### 3.2.7. X = CuO

The addition of CuO to the NiO sample results in improved sensing properties of the sensor compared to bare NiO. This finding is reported in the literature, where Sui et al. [189] proved enhanced properties of such a composite, which include higher response and faster

recovery time when detecting 5 ppm of $H_2S$ at 133 °C (See Figure 45). These improvements can be explained by the chemical and electronic sensitization induced by the CuO addition. The catalytic activity of CuO primarily dominates the chemical sensitization process. When the NiO nanowall arrays are decorated with CuO, the surface of CuO/NiO can adsorb more oxygen molecules, which are more easily dissociated into reactive chemisorbed oxygen. Additionally, CuO can moderately enhance the chemical activity of $H_2S$ and increase its chances of adsorption on the surface, resulting in greater gas adsorption. Furthermore, the presence of CuO also contributes to a faster recovery speed due to its role as a catalyst, promoting the recovery processes that involve adsorption, dissociation, and ionization of oxygen molecules.
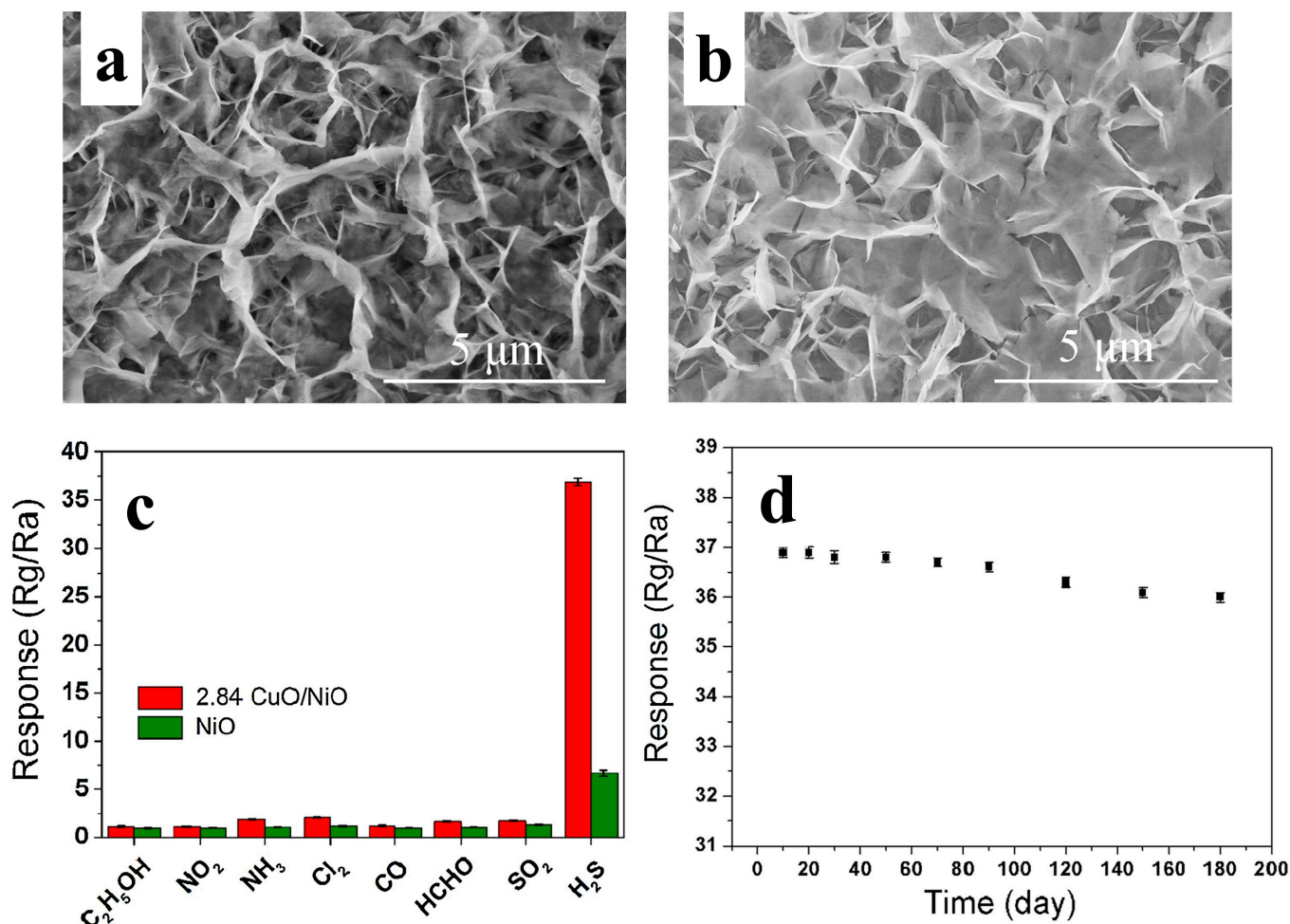


**Figure 45.** SEM image of (**a**) CuO–NiO composite precursor and (**b**) CuO–NiO composite nanowall arrays on ceramic tube, (**c**) selectivity performance of the composite compared to pristine NiO towards various gases, and (**d**) evaluation of composite sensor stability, reproduced from reference [189] Elsevier publisher (Copyright 2020).

The CuO–NiO composite shows its promotion in the gas sensing field thanks to its structural properties and its reactivity with several gases, such as $H_2S$, as presented in Figure 46.

To interpret the sensing mechanism in such a composite whose interface differs from the previous composites' interfaces by the type of junction, Figure 47g–j shows that NiO and CuO form p–p heterojunctions, noting that the NiO work function is higher than the CuO one, which causes holes to migrate from NiO to CuO through the heterojunction to equalize the Fermi levels. This results in the creation of a hole depletion layer and hole accumulation layer at the interface on the side of NiO and CuO, respectively. The

enrichment of holes reduces the adsorption of oxygen, weakening the oxidation of $H_2S$ on the surface of CuO, as per the following equation: $O_2(ads) \rightarrow O_2^- + h^+$. Additionally, the catalytic activity of NiO strengthens the synergetic effects in such composite by enhancing the oxygen chemisorption that increases the oxidation rate of the gas species (NiO role). It is worth noting the role of CuO in maximizing the adsorption of gas molecules on the metal oxide surface where the potential barrier hinders the transport of electrons through the composite and consequently provides extra electrons for oxygen species to be adsorbed on the sensing surface, hence improving the gas detection performance [187–191].
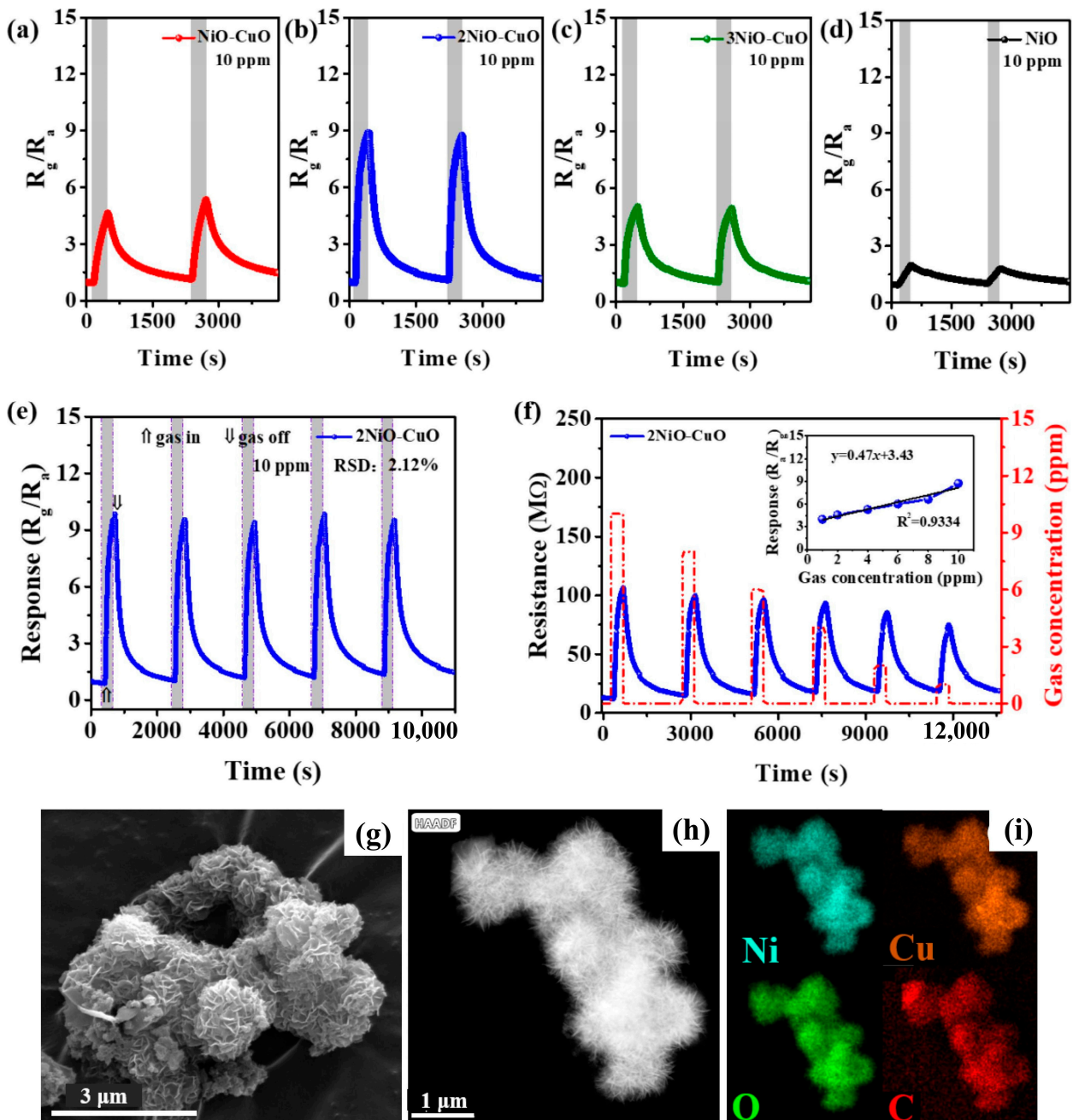


**Figure 46.** Dynamic responses towards 10 ppm-$H_2S$ at room temperature of CuO–NiO composite at different ratios (**a**) 1:1, (**b**) 2:1, (**c**) 3:1, and (**d**) pristine NiO. (**e**) Repeatability of the composite sensor at a ratio of 2:1 and its (**f**) transient resistance to various gas concentrations (inset: response towards 1–10 ppm $H_2S$). (**g**) SEM image, (**h**) TEM image, and (**i**) elemental mapping of the composite, reproduced from reference [190] Elsevier publisher (Copyright 2023).
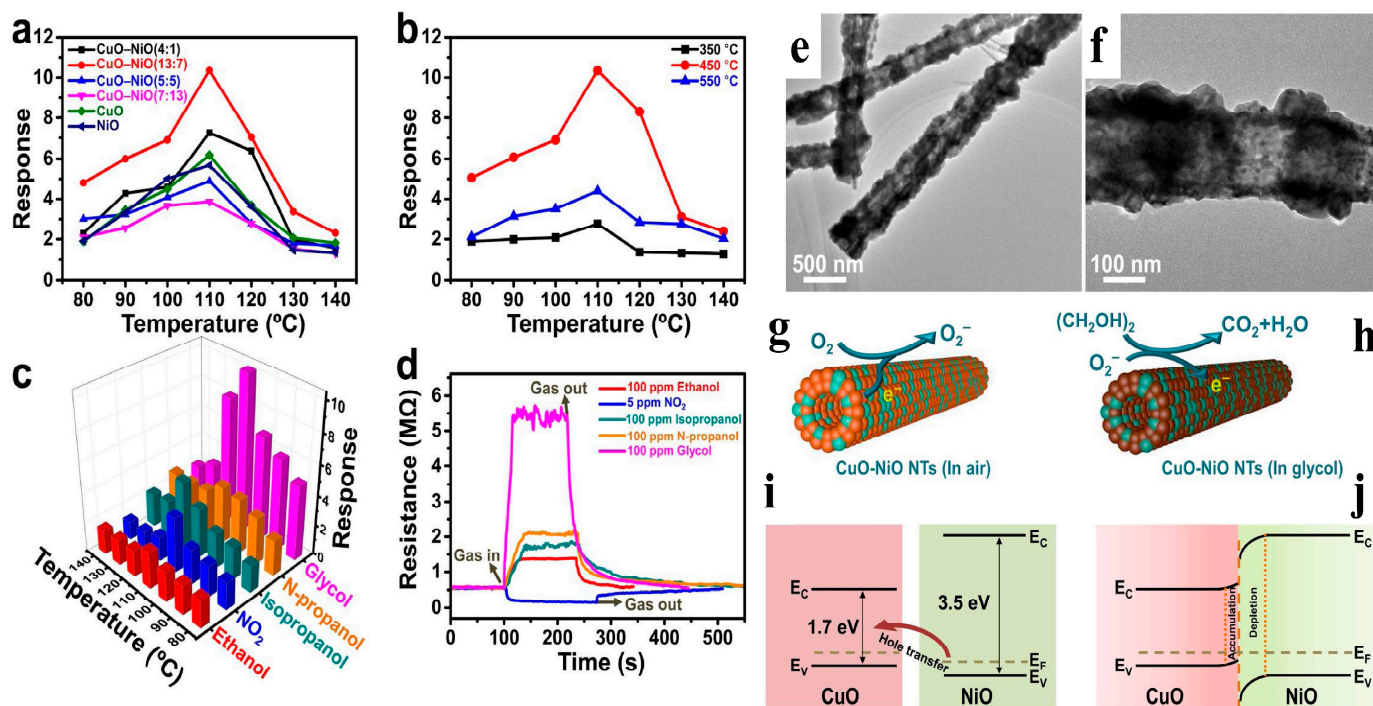
**Figure 47.** Dynamic response towards 100 ppm of glycol for (**a**) CuO-NiO composite at different ratios and (**b**) CuO–NiO (13:7) at different operating temperatures, its selectivity (**c**) and its transient resistance curves (**d**) against various gases, (**e**,**f**) TEM images of CuO–NiO (13:7) at different magnifications, (**g**–**j**) illustrative representation of sensing mechanism in the p–p heterojunction before and after gas exposure, reproduced from reference [187] Elsevier publisher (Copyright 2020).

Also, CuO–NiO nanotubes demonstrate the highest sensitivity toward glycol at 110 °C as the optimum operating temperature, as shown in Figure 47a–c [187].

Table 4 summarizes the sensing properties of X–NiO composites recently reported in the litterature.

**Table 4.** Summary of X–NiO composite gas sensors, reported since 2022.

| X-NiO | Structure | Target Gas | Operating Temperature (°C) | Response | Response Time/Recovery Time (s/s) |
|---|---|---|---|---|---|
| X = ZnO | Hollow microspheres [192] | Toluene (100 ppm) | 300 | 240 | 2/33 |
| | NPs-decorated hierarchical structure [193] | Isopropanol (100 ppm) | 280 | 52.4 | 8/50 |
| | Multi-junction interconnected structure [194] | Acetone (100 ppm) | RT | 6.06 | 28/34 |
| | NPs [195] | Ammonia (3000 ppm) | RT | 0.278 | 50/5–7 |
| | Nanofibers [196] | Ammonia (300 ppm) | RT | 0.46 | 100/25 |
| | Nanosheets [197] | Ammonia (18 ppm) | 35 | 0.558 | 8/28 |
| X = SnO$_2$ | One-dimensional nanorods/two-dimensional porous nanosheets heterostructure [198] | Ethanol (100 ppm) | 300 | 25.7 | 17/23 |
| | NPs-decorated thin film [199] | Formaldehyde (50 ppm) | 210 | 31.04 | 18/105 |
| | Double-layered heterostructure [200] | Sulfur dioxide (2 ppm) | 250 | 0.3 | 48/51 |
| | Composite [201] | Carbon oxide (400 ppm) | 350 | NA | 63/77 |
| | Nanocrystals/porous nanosheets structure [202] | Hydrogen (400 ppm) | 350 | NA | 29/49 |
| | NPs/nanocuboids [203] | Triethylamine (100 ppm) | 400 | 78.5 | <3/120 |
| | NPs-decorated thin film [199] | Ethanol (100 ppm) | 350 | 84 | 3/NA |

**Table 4.** *Cont.*

| X-NiO | Structure | Target Gas | Operating Temperature (°C) | Response | Response Time/Recovery Time (s/s) |
|---|---|---|---|---|---|
| X = Fe$_2$O$_3$ | Nanosheets/nano-prisms [183] | n-butanol (100 ppm) | 200 | 24.15 | 120/6 |
| | NPS/nanofibers [204] | Hydrogen (1000 ppm) | 250 | 199.24 | 11/105 |
| | Hollow-out loaded nanorods [205] | Ethanol (10 ppm) | 150 | 51.2 | NA |
| X = NiFe$_2$O$_4$ | Nanocubes with porous heterostructure [206] Fiber-in-tube heterostructure [207] | Trimethylamine (100 ppm) | 170 | 10.7 | 28.8/20.8 |
| | | Toluene (100 ppm) | 170 | 19 | 19.6/81.3 |
| | | Formaldehyde (100 ppm) | 170 | 24.9 | 10/11.6 |
| | | Triethylamine (100 ppm) | 170 | 56.4 | 11.2/14.4 |
| | | Ethanol (100 ppm) | 170 | 58.4 | 16.8/13.7 |
| | | Aniline (100 ppm) | 170 | 96.8 | 29.4/164.6 |
| | | Ethyl acetate (100 ppm) | 170 | 129 | 26/15.8 |
| | | Acetone (100 ppm) | 170 | 150.3 | 12.8/15.6 |
| | | Triethylamine (50 ppm) | 300 | 8.93 | 16/3 |
| X = In$_2$O$_3$ | Cuboid heterostructure [208] | n-butanol (100 ppm) | 350 | 412 | 6/<2500 |
| | Nanowires/three-dimensional porous foam [209] | Ethylene glycol (100 ppm) | 125 | 160.72 | 8.7/19.3 |
| | Porous nanoflower-like composite [210] | Methane (4000 ppm) | 340 | ~2 | NA |
| | Nanospheric composite [211] | Carbon oxide (300 ppm) | 280 | ~8 | NA |
| | Flower-like microspheres with nanoneedles [212] | N-propanol (100 ppm) | 250 | NA | NA |
| | Nanowires/three-dimensional porous foam [209] | Trimethylamine (10 ppm) | 200 | 20.51 | 39/43 |
| X = TiO$_2$ | Nanosheets/nano-rods [213] NPs [214] | Hydrogen (1000 ppm) Carbon oxide (1000 ppm) Acetone (50 ppm) | 25 25 25 (under UV) 300 | 2.09 0.06 <6 ~25 | NA NA NA NA |
| X = CuO | Hydrangea-like composite [190] | Hydrogen sulfide (1 ppm) | 25 | 11 | NA |
| X = MnO$_2$ | Nanosheets [215] | Allyl Mercaptan (40 ppm) | 275 | 11.28 | 115/25 |
| X = In$_2$S$_3$ | Foam/thin film [216] | Ethylene glycol (100 ppm) | 150 | 180.39 | 11.43/6.16 |
| X = Ti$_3$C$_2$T$_x$ MXene | NPs/stacked accordion-like structure [217] | Ammonia (50 ppm) | RT | 6.13 | 60/19 |
| X = WO$_3$ | Ball-flower-like composite [218] | Nitrogen dioxide (10 ppm) | 200 | 16.06 | 9/13 |
| X = MoO$_3$ | Nanolamella [219] | Hydrogen (200 ppm) | RT | <1.5 | 60/148 |
| | Core-shell heterostructure (nanorods/nanosheets) [220] | Ethyl acetate (100 ppm) | 250 | 34.91 | 67/82 |

## *3.3. Modified NiO Structure with*

### 3.3.1. Noble Metal Nanoparticles NPs

The enhancement of gas sensitivity of metal oxides by noble metals is attributed to their catalytic properties. Noble metals such as gold, platinum, silver, and palladium have high catalytic activity due to their ability to adsorb and dissociate gas molecules on their surface. When these noble metals are decorated on the surface of metal oxides such as nickel oxide, they act as catalytic sites for gas reactions, promoting the dissociation and adsorption of gas molecules on the surface of the sensor. The decoration of noble metals on the surface of metal oxide gas sensors can enhance the sensing mechanism in several ways. Firstly, noble metals can increase the surface area and modify the surface properties of the metal oxide, leading to a higher number of active sites for gas adsorption and reaction. Secondly, noble metals can modify the electronic structure of the metal oxide, leading to a change in its electrical conductivity upon gas exposure. Finally, noble metals can act as

electron acceptors or donors, modifying the electrical conductivity of the metal oxide and enhancing its sensitivity to gases.

Briefly, there are two main phenomena that shape the metallic decoration of nickel oxide: (i) electronic sensitization [221] (Fermi level shifting) and (ii) chemical sensitization (spillover effect) [222].

- The electronic sensitization mechanism in NiO decorated with noble metals can be explained using the Schottky barrier theory. According to this theory, when a metal is in contact with NiO, a potential barrier is formed at the interface due to the difference in work function between the metal and the semiconductor. The transfer of electrons from the noble metal to the NiO surface or vice versa depends on the work function of each component, leading to the formation of a depletion layer at the NiO/noble metal interface. The presence of the depletion layer increases the surface reactivity of the NiO, so it enhances its gas-sensing performance.

- Upon exposure to a gas, the noble metals catalyze the oxidation or reduction of gas molecules on the surface of the sensor, leading to a change in its electrical conductivity. The change in conductivity is proportional to the gas concentration, allowing the sensor to detect the presence and concentration of the gas. The chemical sensitization mechanism in nickel oxide decorated with noble metals can be explained based on the Langmuir–Hinshelwood (LH) model. According to this model, the reaction between the gas molecule and the surface of the sensor occurs in two steps: adsorption and reaction. The reactant molecules are first adsorbed onto the sensing surface, where they form reactive intermediates that can subsequently react with other adsorbed species or desorb back into the gas phase.

Rai et al. have studied Au-functionalized NiO nanoparticles as Au–NiO yolk–shell nanostructure with a response to $H_2S$ approximately four times higher than that of bare NiO hollow nanospheres [223].

To better understand the effect of noble metals on the NiO sensing performances, a schematic representation of the band alignment of NiO and Pd in air and in a reducing environment is shown in Figure 48. Due to the difference in work functions between NiO and Pd, a potential barrier exists at the interface, resulting in the formation of a depletion layer at the interface. The Fermi level of NiO is higher than that of Pd due to the difference in work functions, and electrons tend to flow from Pd to NiO to establish an equilibrium. As a result, the depletion layer is enriched in positive charges on the NiO side and negative charges on the Pd side.

After exposure to a reducing gas, such as hydrogen ($H_2$), Pd metal interacts with the target gas, leading to a formation of the PdH component and a decrease in the work function from 5.6 eV to 3.2 eV. The reduction of Pd and the consequent increase in electron concentration at the interface NiO/Pd in a gas environment leads to a shift in the Fermi level of Pd towards the conduction band of NiO. On the NiO side of the interface, the electrons that are transferred from the Pd side combine with the holes in the valence band of NiO, leading to the formation of a hole accumulation layer (HAL). This process is driven by the formation of an electric field at the interface due to the difference in Fermi levels between NiO and Pd.

The HAL is typically characterized by a high concentration of holes, which are trapped at defects and impurities in the NiO lattice. The presence of the HAL enhances the sensitivity of NiO/Pd-based gas sensors to reducing gases, as the holes in the HAL can react with the reducing gas species and lead to a significant increase in sensor resistance.

Ahmad et al. have also shown how the surface modification of NiO nanosheets by Au NPs enhances the synergetic effect and enlarges the surface area, thereby ensuring high sensitivity next to good reproducibility and selectivity toward hydrazine [224] (see Figure 49).
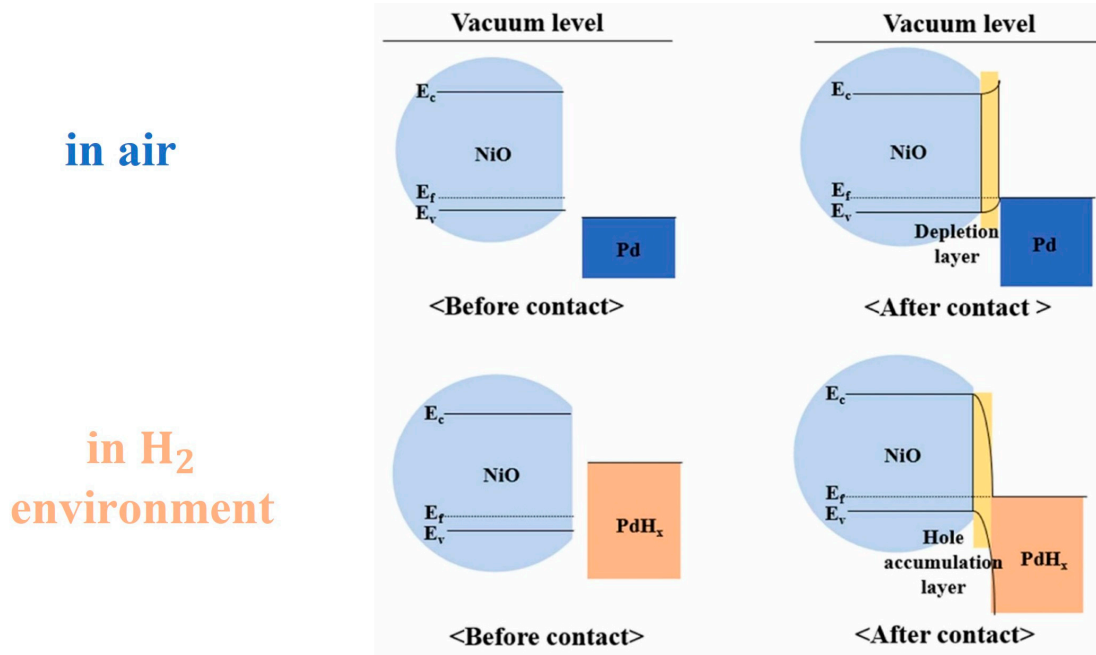
**Figure 48.** Description of band alignment between NiO and Pd before and after contact in air and in reducing environment, reproduced from reference [204] Elsevier publisher (Copyright 2023).
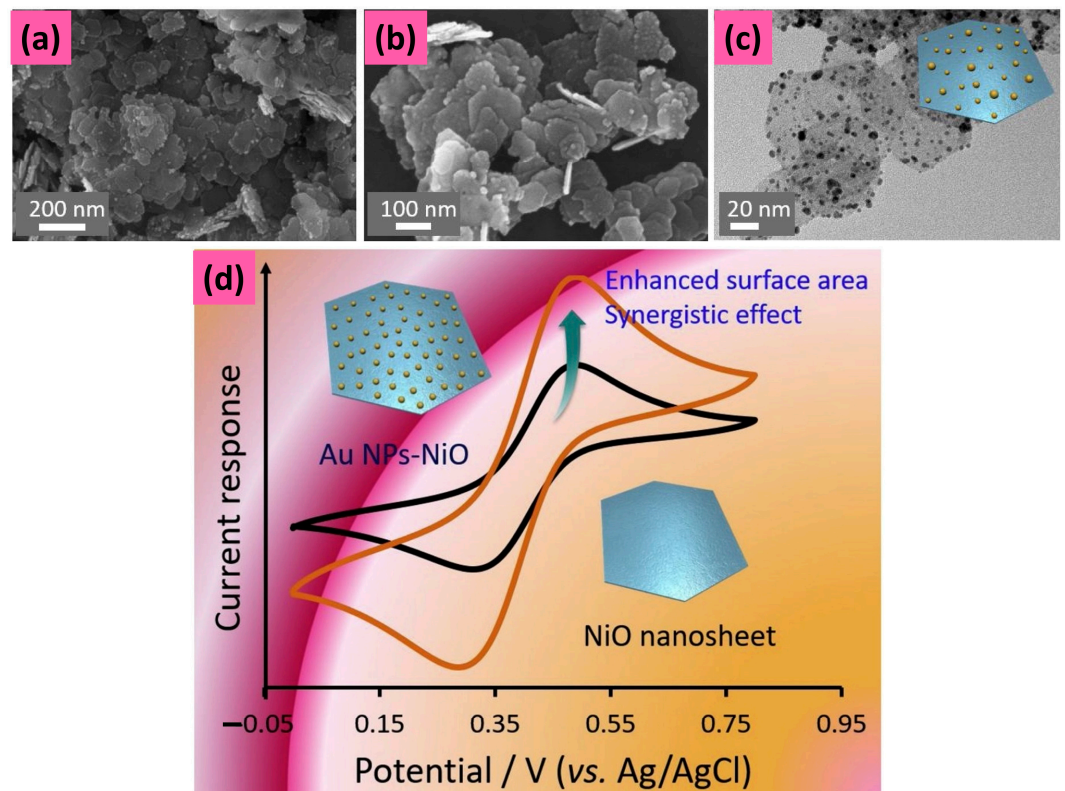


**Figure 49.** (**a**,**b**) SEM and (**c**) TEM images of Au-decorated NiO nanosheets and (**d**) a schematic illustration of its improved performance compared to the NiO nanosheets, reproduced from reference [224] Elsevier publisher (Copyright 2019).

Another interesting research report is that silver nanoparticles play the role of bridge between NiO and $TiO_2$ nanostructures, leading to combining the effects of p–n heterojunction and Schottky potential barrier to enhance the sensor's response to acetone gas [225]. In fact, Ag NPs formed at the granular interfaces of NiO–$TiO_2$ heterojunction accumulate

electrons and induce a Schottky barrier at the p–n interfaces, which increases the sensor resistance in air. Under its exposure to acetone, the interaction between gas molecules and the surface-adsorbed oxygen species causes electron transfer and lowers the charge carrier's density in the p-type NiO domains, resulting in an increase in the resistance of the sensor since the height of the Schottky barrier is significantly increased. In Figure 50, a comparative study of the sensing response of different sensors assigns the highest response toward acetone to the Ag-decorated sensor at 90 °C (see Figure 50a) justified by the smallest diameter of the arc semicircle in the Nyquist-plot (see Figure 50b) that implies an improvement in the charge transfer across the interface, compared to the other curves. The Ag NPs act as an intermediate layer between the two semiconductors, responsible for slowing the electron recombination at the p–n heterointerface (see Figure 50c). Figure 50d clearly shows the role of Ag NPs in an acetone environment.

In Table 5, we cite some research works studying the sensing properties of NiO functionalized by metallic nanoparticles.

**Table 5.** Application of metallic NPs-functionalized NiO in gas sensing devices.

| Structure | Noble Metal | Gas Species | Temperature (°C) | Response | Response Time/Recovery Time (s/s) |
|---|---|---|---|---|---|
| NiO yolk–shell nanoparticles [223] | Au | $H_2S$ (5 ppm) | 300 | 108.92 | NA |
| NiO microspheres [226] | Pd | $NO_2$ (1.8 ppm) | 50 | 1.33 | 430/936 |
| NiO nanotubes [227] | Pt | Ethanol (100 ppm) | 200 | 20.85 | NA |
| NiO thin film [228] | Au | $H_2$ (2000 ppm) | 128 | <20 | NA |
| NiO thin film [229] | Pt | $H_2$ (3% $H_2$/air) | 45 | 305 * | NA |
| NiO–$TiO_2$ composite [225] | Ag | Acetone (100 ppm) | 90 | ~0.70 | 25/40 |
| NiO–$Co_3O_4$ composite [230] | Pt | $H_2S$ (100 ppm) | 200 | 250 | 213/135 |
| NiO microspheres [226] | Pd | $NO_2$ (1.8 ppm) | 250 | 203 | 73/169 |
| NiO thin film [231] | Pt | $NH_3$ (1000 ppm) | 300 | 1278 | 15/76 (at 350 °C) |
| NiO nanoparticles [232] | Au | Ethanol (100 ppm) | 200 | 2.54 | 250/420 |
| NiO nanoparticles [233] | Ru | Ethanol (2000 ppm) | 350 | 35.9 | 35/NA |
| NiO nanoparticles [234] | Pd | 2-methoxy ethanol (100 ppm) | 25 | 4882 | 3.68/3.76 |
| NiO–ZnO nanocomposite [235] | Pd | $H_2$ (100 ppm) | 225 | 0.72 | NA |
| NiO film [236] | Pd | $H_2$ (0.7 ppm) | 130 | 0.135 | 600/NA |

* denotes the selectivity of $H_2$ against CO in air mixture [229].

To summarize, the addition of noble metallic nanoparticles can enhance the gas sensitivity of NiO-based sensors in several ways:

1. Increased surface area: The addition of such nanoparticles increases the surface area of the sensor, providing more sites for gas molecules to interact with the NiO surface.
2. Improved catalytic activity: Noble metallic nanoparticles act as a catalyst for the reaction between reducing gas molecules and oxygen species on the NiO surface, leading to an increase in the sensitivity of the sensor towards reducing gases.
3. Enhanced charge transfer: The addition of such nanoparticles can improve the charge transfer between the NiO and the gas molecules, leading to a more significant change in the electrical conductivity of the sensor upon exposure to reducing gases/oxidizing gases.
4. Reduced operating temperature: The presence of these metallic nanoparticles can lower the operating temperature of the sensor, allowing it to be used in applications where high temperatures are not practical.
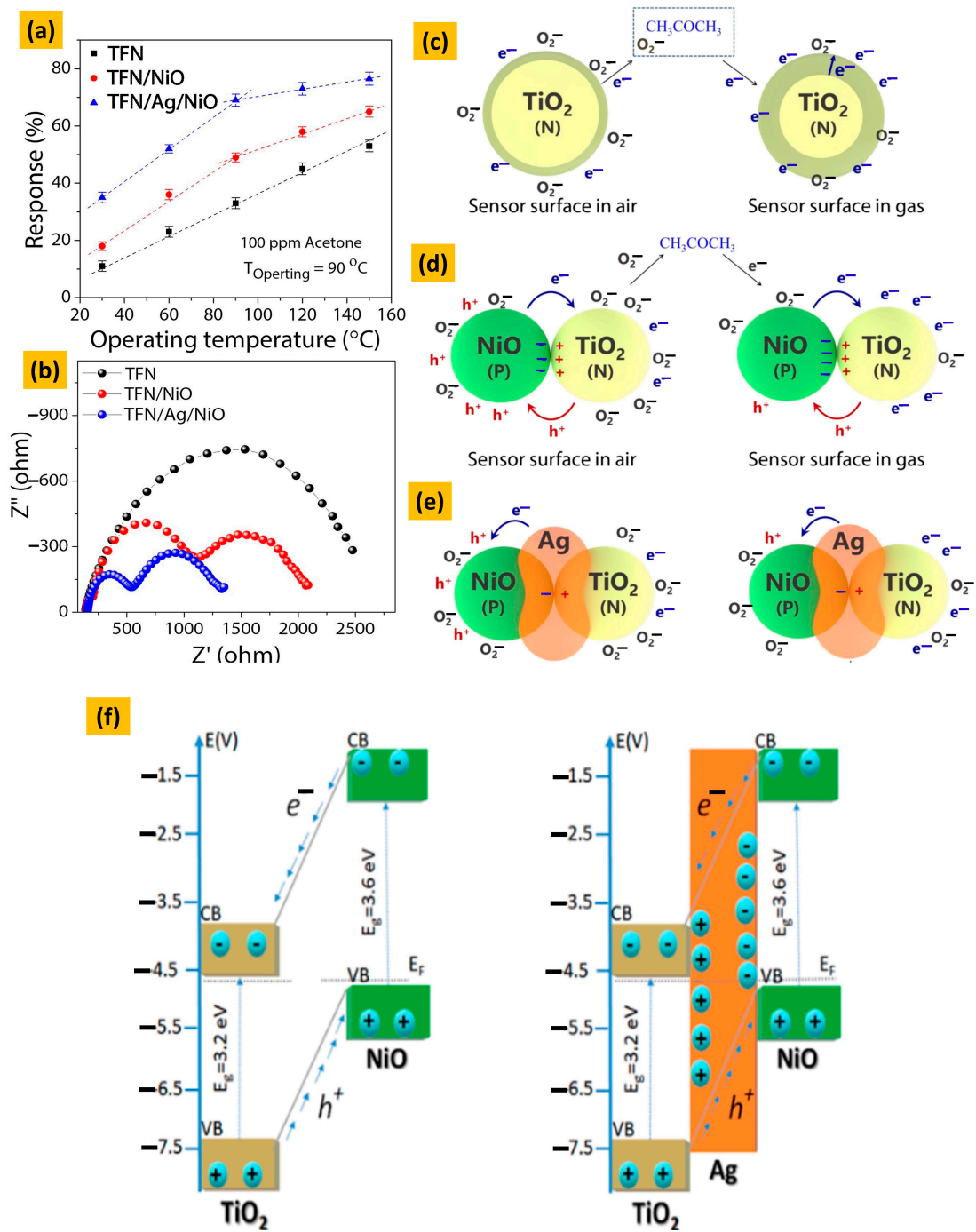
**Figure 50.** (**a**) Sensing performances towards acetone of three sensors (TiO$_2$, TiO$_2$–NiO, and TiO$_2$–Ag–NiO) at different operating temperatures, (**b**) their Nyquist-plots, mechanism of surface interaction of (**c**) TiO$_2$, and the composite NiO–TiO$_2$ before (**d**) and after (**e**) Ag–decoration in air and in reducing environment, and (**f**) band diagram of the composite NiO–TiO$_2$ before and after Ag-decoration, reproduced from reference [225] Elsevier publisher (Copyright 2022).

### 3.3.2. Carbon-Based Nanomaterials

The incorporation of carbon-based materials with NiO has been extensively researched in various fields: solar cells [237], batteries [238], supercapacitors [239], electrolytic cells [240], fuel cells [241], catalysts [242], biosensors [243–245], etc. Surprisingly, only a limited number of studies have explored the use of these composites in gas-sensing applications

despite their exceptional properties. In this context, we present the recent advancements in enhancing the gas sensitivity of NiO as a p-type chemo-resistive sensor.

Graphitic-based two-dimensional nanomaterials can enhance the gas-sensing performance of metal oxides in several ways. First, the large surface area of two-dimensional nanomaterials provides more active sites for gas adsorption and reaction compared to bulk materials. It is also worth mentioning their high carrier mobility at room temperature, next to the high carrier density and low resistivity. This can increase the sensitivity of gas sensors and lower the detection limit since their high electrical conductivity allows for efficient electron transfer between the gas molecules and the metal oxide, resulting in faster response times and improved sensitivity added to the low electrical noises [246]. Second, the unique electronic structure of two-dimensional nanomaterials, such as graphene or graphene oxide, can interact with gas molecules through π–π interactions or hydrogen bonding, resulting in enhanced selectivity towards specific gas molecules [247,248]. Finally, its incorporation into metal oxide-based gas sensors can also improve the stability and durability of the sensor [249].

Carbon soot is a material that holds promise as an integral component of gas sensors due to its desirable properties. It is highly conductive, porous, inexpensive, non-toxic, and stable. Carbon soot is composed of carbon nanoparticles which have an onion ring-like structure. Malepe et al. [250] used such material in optimizing NiO sensitivity towards mesitylene gas. They have proved mesitylene detection at low ppm-level at room temperature with short response/recovery times around 84 s/51 s. The unique properties of C nanoparticles, such as their high activity in transferring charges, their ultrahigh specific surface area, surface reactivity, and their highly disordered structure, make them effective not only at promoting chemisorption but also at providing ambient functionality to NiO sensor devices. This allows for a greater number of analyte molecules to be adsorbed onto the sensor surface, resulting in a more significant change in resistance and better sensitivity at room temperature (see Figure 51).
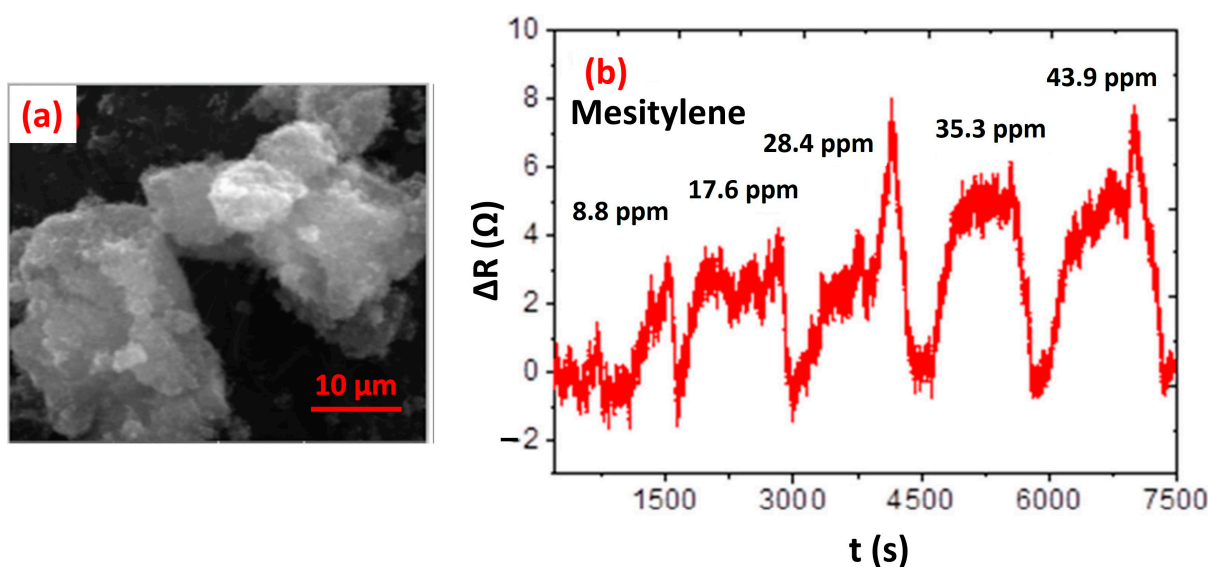


**Figure 51.** (**a**) SEM image and (**b**) dynamic response of carbon soot towards mesitylene gas at different concentrations, operating at room temperature, reproduced from reference [250] MDPI publisher (Copyright 2022).

Graphene is composed of a single layer of carbon atoms arranged in a hexagonal lattice structure and used as a functionalizing material for metal oxide gas sensors. In a metal oxide frame, graphene is reduced by being functionalized with oxygen-containing groups, known as rGO.

A low-temperature operable sensor with rapid response time is produced hydrothermally to give a hierarchical NiO and rGO hybrid structure. This composite shows ultra-high selectivity toward $NO_2$ with different responses at different weight fractions of GO, where the highest value is recorded at 21%, as can be seen in Figure 52. Indeed, under exposure to target gas, the $NO_2$ adsorption/desorption occurs faster due to the high electron affinity of gas molecules and the large specific surface area of the sensing composite, which leads to rapid electron transfer. Based on the low conductivity of NiO, the accumulation of further $NO_2$ molecules is restricted due to the presence of holes. In contrast, the transfer of hole carriers from the valence band of NiO to the rGO might help to decrease the holes' accumulation layer in NiO, thereby increasing the adsorption of $NO_2$. This ultimately leads to improved responsiveness and sensitivity of the material. Additionally, the rapid hole transfer from NiO to rGO improves the sensitivity by reducing the response time of the sensor [251].
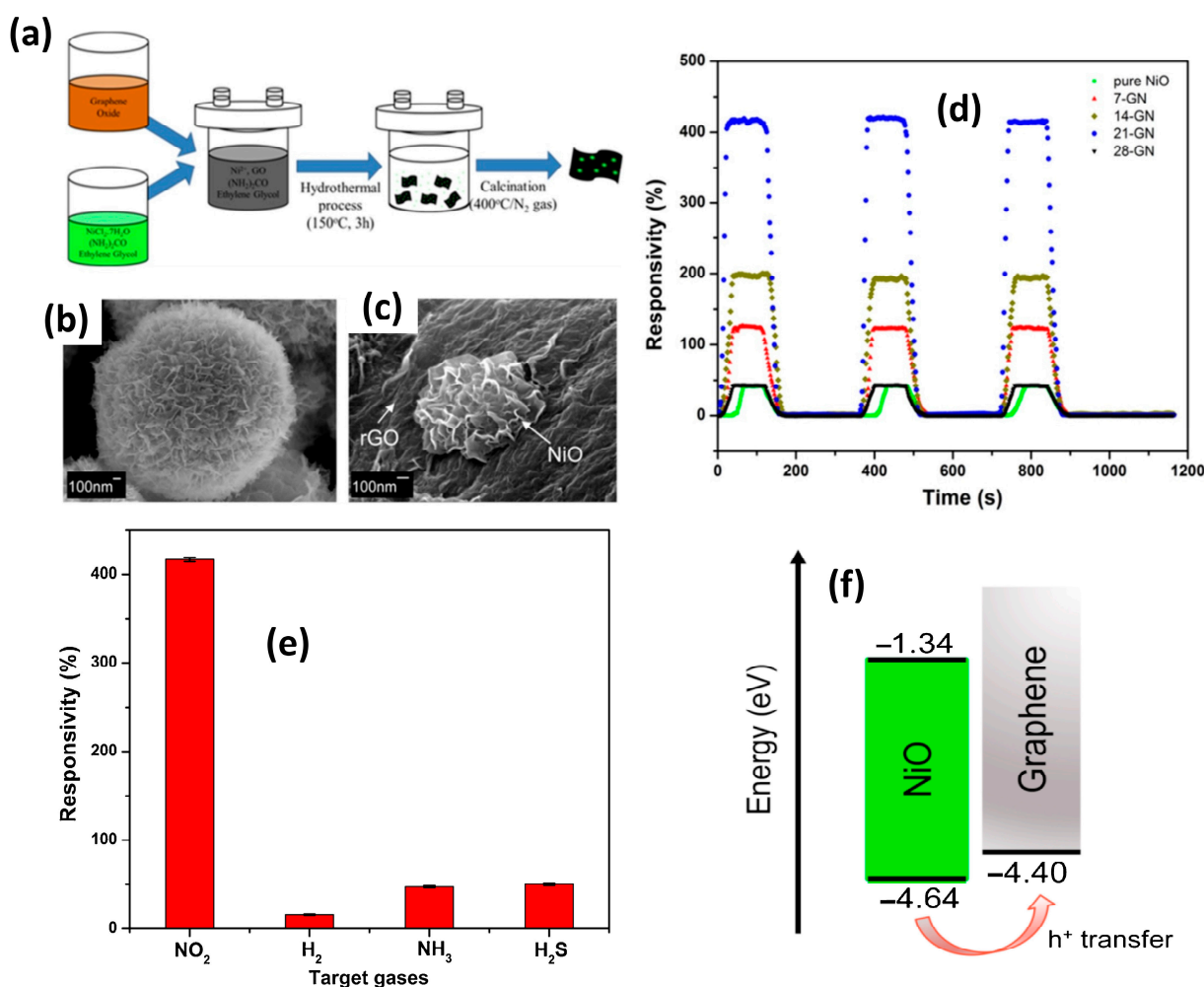


**Figure 52.** Hydrothermal growth of NiO–rGO nanocomposites devoted to efficient $NO_2$ sensor with high selectivity: (**a**) schematic illustration of growth process, (**b**) SEM image of pristine NiO, (**c**) SEM image of NiO–rGO, (**d**) dynamic response of pure NiO and NiO–rGO composites to $NO_2$ (**e**) responsivity of pure NiO and hybrid composites of NiO–rGO to 100 ppm of $NO_2$, and (**f**) energetic diagram of hole transfer from NiO to rGO, reproduced from reference [251] Elsevier publisher (Copyright 2016).

By using a facile solution-based process, another NiO–rGO sensor toward $NO_2$ is also made by Hoa et al. [252], showing high selectivity toward the oxidizing gas, as we described above, and very poor sensitivity toward reducing gases (See Figure 53). The

latter can be explained by the fact that when reducing gases interact with adsorbed oxygen on the surface of NiO, they release free electrons that neutralize the holes in NiO, therefore increasing the sensor resistance.
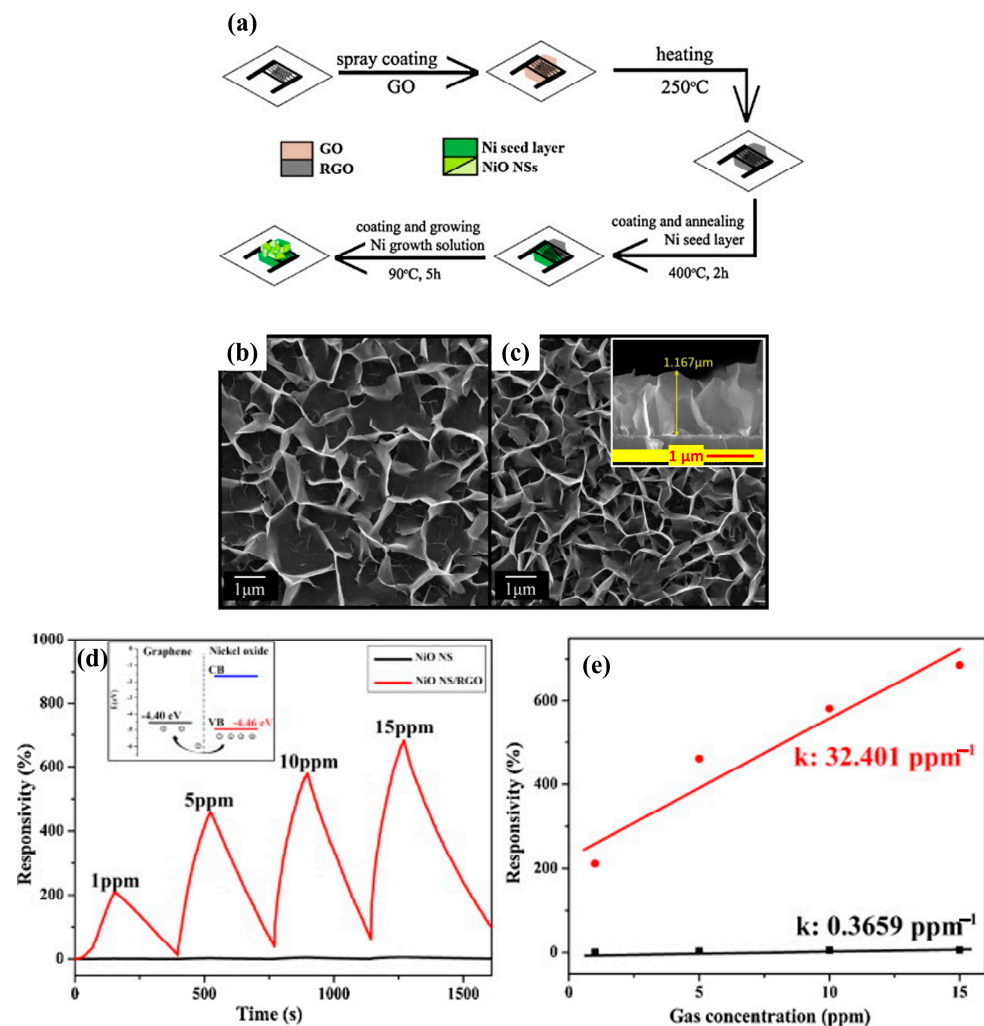


**Figure 53.** Preparation of NiO–rGO nanosheet composite by spray coating: (**a**) schematic illustration, SEM images of (**b**) NiO nanosheet structure and (**c**) NiO–rGO nanosheet structure, inset: cross-section SEM image, (**d**) dynamic response curve toward $NO_2$ at different concentrations, inset: energetic diagram of carrier transfer between graphene and NiO, (**e**) responsivity to different concentrations of $NO_2$ gas, reproduced from reference [252] Elsevier publisher (Copyright 2013).

The hydrothermal synthesized NiO–rGO hybrid nanocomposite shows high performance in gas sensing applications, as reported by Zhang et al. in 2016 [253]. The isotype heterojunction NiO–rGO enhances the NiO sensor's response toward methane six-fold due to not only the enlarged surface area but also the potential barrier at the heterointerface, which facilitates the adsorption and diffusion of methane molecules. The oxidation reaction between target gas molecules and oxygen species decreases the hole concentration as well as increases the sensor resistance. This sensor exhibits high selectivity toward methane at 260 °C [253].

Another study has focused on the rGO effect on NiO sensors operating at room temperature in two different $NO_2$ concentration ranges [142]. At concentrations between 0.25–1 ppm of $NO_2$, the sensitivity of pristine NiO was slightly higher compared to that of the NiO–rGO nanocomposite since some $NO_2$ molecules are physically adsorbed onto the rGO, preventing them from taking part in electron exchange with the NiO–rGO nanocomposite and subsequently decreasing its sensitivity. The high concentration range (7–60 ppm)

exhibited a remarkable improvement in the sensitivity of rGO–NiO. This increase in sensitivity was explained by the effective electron transfer between NiO and rGO, as well as by the increase in the specific surface area of NiO–rGO. Additionally, the nanocomposite displayed an accelerated recovery rate compared to pristine NiO, which was attributed to the higher electron mobility of rGO and the effective electron transfer between NiO and rGO.

Recently, graphene nickel oxide composite has been studied and proposed as a candidate for humidity sensors where a DFT calculation predicts its ability to interact highly with humidity [254].

Additionally, cylindrical tubes made of graphene sheets rolled up into a tube prove their ability to enhance the gas sensitivity of NiO.

Single-walled carbon nanotubes (SWCNT) combined with NiO have demonstrated room temperature operation, the highest sensitivity with a detection limit of 97 ppb, and the fastest response at the same level of NO concentration when comparing it to pristine NiO and SWCNT sensors. Good selectivity toward NO is also proven [255].

Multi-walled carbon nanotubes (MWCNT)–NiO composite have also shown an enhancement in sensor response compared to pristine NiO, operating at relatively low temperatures (180 °C) [256].

The improvement in the sensor response is often attributed to the higher surface area and interconnections of the metal oxide and carbon nanotubes. This composite structure provides more active sites for the adsorption of gas molecules, facilitating the transfer of the gas molecules over the barriers and ultimately decreasing the operating temperature. The enhanced sensitivity of the composite can be attributed to the synergistic effect of the two materials, whereby the carbon nanotubes facilitate electron transfer and provide a conductive pathway, while NiO provides a high surface area for gas adsorption [257–259] (see Figure 54).
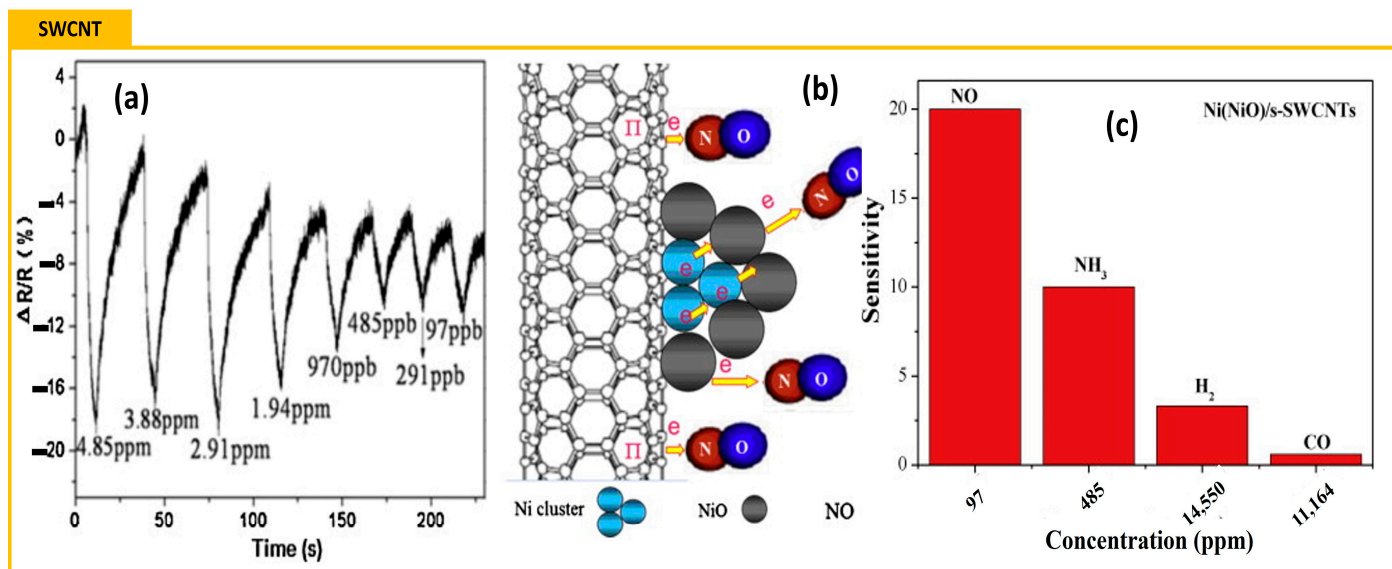


**Figure 54.** (**a**) Dynamic curve at different NO concentrations, (**b**) gas sensing mechanism in carbon nanotubes–NiO composite after exposure to NO gas and (**c**) its selectivity to different gases, reproduced from references [255] Elsevier publisher (Copyright 2013).

Like graphene, carbon nitride is composed of carbon and nitrogen atoms arranged in a two-dimensional honeycomb lattice structure and used for functionalizing NiO sensors and enhancing its gas responsiveness since it showed ultrahigh sensing performance mostly toward $NO_2$ [260]. Li et al. prepared the graphitic carbon nitride (g–$C_3N_4$) nanosheets decorated with a three-dimensional hierarchical flower-like NiO composite (NiO/g–$C_3N_4$). It was observed that the composite with 10 wt% g–$C_3N_4$ exhibited a sensing response to

500 ppm of TEA three-fold higher than pristine NiO at 280 °C. Additionally, the composite showed good selectivity towards TEA among ethanol, methanol, acetone, formaldehyde, and methylbenzene. The improved gas sensitivity can be referred to as the internal charge transfer within the p–n heterojunction and the high specific surface area of the $Ni/C_3N_4$ composite, which promotes adequate contact and chemical reaction between the sensing material surface and gas species [261]. In Table 6, we show the gas sensing response of NiO-carbon material composites.

**Table 6.** Gas sensing response of NiO combined with carbonaceous materials.

| Structure | Carbon Compound | Gas Species | Temperature (°C) | Response |
|---|---|---|---|---|
| NiO nanoparticles [250] | Carbon soot | Mesitylene (43.9 ppm) | RT | NA |
| NiO granular structure [253] | rGO | Methane (1000 ppm) | 260 | 0.15 |
| NiO nanoparticles [262] | rGO | $NH_3$ (100 ppm) | RT | 4.14 |
| NiO nanosheets [252] | rGO | $NO_2$ (15 ppm) | N/A | <7 |
| NiO hierarchical cubes [263] | N-doped rGO | $H_2S$ (50 ppm) | 92 | 31.95 |
| Hexagonal NiO nanosheets [142] | rGO | $NO_2$ (60 ppm) | RT | >7 |
| Flower-like NiO microspheres [251] | rGO | $NO_2$ (100 ppm) | 100 | NA |
| NiO rod-shaped particles [264] | Graphene | $H_2$ (2000 ppm) | 200 | 0.524 |
| NiO nanoparticles [265] | Graphene oxide | Ethanol (500 ppm) | RT | >0.2 |
| NiO nanoparticles [255] | SWCNT | NO (97 ppb) | 18 | 0.05 |
| Aggregated flake-like NiO [256] | MWCNT | Ethanol (500 ppm) | 180 | 3 |
| NiO particles [266] | Carbon nanotubes | $H_2$ (5 sccm) | RT | <0.03 |
| Flower-like NiO [261] | Carbon nitride | TEA (500 ppm) | 280 | 20.03 |

### 3.3.3. Conducting Polymers

Conducting polymers have emerged as promising materials for gas sensor functionalization thanks to their tunable conductivity: they can be a semiconductor, a conductor, a superconductor, or even a magnetic material. Its unique properties due to the delocalized π–electrons on its backbone make it a satisfactory solution to enhance the gas sensing of metal oxide semiconductors (MOX). As most MOX-based gas sensors operate at elevated temperatures, structural modifications can occur, causing instability problems and response/recovery variations next to the possible auto-ignition of combustible gases. Polymers can offer a reliable solution to bypass these issues by ensuring safer detection of gases under mixture conditions and ambient temperature. Generally, the most known polymers used for functionalization of MOX gas sensors are poly(3–hexylthiophene-2,5-diyl) (P3HT), polythiophene (PTh), polypyrrole (PPy), poly(3,4-ethylenedioxythiophene) (PEDOT), and polyaniline (PANI) [267,268]. Regarding NiO, the conducting polymers' effects on gas sensing have rarely been studied.

Hu et al. [269] have investigated PANI and PANI–NiO compounds and proved that hollow NiO/PANI composite possesses higher responsiveness to ammonia at room temperature. However, the highest value can be attained with a hollow morphology of NiO around 43.1%, presenting a larger surface area, unlike the PANI–NiO with a spherical form, which demonstrated 28.7%. The outstanding sensitivity upon ammonia with fast times of response and recovery (149 s and 257 s, respectively) finds its origin in two key factors:

- The hollow structure on which aniline can be polymerized provides a larger specific surface area, facilitating increased adsorption of target gas molecules;
- The p–p heterojunction resulted from the difference in work functions between the two materials inducing holes' transfer from PANI to NiO, leading to the formation of a hole depletion layer (HDL) on the PANI side and a hole accumulation layer (HAL) on the NiO side. This configuration results in higher initial resistance and enhances the sensitivity of the gas-sensing behavior of the h–NiO–PANI composite.

Similar results are also found in the research work [270], showing that the NiO–PANI composite sensitivity varies increasingly in humidity.

In the report [271], NiO–Polyindole/Phenothiazine (NiO–PIN/PTZ) nanocomposites have been investigated for gas sensing applications at different loading percentages, demonstrating the highest sensitivity upon ammonia at 10 wt% at room temperature. It is evident that the sensing ability of the composite diminishes with higher loading of filler particles, particularly at 15 wt%. This decrease in sensitivity is primarily attributed to the agglomeration of nanoparticles within the polymer matrix [272]. Consequently, it can be concluded that NiO nanoparticles have the potential to enhance the gas-sensing properties of the polymer matrix, provided that appropriate loading and dispersion techniques are employed to minimize agglomeration and ensure a favorable nanoparticle–polymer interaction.

All the research papers reported in this section show an operation at room temperature, which represents a challenging issue for environmental monitoring applications.

In Table 7, we summarize the gas sensing response of different NiO–polymer composites.

**Table 7.** Gas responsiveness of NiO–polymer composite-based sensors.

| Structure | Conducting Polymer | Gas Species | Temperature | Response |
|---|---|---|---|---|
| NiO hollow spheres [269] | PANI | $NH_3$ (10 ppm) | RT | 0.431 |
| NiO spheres [269] | PANI | $NH_3$ (10 ppm) | RT | 0.287 |
| NiO nanoparticles [271] | PIN/PTZ blend | $NH_3$ (100 ppm) | RT | >0.9 |
| Ag–NiO nanoparticles [272] | PPy | $NH_3$ (100 ppm) | RT | <0.5 |
| Mesoporous NiO nanosheets [273] | PPy | $NO_2$ (60 ppm) | RT | 45 |

## 4. Conclusions and Outlooks

Sensors play a pivotal role in our ability to discern pertinent information from our surroundings and subsequently transform this information into discernible electric signals. Among the various sensor types, gas sensors have garnered significant attention for their extensive applications in industrial and domestic environments. Metal oxide gas sensors offer a multitude of advantages, including low power consumption, compact dimensions, cost-effectiveness, and a high degree of reliability. Their capacity to detect and quantify specific gases within a given environment has proven invaluable in numerous contexts, contributing to enhanced safety, environmental monitoring, and the optimization of various industrial processes. This review has placed a particular emphasis on nickel oxide due to its properties as well as its efficiency in gas detection by reporting recent advances in its sensitivity towards various gases, particularly ethanol, acetone, formaldehyde, benzene, and toluene which were cited as the top five gases detected by NiO within the last three years.

A specific focus on the different growth approaches used for preparing NiO structures, including vapor-phase deposition, liquid-phase deposition, and solution processing, has been discussed, and the key parameters of each technique impacting the morphology and physical properties of nickel oxide have been discussed. The hierarchical morphology and nanostructures with high specific surface area showed higher gas responses than other structures due to the increased adsorption sites that enhance the chemisorption of oxygen species and adsorption of target gas molecules in different environments.

Despite the correspondence of p-type MOX gas response to the square root of that exhibited by n-type MOX with identical morphologies, NiO showed good gas response in dry and humid conditions, which makes it a moisture-tolerant sensor used in real-time monitoring applications.

As a p-type material, NiO, often integrated into novel nanostructures and p–n heterojunctions, offers benefits such as wide band gaps, low current operation, increased durability, and resilience to humidity. The combination of NiO with n-type or p-type metal oxides in heterojunctions enhances adsorption sites, leading to superior sensing performance when compared to pristine material. Moreover, the catalytic activity of NiO fortifies the

synergistic effects within hybrid structures by amplifying oxygen chemisorption, thereby the reduction or oxidation of various volatile organic compounds. Functionalization of NiO by noble metals can also enhance its gas sensing capabilities by increasing adsorption sites, improving catalytic activity, boosting charge transfer between NiO and target gas species, and reducing operating temperature. Carbon-based materials play an important role in reducing the working temperature of NiO, optimizing its gas response towards several gases, and shortening the response/recovery time due to high carrier density and mobility at room temperature and low resistivity that offer efficient electron transfer, added to porosity that provides more specific surface area for gas adsorption. Polymers are commonly used for the same purpose, providing an operation at room temperature of NiO combined with PANI, PPy, and PIN/PTZ blend. Notably, the agglomeration phenomenon should be avoided when combining polymers with MOXs to keep a higher specific surface area by tuning the MOX loading and controlling the interactions between MOX particles and polymer chains.

More accurate and reliable gas detection can be admitted for NiO sensors by further optimizing the growth conditions, tuning the surface morphology, and combining it with other compounds to highly reduce the working temperature. Real-time is also a challenge for such material to make more advanced gas sensing systems that can address emerging challenges in environmental and industrial monitoring. The development of uniform gas sensor arrays and the application of deep learning algorithms to analyze the data from these arrays hold promise for resolving these challenges. By overcoming these obstacles, improved selectivity, enhanced accuracy, and real-time monitoring can be achieved, enabling more effective and reliable gas sensing capabilities in NiO-based devices.

**Conflicts of Interest:** The authors declare no conflicts of interest.

# References

1. Wei, H.; Zhang, H.; Song, B.; Yuan, K.; Xiao, H.; Cao, Y.; Cao, Q. Metal–Organic Framework (MOF) Derivatives as Promising Chemiresistive Gas Sensing Materials: A Review. *Int. J. Environ. Res. Public Health* **2023**, *20*, 4388. [CrossRef] [PubMed]
2. Eranna, G.; Joshi, B.C.; Runthala, D.P.; Gupta, R.P. Oxide Materials for Development of Integrated Gas Sensors—A Comprehensive Review. *Crit. Rev. Solid State Mater. Sci.* **2004**, *29*, 111–188. [CrossRef]
3. Dey, A. Semiconductor metal oxide gas sensors: A review. *Mater. Sci. Eng. B* **2018**, *229*, 206–217. [CrossRef]
4. Wang, C.; Yin, L.; Zhang, L.; Xiang, D.; Gao, R. Metal Oxide Gas Sensors: Sensitivity and Influencing Factors. *Sensors* **2010**, *10*, 2088–2106. [CrossRef] [PubMed]
5. Zhong, M.; Hisatomi, T.; Kuang, Y.; Zhao, J.; Liu, M.; Iwasi, A.; Jia, Q.; Nishiyama, H.; Minegishi, T.; Nakabayashi, M.; et al. Surface Modification of $CoO_x$ Loaded $BiVO_4$ Photoanodes with Ultrathin *p*-Type NiO Layers for Improved Solar Water Oxidation. *J. Am. Chem. Soc.* **2015**, *137*, 5053–5060. [CrossRef] [PubMed]
6. Neiva, E.G.; Oliveira, M.M.; Marcolino, L.H.; Zarbin, A.J. Nickel nanoparticles with hcp structure: Preparation, deposition as thin films and application as electrochemical sensor. *J. Colloid Interface Sci.* **2016**, *468*, 34–41. [CrossRef] [PubMed]
7. Miura, N.; Wang, J.; Nakatou, M.; Elumalai, P.; Zhuiykov, S.; Hasei, M. High-temperature operating characteristics of mixed-potential-type $NO_2$ sensor based on stabilized-zirconia tube and NiO sensing electrode. *Sens. Actuators B Chem.* **2006**, *114*, 903–909. [CrossRef]

8.　Diao, C.-C.; Huang, C.-Y.; Yang, C.-F.; Wu, C.-C. Morphological, Optical, and Electrical Properties of p-Type Nickel Oxide Thin Films by Nonvacuum Deposition. *Nanomaterials* **2020**, *10*, 636. [CrossRef]

9.　Aslinjensipriya, A.; Sylvia Reena, R.; Ragu, P.; Grace Infantiya, S.; Mangalam, G.; Justin Raj, C.; Jerome Das, S. Exploring the influence of tin in micro-structural, magneto-optical and antimicrobial traits of nickel oxide nanoparticles. *Surf. Interfaces* **2021**, *28*, 101605. [CrossRef]

10.　Chen, W.; Wu, Y.; Yue, Y.; Liu, J.; Zhang, W.; Yang, X.; Chen, H.; Bi, E.; Ashraful, I.; Grätzel, M.; et al. Efficient and stable large-area perovskite solar cells with inorganic charge extraction layers. *Science* **2015**, *350*, 944–948. [CrossRef]

11.　Jang, W.-L.; Lu, Y.-M.; Hwang, W.-S.; Hsiung, T.-L.; Wang, H.P. Point defects in sputtered NiO films. *Appl. Phys. Lett.* **2009**, *94*, 062103. [CrossRef]

12.　Kumar, N.; Lee, H.B.; Hwang, S.; Kang, J.-W. Large-area, green solvent spray deposited nickel oxide films for scalable fabrication of triple-cation perovskite solar cells. *J. Mater. Chem. A* **2020**, *8*, 3357–3368. [CrossRef]

13.　Wilson, R.L.; Simion, C.E.; Stanoiu, A.; Taylor, A.; Guldin, S.; Covington, J.A.; Carmalt, C.J.; Blackman, C.S. Humidity-Tolerant Ultrathin NiO Gas-Sensing Films. *ACS Sens.* **2020**, *5*, 1389–1397. [CrossRef] [PubMed]

14.　Simion, C.; Junker, B.; Weimar, U.; Stanoiu, A.; Bârsan, N. Sensing mechanisms of CO and $H_2$ with NiO material–DRIFTS investigations. *Sens. Actuators B Chem.* **2023**, *390*, 134028. [CrossRef]

15.　Simion, C.E.; Ghica, C.; Mihalcea, C.G.; Ghica, D.; Mercioniu, I.; Somacescu, S.; Florea, O.G.; Stanoiu, A. Insights about CO Gas-Sensing Mechanism with NiO-Based Gas Sensors—The Influence of Humidity. *Chemosensors* **2021**, *9*, 244. Available online: https://www.mdpi.com/2227-9040/9/9/244 (accessed on 3 February 2024). [CrossRef]

16.　Liu, Y.S.; Gao, C.; Li, Q.; Pang, H. Nickel Oxide/Graphene Composites: Synthesis and Applications. *Chemistry* **2019**, *25*, 2141–2160. [CrossRef] [PubMed]

17.　Mokoena, T.P.; Swart, H.C.; Motaung, D.E. A review on recent progress of p-type nickel oxide based gas sensors: Future perspectives. *J. Alloys Compd.* **2019**, *805*, 267–294. [CrossRef]

18.　Li, Q.; Zeng, W.; Li, Y. NiO-Based Gas Sensors for Ethanol Detection: Recent Progress. *J. Sens.* **2022**, *2022*, 1855493. [CrossRef]

19.　Prajesh, R.; Goyal, V.; Nahid, M.; Saini, V.; Singh, A.K.; Sharma, A.K.; Bhargava, J.; Agarwal, A. Nickel oxide (NiO) thin film optimization by reactive sputtering for highly sensitive formaldehyde sensing. *Sens. Actuators B Chem.* **2020**, *318*, 128166. [CrossRef]

20.　Hotovy, I.; Spiess, L.; Predanocy, M.; Rehacek, V.; Racko, J. Sputtered nanocrystalline NiO thin films for very low ethanol detection. *Vacuum* **2014**, *107*, 129–131. [CrossRef]

21.　Urs, K.M.B.; Sahoo, K.; Bhat, N.; Kamble, V. Complementary Metal Oxide Semiconductor-Compatible Top-Down Fabrication of a Ni/NiO Nanobeam Room Temperature Hydrogen Sensor Device. *ACS Appl. Electron. Mater.* **2022**, *4*, 87–91. [CrossRef]

22.　Wang, R.; Lin, H.; Zhu, H.; Wan, M.; Shen, K.; Mai, Y. Preparation, investigation and application of nickel oxide thin films in flexible all-thin-film electrochromic devices: From material to device. *J. Alloys Compd.* **2021**, *898*, 162879. [CrossRef]

23.　Terlemezoglu, M.; Surucu, O.; Isik, M.; Gasanly, N.M.; Parlak, M. Temperature-dependent optical characteristics of sputtered NiO thin films. *Appl. Phys. A* **2021**, *128*, 50. [CrossRef]

24.　Pooyodying, P.; Son, Y.-H.; Sung, Y.-M.; Ok, J.-W. The effect of sputtering Ar gas pressure on optical and electrical properties of flexible ECD device with $WO_3$ electrode deposited by RF magnetron sputtering on ITO/PET substrate. *Opt. Mater.* **2021**, *123*, 111829. [CrossRef]

25.　Elmassi, S.; Narjis, A.; Nkhaili, L.; Elkissani, A.; Amiri, L.; Drissi, S.; Abali, A.; Bousseta, M.; Outzouhit, A. Effect of annealing on structural, optical and electrical properties of nickel oxide thin films synthesized by the reactive radio frequency sputtering. *Phys. B Condens. Matter.* **2022**, *639*, 413980. [CrossRef]

26.　Peng, Z.; Zuo, Z.; Qi, Q.; Hou, S.; Fu, Y.; Zou, D. Managing the Double-Edged Sword of Ni3+ in Sputter-Deposited NiO x by Interfacial Redox Reactions for Efficient Perovskite Solar Cells. *ACS Appl. Energy Mater.* **2023**, *6*, 1396–1403. [CrossRef]

27.　Li, H.; Li, Y.; Li, X.; Xie, A.; Sun, D.; Wang, Y. Effects of Sputtering Pressure on Electrochromic Properties of NiO films Prepared by DC Magnetron Sputtering. *J. Electrochem. Soc.* **2022**, *169*, 116508. [CrossRef]

28.　Astinchap, B.; Awrang, S.M.; Norian, E. Surface characterization of NiO thin films deposited by RF-magnetron sputtering at different thickness: Statistical and multifractal approach. *Microsc. Res. Tech.* **2022**, *85*, 3056–3068. [CrossRef]

29.　Poulain, R.; Rohrer, J.; Hermans, Y.; Dietz, C.; Brötz, J.; Proost, J.; Chatenet, M.; Klein, A. Origin of Surface Reduction upon Water Adsorption on Oriented NiO Thin Films and Its Relation to Electrochemical Activity. *J. Phys. Chem. C* **2022**, *126*, 1303–1315. [CrossRef]

30.　Gao, X.; Meng, X. Effect of reactive pressure on direct current-sputtered NiO films with improved p-type conduction ability. *Phys. B Condens. Matter.* **2023**, *650*, 414540. [CrossRef]

31.　Mohr, J.; Hennen, T.; Bedau, D.; Nag, J.; Waser, R.; Wouters, D.J. Fabrication of highly resistive NiO thin films for nanoelectronic applications. *Adv. Phys. Res.* **2022**, *1*, 2200008. [CrossRef]

32.　Hameed, A.M.; Hameed, M.A. Spectroscopic characteristics of highly pure metal oxide nanostructures prepared by DC reactive magnetron sputtering technique. *Emergent Mater.* **2022**, *6*, 627–633. [CrossRef]

33.　Turgut, E.; Çoban, Ö.; Sarıtaş, S.; Tüzemen, S.; Yıldırım, M.; Gür, E. Oxygen partial pressure effects on the RF sputtered p-type NiO hydrogen gas sensors. *Appl. Surf. Sci.* **2018**, *435*, 880–885. [CrossRef]

34. Jamal, M.S.; Shahahmadi, S.A.; Chelvanathan, P.; Alharbi, H.F.; Karim, M.R.; Dar, M.A.; Luqman, M.; Alharthi, N.H.; Al-Harthi, Y.S.; Aminuzzaman, M.; et al. Effects of growth temperature on the photovoltaic properties of RF sputtered undoped NiO thin films. *Results Phys.* **2019**, *14*, 102360. [CrossRef]

35. Wang, Y.; Ghanbaja, J.; Boulet, P.; Horwat, D.; Pierson, J. Growth, interfacial microstructure and optical properties of NiO thin films with various types of texture. *Acta Mater.* **2018**, *164*, 648–653. [CrossRef]

36. Comini, E.; Bianchi, S.; Faglia, G.; Ferroni, M.; Vomiero, A.; Sberveglieri, G. Functional nanowires of tin oxide. *Appl. Phys. A* **2007**, *89*, 73–76. [CrossRef]

37. Zhu, Z.; Chen, T.-L.; Gu, Y.; Warren, J.; Osgood, R.M. Zinc Oxide Nanowires Grown by Vapor-Phase Transport Using Selected Metal Catalysts: A Comparative Study. *Chem. Mater.* **2005**, *17*, 4227–4234. [CrossRef]

38. Kim, T.; Kim, J.; Kumar, M.S.; Suh, E.-K.; Nahm, K. Influence of ambient gases on the morphology and photoluminescence of ZnO nanostructures synthesized with nickel oxide catalyst. *J. Cryst. Growth* **2004**, *270*, 491–497. [CrossRef]

39. García-Alonso, J.; Maestre, D.; Bartolomé, J.; García-Tecedor, M.; Vásquez-López, A.; Taeño, M.; del Prado, F.; Nogales, E.; Cremades, A. Synthesis of low dimensional oxide based complex materials by a vapor-solid method. In *Oxide-Based Materials and Devices XII*; SPIE: Cambridge, MA, USA, 2021; Volume 11687, pp. 125–134. [CrossRef]

40. Singh, Y.R.; Kataria, S.; Barshilia, H.C. Different Morphologies of Zinc Oxide Nanostructures Grown Under Similar Deposition Conditions During Vapor–Liquid–Solid Growth. *Nanosci. Nanotechnol. Lett.* **2013**, *5*, 1224–1230. [CrossRef]

41. Kaur, N.; Singh, M.; Comini, E. One-Dimensional Nanostructured Oxide Chemoresistive Sensors. *Langmuir* **2020**, *36*, 6326–6344. [CrossRef]

42. Kaur, N.; Comini, E.; Zappa, D.; Poli, N.; Sberveglieri, G. Nickel oxide nanowires: Vapor liquid solid synthesis and integration into a gas sensing device. *Nanotechnology* **2016**, *27*, 205701. [CrossRef] [PubMed]

43. Strawbridge, A.; Rapp, R.A. The Role of Reactive Elements on Scale Growth in High-Temperature Oxidation of Pure Nickel, Iron, Cobalt, and Copper: I. Oxidation Kinetics and Scale Morphology. *J. Electrochem. Soc.* **1994**, *141*, 1905. [CrossRef]

44. Hiralal, P.; Unalan, H.E.; Wijayantha, K.G.U.; Kursumovic, A.; Jefferson, D.; MacManus-Driscoll, J.L.; Amaratunga, G.A.J. Growth and process conditions of aligned and patternable films of iron (III) oxide nanowires by thermal oxidation of iron. *Nanotechnology* **2008**, *19*, 455608. [CrossRef] [PubMed]

45. Zappa, D.; Comini, E.; Zamani, R.; Arbiol, J.; Morante, J.; Sberveglieri, G. Copper oxide nanowires prepared by thermal oxidation for chemical sensing. *Procedia Eng.* **2011**, *25*, 753–756. [CrossRef]

46. Zappa, D.; Comini, E.; Sberveglieri, G. Thermally oxidized zinc oxide nanowires for use as chemical sensors. *Nanotechnology* **2013**, *24*, 444008. [CrossRef] [PubMed]

47. Liu, Y.Y.; Natesan, K. The Adherence of Nickel Oxide on Nickel during High-Temperature Oxidation. *MRS Proc.* **1988**, *119*, 213. [CrossRef]

48. Pinnel, M.; Tompkins, H.; Heath, D. Oxidation of Nickel and Nickel-Gold Alloys in Air at 50°–150° C. *J. Electrochem. Soc.* **1979**, *126*, 1274. [CrossRef]

49. Dastan, D.; Shan, K.; Jafari, A.; Marszalek, T.; Mohammed, M.K.A.; Tao, L.; Shi, Z.; Chen, Y.; Yin, X.T.; Alharbi, N.D.; et al. Influence of heat treatment on H$_2$S gas sensing features of NiO thin films deposited via thermal evaporation technique. *Mater. Sci. Semicond. Process.* **2023**, *154*, 107232. [CrossRef]

50. De Los Santos Valladares, L.; Ionescu, A.; Holmes, S.; Barnes, C.H.W.; Dominguez, A.B.; Quispe, O.A.; González, J.C.; Milana, S.; Barbone, M.; Ferrari, A.C.; et al. Characterization of Ni thin films following thermal oxidation in air. *J. Vac. Sci. Technol. B* **2014**, *32*, 051808. [CrossRef]

51. Hajakbari, F. Characterization of nanocrystalline nickel oxide thin films prepared at different thermal oxidation temperatures. *J. Nanostruct. Chem.* **2020**, *10*, 97–103. [CrossRef]

52. Peraldi, R.; Monceau, D.; Jean, S.; Pieraggi, B. High temperature oxidation of high purity nickel: Oxide scale morphology and growth kinetics. *Mater. High Temp.* **2003**, *20*, 649–655. [CrossRef]

53. Mrowec, S.; Grzesik, Z. Oxidation of nickel and transport properties of nickel oxide. *J. Phys. Chem. Solids* **2004**, *65*, 1651–1657. [CrossRef]

54. Marciuš, M.; Ristić, M.; Ivanda, M.; Musić, S. Formation and microstructure of nickel oxide films. *J. Alloys Compd.* **2012**, *541*, 238–243. [CrossRef]

55. Ren, Y.; Chim, W.K.; Chiam, S.Y.; Huang, J.Q.; Pi, C.; Pan, J.S. Formation of Nickel Oxide Nanotubes with Uniform Wall Thickness by Low-Temperature Thermal Oxidation through Understanding the Limiting Effect of Vacancy Diffusion and the Kirkendall Phenomenon. *Adv. Funct. Mater.* **2010**, *20*, 3336–3342. [CrossRef]

56. Vorotyntsev, A.V.; Markov, A.N.; Kapinos, A.A.; Petukhov, A.N.; Atlaskin, A.A.; Golovacheva, A.A.; Vilkov, I.V.; Yunin, P.A.; Vorotyntsev, V.M.; Vorotyntsev, I.V. Direct synthesis of nanostructural and nanospherical silica using induction jet levitation: Synthesis, design and catalytic application. *Mater. Today Chem.* **2022**, *26*, 101004. [CrossRef]

57. Morozov, Y.G.; Belousova, O.V.; Kuznetsov, M.V.; Ortega, D.; Parkin, I.P. Electric field-assisted levitation-jet aerosol synthesis of Ni/NiO nanoparticles. *J. Mater. Chem.* **2012**, *22*, 11214–11223. [CrossRef]

58. Hernández, P.T.; Kuznetsov, M.V.; Morozov, I.G.; Parkin, I.P. Application of levitation-jet synthesized nickel-based nanoparticles for gas sensing. *Mater. Sci. Eng. B* **2019**, *244*, 81–92. [CrossRef]

59. Baiutti, F.; Wrobel, F.; Christiani, G.; Logvenov, G. Oxide molecular beam epitaxy of complex oxide heterointerfaces. In *Metal Oxide-Based Thin Film Structures*; Elsevier: Amsterdam, The Netherlands, 2018; pp. 53–78.

60. Budde, M.; Remmele, T.; Tschammer, C.; Feldl, J.; Franz, P.; Lähnemann, J.; Cheng, Z.; Hanke, M.; Ramsteiner, M.; Albrecht, M.; et al. Plasma-assisted molecular beam epitaxy of NiO on GaN(00.1). *J. Appl. Phys.* **2020**, *127*, 015306. [CrossRef]

61. Zhang, Z.; Lukaszew, R.A.; Cionca, C.; Pan, X.; Clarke, R.; Yeadon, M.; Zambano, A.; Walko, D.; Dufresne, E.; te Velthius, S. Correlated structural and magnetization reversal studies on epitaxial Ni films grown with molecular beam epitaxy and with sputtering. *J. Vac. Sci. Technol. A* **2004**, *22*, 1868–1872. [CrossRef]

62. Chaudhary, K.T. Thin film deposition: Solution based approach. In *Thin Films*; IntechOpen: Budhapest, Hungary, 2021.

63. Herman, M.A.; Sitter, H. *Molecular Beam Epitaxy: Fundamentals and Current Status*; Springer Science & Business Media: Berlin/Heidelberg, Germany, 2012.

64. Lane, P.A.; Wright, P.J.; Crosbie, M.J.; Pitt, A.D.; Reeves, C.L.; Cockayne, B.; Jones, A.C.; Leedham, T.J. Liquid injection metal organic chemical vapour deposition of nickel zinc ferrite thin films. *J. Cryst. Growth* **1998**, *192*, 423–429. [CrossRef]

65. Liu, X.; Chan, S.H.; Wu, F.; Li, Y.; Keller, S.; Speck, J.S.; Mishra, U.K. Metalorganic chemical vapor deposition of $Al_2O_3$ using trimethylaluminum and $O_2$ precursors: Growth mechanism and crystallinity. *J. Cryst. Growth* **2014**, *408*, 78–84. [CrossRef]

66. Seisenbaeva, G.A.; Kessler, V.G. Precursor directed synthesis–"molecular" mechanisms in the Soft Chemistry approaches and their use for template-free synthesis of metal, metal oxide and metal chalcogenide nanoparticles and nanostructures. *Nanoscale* **2014**, *6*, 6229–6244. [CrossRef] [PubMed]

67. Kukimoto, H. MOCVD—Current state and future. *J. Cryst. Growth* **1989**, *95*, 360–362. [CrossRef]

68. Wright, P.J.; Crosbie, M.J.; Williams, D.J.; Lane, P.A.; Jones, A.C.; Leedham, T.J.; Davies, H.O. Metal organic chemical vapor deposition (MOCVD) of oxides and ferroelectric materials. *J. Mater. Sci. Mater. Electron.* **2002**, *13*, 671–678. [CrossRef]

69. Nigro, R.L.; Battiato, S.; Greco, G.; Fiorenza, P.; Roccaforte, F.; Malandrino, G. Metal Organic Chemical Vapor Deposition of nickel oxide thin films for wide band gap device technology. *Thin Solid Films* **2014**, *563*, 50–55. [CrossRef]

70. George, S.M. Atomic Layer Deposition: An Overview. *Chem. Rev.* **2009**, *110*, 111–131. [CrossRef] [PubMed]

71. Santinacci, L. Atomic layer deposition: An efficient tool for corrosion protection. *Curr. Opin. Colloid Interface Sci.* **2023**, *63*, 101674. [CrossRef]

72. Pan, H.; Wang, C.; Zhang, Z.; Li, Y.; Hou, X.; Zheng, W.; Liu, X.; Wan, Y.; Zhang, J. Oxygen vacancy-enriched ALD NiO sub-50 nm thin films for enhanced triethylamine detection. *Appl. Phys. Lett.* **2022**, *121*, 111603. [CrossRef]

73. Hile, D.; Swart, H.; Motloung, S.; Kroon, R.; Egbo, K.; Koao, L. The effect of annealing time on zinc selenide thin films deposited by photo-assisted chemical bath deposition. *J. Phys. Chem. Solids* **2020**, *140*, 109381. [CrossRef]

74. He, H. Thermal-assisted chemical bath deposition and optical property of CuS films. *Optoelectron. Adv. Mater.-Rapid Commun.* **2011**, *5*, 1301–1306.

75. Lin, W.-W.; Wang, N.-W.; Lan, Z.-Y.; Huang, Z.-P.; Lin, L.-M.; Ye, Q.-Y.; Chen, S.-Y.; Chen, G.-L. A facile Ion-Exchange assisted chemical bath deposition of $CuSbS_2$ for thin film solar cells. *Sol. Energy* **2022**, *244*, 465–473. [CrossRef]

76. Han, S.-Y.; Lee, D.-H.; Chang, Y.-J.; Ryu, S.-O.; Lee, T.-J.; Chang, C.-H. The Growth Mechanism of Nickel Oxide Thin Films by Room-Temperature Chemical Bath Deposition. *J. Electrochem. Soc.* **2006**, *153*, C382. [CrossRef]

77. Hao, F.; Verma, A.; Mukherjee, P.P. Electrodeposition stability of metal electrodes. *Energy Storage Mater.* **2019**, *20*, 1–6. [CrossRef]

78. Maile, N.; Shinde, S.; Koli, R.; Fulari, A.; Kim, D.; Fulari, V. Effect of different electrolytes and deposition time on the supercapacitor properties of nanoflake-like $Co(OH)_2$ electrodes. *Ultrason. Sonochem.* **2018**, *51*, 49–57. [CrossRef] [PubMed]

79. Firat, Y. Influence of current density on Al:NiO thin films via electrochemical deposition: Semiconducting and electrochromic properties. *Mater. Sci. Semicond. Process.* **2020**, *109*, 104958. [CrossRef]

80. Park, B.-O.; Lokhande, C.; Park, H.-S.; Jung, K.-D.; Joo, O.-S. Performance of supercapacitor with electrodeposited ruthenium oxide film electrodes—Effect of film thickness. *J. Power Sources* **2004**, *134*, 148–152. [CrossRef]

81. Zhang, Y.; Xie, L.-Z.; Yuan, C.-X.; Zhang, C.-L.; Liu, S.; Peng, Y.-Q.; Li, H.-R.; Zhang, M. Preparation of 3D rose-like nickel oxide nanoparticles by electrodeposition method and application in gas sensors. *J. Mater. Sci. Mater. Electron.* **2015**, *27*, 1817–1827. [CrossRef]

82. Shahzad, A.; Khan, I.A.; Manzoor, A.; Kashif, M.; Ahsan, M.; He, M.; Razzokov, J. Synthesis of nickel nanowires (Ni-NWs) as high ferromagnetic material by electrodeposition technique. *Heliyon* **2022**, *9*, e12576. [CrossRef]

83. Xue, J.; Wu, T.; Dai, Y.; Xia, Y. Electrospinning and Electrospun Nanofibers: Methods, Materials, and Applications. *Chem. Rev.* **2019**, *119*, 5298–5415. [CrossRef]

84. Katsogiannis, K.A.G.; Vladisavljević, G.T.; Georgiadou, S.; Rahmani, R. Assessing the Increase in Specific Surface Area for Electrospun Fibrous Network due to Pore Induction. *ACS Appl. Mater. Interfaces* **2016**, *8*, 29148–29154. [CrossRef]

85. Ercolano, G.; Farina, F.; Cavaliere, S.; Jones, D.J.; Rozière, J. Nickel Based Electrospun Materials with Tuned Morphology and Composition. *Nanomaterials* **2016**, *6*, 236. [CrossRef]

86. Balogun, M.-S.; Zeng, Y.; Qiu, W.; Luo, Y.; Onasanya, A.; Olaniyi, T.K.; Tong, Y. Three-dimensional nickel nitride ($Ni_3N$) nanosheets: Free standing and flexible electrodes for lithium ion batteries and supercapacitors. *J. Mater. Chem. A* **2016**, *4*, 9844–9849. [CrossRef]

87. Liu, H.; Wang, X.; He, G.; Lin, Y.; Wei, J.; Zheng, J.; Zheng, G.; Sun, D. Electrospun nickel oxide nanofibers for gas sensor application. In Proceedings of the 8th Annual IEEE International Conference on Nano/Micro Engineered and Molecular Systems, Suzhou, China, 7–10 April 2013; pp. 377–380.

88. Yu, G.; Li, T.S.; Xu, M.; Andersson, M.; Li, B.; Tang, H.; Parbey, J.; Shao, J. Fabrication of nickel-YSZ cermet nanofibers via electrospinning. *J. Alloys Compd.* **2017**, *693*, 1214–1219. [CrossRef]

89.  Haider, A.J.; Al-Anbari, R.; Sami, H.M.; Haider, M.J. Photocatalytic activity of nickel oxide. *J. Mater. Res. Technol.* **2019**, *8*, 2802–2808. [CrossRef]

90.  Chtouki, T.; Soumahoro, L.; Kulyk, B.; Bougharraf, H.; Kabouchi, B.; Erguig, H.; Sahraoui, B. Comparison of structural, morphological, linear and nonlinear optical properties of NiO thin films elaborated by Spin-Coating and Spray Pyrolysis. *Optik* **2017**, *128*, 8–13. [CrossRef]

91.  Kim, S.-K.; Seok, H.-J.; Kim, D.-H.; Choi, D.-H.; Nam, S.-J.; Kim, S.-C.; Kim, H.-K. Comparison of NiO x thin film deposited by spin-coating or thermal evaporation for application as a hole transport layer of perovskite solar cells. *RSC Adv.* **2020**, *10*, 43847–43852. [CrossRef] [PubMed]

92.  Chtouki, T.; El Mrabet, M.; Tarbi, A.; Goncharova, I.; Erguig, H. Comprehensive review of the morphological, linear and nonlinear optical characterization of spin-coated NiO thin films for optoelectronic applications. *Opt. Mater.* **2021**, *118*, 111294. [CrossRef]

93.  Tang, X.; Yan, X. Dip-coating for fibrous materials: Mechanism, methods and applications. *J. Sol-Gel Sci. Technol.* **2016**, *81*, 378–404. [CrossRef]

94.  Kalangestani, F.C.; Simiari, M.; Ghodsi, F.E. Preparation and characterization of vanadium-doped nickel oxide nanostructure deposited by dip-coating technique. *Eur. Phys. J. Plus* **2021**, *136*, 517. [CrossRef]

95.  Reale, A.; LA Notte, L.; Salamandra, L.; Polino, G.; Susanna, G.; Brown, T.M.; Brunetti, F.; Di Carlo, A. Spray Coating for Polymer Solar Cells: An Up-to-Date Overview. *Energy Technol.* **2015**, *3*, 385–406. [CrossRef]

96.  Srikanth, A.; Basha, G.M.T.; Venkateshwarlu, B. A Brief Review on Cold Spray Coating Process. *Mater. Today Proc.* **2020**, *22*, 1390–1397. [CrossRef]

97.  Desai, J.D. Nickel oxide thin films by spray pyrolysis. *J. Mater. Sci. Mater. Electron.* **2016**, *27*, 12329–12334. [CrossRef]

98.  Desai, J.; Min, S.-K.; Jung, K.-D.; Joo, O.-S. Spray pyrolytic synthesis of large area NiOx thin films from aqueous nickel acetate solutions. *Appl. Surf. Sci.* **2006**, *253*, 1781–1786. [CrossRef]

99.  Calvert, P. Inkjet Printing for Materials and Devices. *Chem. Mater.* **2001**, *13*, 3299–3305. [CrossRef]

100.  Huang, C.-C.; Kao, Z.-K.; Liao, Y.-C. Flexible Miniaturized Nickel Oxide Thermistor Arrays via Inkjet Printing Technology. *ACS Appl. Mater. Interfaces* **2013**, *5*, 12954–12959. [CrossRef] [PubMed]

101.  Heinrich, C.A.; Candela, P.A. Fluids and ore formation in the Earth's crust. In *Treatise on Geochemistry*, 2nd ed.; Elsevier: Amsterdam, The Netherlands, 2014; Volume 13, pp. 1–28.

102.  Gan, Y.X.; Jayatissa, A.H.; Yu, Z.; Chen, X.; Li, M. Hydrothermal Synthesis of Nanomaterials. *J. Nanomater.* **2020**, *2020*, 89170. [CrossRef]

103.  Rungchet, A.; Chindaprasirt, P.; Wansom, S.; Pimraksa, K. Hydrothermal synthesis of calcium sulfoaluminate–belite cement from industrial waste materials. *J. Clean. Prod.* **2016**, *115*, 273–283. [CrossRef]

104.  Tavakoli, A.; Sohrabi, M.; Kargari, A. A review of methods for synthesis of nanostructured metals with emphasis on iron compounds. *Chem. Pap.* **2007**, *61*, 151–170. [CrossRef]

105.  Nadimpalli, N.K.V.; Bandyopadhyaya, R.; Runkana, V. Thermodynamic analysis of hydrothermal synthesis of nanoparticles. *Fluid Phase Equilibria* **2018**, *456*, 33–45. [CrossRef]

106.  Wilson, M. The origin and formation of clay minerals in soils: Past, present and future perspectives. *Clay Miner.* **1999**, *34*, 7–25. [CrossRef]

107.  Wang, C.; Huang, W.; Wang, Y.; Cheng, Y.; Zou, B.; Fan, X.; Yang, J.; Cao, X. Synthesis of monodispersed $La_2Ce_2O_7$ nanocrystals via hydrothermal method: A study of crystal growth and sintering behavior. *Int. J. Refract. Met. Hard Mater.* **2012**, *31*, 242–246. [CrossRef]

108.  Soa, W.-W.; Janga, J.-S.; Rheeb, Y.-W.; Kima, K.-J.; Moon, S.-J. Preparation of Nanosized Crystalline CdS Particles by the Hydrothermal Treatment. *J. Colloid Interface Sci.* **2001**, *237*, 136–141. [CrossRef] [PubMed]

109.  Tiwari, A.; Michalska-Domanska, M.; Dhoble, S.J. 10—Nanocomposite-based functional materials: Synthesis, properties, and applications. In *Functional Materials from Carbon, Inorganic, and Organic Sources*; Dhoble, S.J., Nande, A., Kalyani, N.T., Tiwari, A., Arof, A.K., Eds.; Woodhead Publishing: Cambridge, MA, USA, 2023; pp. 317–365.

110.  Erdem, S.; Erdem, B.; Öksüzoğlu, R.M.; Çıtak, A. Effect of calcination temperature on the structural and magnetic properties of Ni/SBA-15 nanocomposite. *J. Porous Mater.* **2015**, *22*, 689–698. [CrossRef]

111.  Mokoena, T.P.; Hillie, K.T.; Swart, H.C.; Leshabane, N.; Tshilongo, J.; Motaung, D.E. Fabrication of a propanol gas sensor using p-type nickel oxide nanostructures: The effect of ramping rate towards luminescence and gas sensing characteristics. *Mater. Chem. Phys.* **2020**, *253*, 123316. [CrossRef]

112.  Parashar, M.; Shukla, V.K.; Singh, R. Metal oxides nanoparticles via sol–gel method: A review on synthesis, characterization and applications. *J. Mater. Sci. Mater. Electron.* **2020**, *31*, 3729–3749. [CrossRef]

113.  Milea, C.; Bogatu, C.; Duta, A. The influence of parameters in silica sol-gel process. *Bull. Transilv. Univ. Bras.* **2011**, *4*, 53.

114.  Guastaferro, M.; Reverchon, E.; Baldino, L. Polysaccharide-based aerogel production for biomedical applications: A comparative review. *Materials* **2021**, *14*, 1631. [CrossRef]

115.  Niederberger, M. Nonaqueous Sol–Gel Routes to Metal Oxide Nanoparticles. *Acc. Chem. Res.* **2007**, *40*, 793–800. [CrossRef]

116.  Kakihana, M. Invited review "sol-gel" preparation of high temperature superconducting oxides. *J. Sol-Gel Sci. Technol.* **1996**, *6*, 7–55. [CrossRef]

117.  Vinogradov, A.V.; Vinogradov, V.V. Low-temperature sol–gel synthesis of crystalline materials. *RSC Adv.* **2014**, *4*, 45903–45919. [CrossRef]

118. Sakka, S. History of ferroelectric materials prepared by sol-gel method. *J. Sol-Gel Sci. Technol.* **2022**, *101*, 140–175. [CrossRef]

119. Babaei, E.; Bazyari, A. Effects of drying conditions on physicochemical properties of epoxide sol−gel derived α-Fe$_2$O$_3$ and NiO: A comparison between xerogels and aerogels. *Ceram. Int.* **2022**, *48*, 33340–33349. [CrossRef]

120. Li, Y.; He, X.; Cao, M. Micro-emulsion-assisted synthesis of ZnS nanospheres and their photocatalytic activity. *Mater. Res. Bull.* **2008**, *43*, 3100–3110. [CrossRef]

121. Shi, W.; Lu, W.; Jiang, L. Fabrication of Amphiphilic Gold Nanoparticles of Well-Defined Size, High Concentration and Robust Colloidal Stability Fabrication of Amphiphilic Gold Nanoparticles of Well-Defined Size, High Concentration and Robust Colloidal Stability Fabrication of Amphiphilic Gold Nanoparticles of Well-Defined Size, High Concentration and Robust Colloidal Stability. *J. Nanosci. Nanotechnol.* **2009**, *9*, 5764–5769. [CrossRef] [PubMed]

122. Rao, J.P.; Geckeler, K.E. Polymer nanoparticles: Preparation techniques and size-control parameters. *Prog. Polym. Sci.* **2011**, *36*, 887–913. [CrossRef]

123. Jamil, S.; Janjua, M.R.S.A. Synthetic Study and Merits of Fe$_3$O$_4$ Nanoparticles as Emerging Material. *J. Clust. Sci.* **2017**, *28*, 2369–2400. [CrossRef]

124. Wang, S.; Xin, X.; Zhang, H.; Shen, J.; Zheng, Y.; Song, Z.; Yang, Y. Stable monodisperse colloidal spherical gold nanoparticles formed by an imidazolium gemini surfactant-based water-in-oil microemulsion with excellent catalytic performance. *RSC Adv.* **2016**, *6*, 28156–28164. [CrossRef]

125. Yu, X.M.; Meng, S.X.; Feng, Y.Q.; Liu, L.; Peng, X. TiO$_2$ Particles with Controlled Size Prepared by a Simple Micro-Emulsion Method and their Application in the Dye-Senstitized Solar Cell. *Adv. Mater. Res.* **2012**, *512*, 214–218. [CrossRef]

126. Entezari, M.H.; Ghows, N. Micro-emulsion under ultrasound facilitates the fast synthesis of quantum dots of CdS at low temperature. *Ultrason. Sonochem.* **2011**, *18*, 127–134. [CrossRef]

127. Malik, M.A.; Wani, M.Y.; Hashim, M.A. Microemulsion method: A novel route to synthesize organic and inorganic nanomaterials. *Arab. J. Chem.* **2012**, *5*, 397–417. [CrossRef]

128. Pei, L.; Wu, P.; Liu, J.; Wang, J. Effect of Nonionic Surfactant on the Micro-Emulsifying Water in Silicone Media. *J. Surfactants Deterg.* **2017**, *20*, 247–254. [CrossRef]

129. Duan, S.; Tang, R.; Xue, Z.; Zhang, X.; Zhao, Y.; Zhang, W.; Zhang, J.; Wang, B.; Zen, S.; Sun, D. Effective removal of Pb(II) using magnetic Co$_{0.6}$Fe$_{2.4}$O$_4$ micro-particles as the adsorbent: Synthesis and study on the kinetic and thermodynamic behaviors for its adsorption. *Colloids Surf. A Physicochem. Eng. Asp.* **2015**, *469*, 211–223. [CrossRef]

130. Sanchez-Dominguez, M.; Aubery, C.; Solans, C. New trends on the synthesis of inorganic nanoparticles using microemulsions as confined reaction media. *Smart Nanopart. Technol.* **2012**, 195–220.

131. Elayampallayam, T. Studies on synthesis, structure and optical properties of nickel nanoparticles. *J. Ovonic Res. Vol.* **2012**, *8*, 47–51.

132. Ahmad, T.; Ramanujachary, K.V.; Lofland, S.E.; Ganguli, A.K. Magnetic and electrochemical properties of nickel oxide nanoparticles obtained by the reverse-micellar route. *Solid State Sci.* **2006**, *8*, 425–430. [CrossRef]

133. Akaltun, Y.; Çayır, T. Fabrication and characterization of NiO thin films prepared by SILAR method. *J. Alloys Compd.* **2015**, *625*, 144–148. [CrossRef]

134. Das, M.R.; Roy, A.; Mpelane, S.; Mukherjee, A.; Mitra, P.; Das, S. Influence of dipping cycle on SILAR synthesized NiO thin film for improved electrochemical performance. *Electrochim. Acta* **2018**, *273*, 105–114. [CrossRef]

135. Taşdemirci, T.Ç. Influence of annealing on properties of SILAR deposited nickel oxide films. *Vacuum* **2019**, *167*, 189–194. [CrossRef]

136. Wang, X.; Wang, Y.; Tian, F.; Liang, H.; Kui, W.; Zhao, X.; Lu, Z.; Jiang, K.; Yang, L.; Lou, X. From the Surface Reaction Control to Gas-Diffusion Control: The Synthesis of Hierarchical Porous SnO$_2$ Microspheres and Their Gas-Sensing Mechanism. *J. Phys. Chem. C* **2015**, *119*, 15963–15976. [CrossRef]

137. Ji, H.; Zeng, W.; Li, Y. Gas sensing mechanisms of metal oxide semiconductors: A focus review. *Nanoscale* **2019**, *11*, 22664–22684. [CrossRef]

138. Shailja; Singh, K.J.; Singh, R.C. Highly sensitive and selective ethanol gas sensor based on Ga-doped NiO nanoparticles. *J. Mater. Sci. Mater. Electron.* **2021**, *32*, 11274–11290. [CrossRef]

139. Nakate, U.T.; Ahmad, R.; Patil, P.; Yu, Y.; Hahn, Y.-B. Ultra thin NiO nanosheets for high performance hydrogen gas sensor device. *Appl. Surf. Sci.* **2019**, *506*, 144971. [CrossRef]

140. Wang, B.; Nisar, J.; Ahuja, R. Molecular Simulation for Gas Adsorption at NiO (100) Surface. *ACS Appl. Mater. Interfaces* **2012**, *4*, 5691–5697. [CrossRef] [PubMed]

141. Gomaa, M.; Sayed, M.; Patil, V.; Boshta, M.; Patil, P. Gas sensing performance of sprayed NiO thin films toward NO$_2$ gas. *J. Alloys Compd.* **2021**, *885*, 160908. [CrossRef]

142. Zhang, J.; Zeng, D.; Zhao, S.; Wu, J.; Xu, K.; Zhu, Q.; Zhang, G.; Xie, C. Room temperature NO$_2$ sensing: What advantage does the rGO–NiO nanocomposite have over pristine NiO? *Phys. Chem. Chem. Phys.* **2015**, *17*, 14903–14911. [CrossRef] [PubMed]

143. Kampitakis, V.; Gagaoudakis, E.; Zappa, D.; Comini, E.; Aperathitis, E.; Kostopoulos, A.; Kiriakidis, G.; Binas, V. Highly sensitive and selective NO$_2$ chemical sensors based on Al doped NiO thin films. *Mater. Sci. Semicond. Process.* **2020**, *115*, 105149. [CrossRef]

144. Zhang, J.; Zeng, D.; Zhu, Q.; Wu, J.; Huang, Q.; Xie, C. Effect of Nickel Vacancies on the Room-Temperature NO$_2$ Sensing Properties of Mesoporous NiO Nanosheets. *J. Phys. Chem. C* **2016**, *120*, 3936–3945. [CrossRef]

145. Haunsbhavi, K.; Kumar, K.D.A.; Mele, P.; Aldossary, O.M.; Ubaidullah, M.; Mahesh, H.M.; Murahari, P.; Angadi, B. Pseudo n-type behaviour of nickel oxide thin film at room temperature towards ammonia sensing. *Ceram. Int.* **2021**, *47*, 13693–13703. [CrossRef]

146. Mokoena, T.P.; Tshabalala, Z.P.; Hillie, K.T.; Swart, H.C.; Motaung, D.E. The blue luminescence of p-type NiO nanostructured material induced by defects: $H_2S$ gas sensing characteristics at a relatively low operating temperature. *Appl. Surf. Sci.* **2020**, *525*, 146002. [CrossRef]

147. Lu, Y.; Ma, Y.H.; Ma, S.Y.; Jin, W.X.; Yan, S.H.; Xu, X.L.; Chen, Q. Curly porous NiO nanosheets with enhanced gas-sensing properties. *Mater. Lett.* **2017**, *190*, 252–255. [CrossRef]

148. Mokoena, T.P.; Swart, H.C.; Hillie, K.T.; Tshabalala, Z.P.; Jozela, M.; Tshilongo, J.; Motaung, D.E. Enhanced propanol gas sensing performance of p-type NiO gas sensor induced by exceptionally large surface area and crystallinity. *Appl. Surf. Sci.* **2021**, *571*, 151121. [CrossRef]

149. Nie, C.; Zeng, W.; Li, Y. The 3D crystal morphologies of NiO gas sensor and constantly improved sensing properties to ethanol. *J. Mater. Sci. Mater. Electron.* **2018**, *30*, 1794–1802. [CrossRef]

150. Dang, T.K.; Cuong, N.D.; Sinh, V.H.; Long, H.T.; Hieu, L.T.; Thy, P.N.A.; Quang, D.T.; Son, L.T.; Phuc, P.T.; Hue, P.T.; et al. Hexagonal annular-NiO nanoarchitecture with local p-n homojunctions: Novel formation mechanism and $H_2S$ gas sensing properties. *J. Alloys Compd.* **2023**, *933*, 167782. [CrossRef]

151. Zhou, Q.; Lu, Z.; Wei, Z.; Xu, L.; Gui, Y.; Chen, W. Hydrothermal Synthesis of Hierarchical Ultrathin NiO Nanoflakes for High-Performance $CH_4$ Sensing. *Front. Chem.* **2018**, *6*, 194. [CrossRef] [PubMed]

152. Haidry, A.A.; Yucheng, W.; Fatima, Q.; Raza, A.; Zhong, L.; Chen, H.; Mandebvu, C.R.; Ghani, F. Synthesis and characterization of $TiO_2$ nanomaterials for sensing environmental volatile compounds (VOCs): A review. *Trends Anal. Chem.* **2024**, *170*, 117454. [CrossRef]

153. Dang, T.T.L.; Tonezzer, M.; Nguyen, V.H. Hydrothermal growth and hydrogen selective sensing of nickel oxide nanowires. *J. Nanomater.* **2015**, *2015*, 6. [CrossRef]

154. Lin, L.; Liu, T.; Miao, B.; Zeng, W. Synthesis of NiO nanostructures from 1D to 3D and researches of their gas-sensing properties. *Mater. Res. Bull.* **2013**, *48*, 449–454. [CrossRef]

155. Dhas, S.D.; Maldar, P.S.; Patil, M.D.; Waikar, M.R.; Sonkawade, R.G.; Moholkar, A.V. Sol-gel synthesized nickel oxide nanostructures on nickel foam and nickel mesh for a targeted energy storage application. *J. Energy Storage* **2021**, *47*, 103658. [CrossRef]

156. Zhao, S.; Shen, Y.; Zhou, P.; Zhang, J.; Zhang, W.; Chen, X.; Wei, D.; Fang, P.; Shen, Y. Highly selective $NO_2$ sensor based on p-type nanocrystalline NiO thin films prepared by sol–gel dip coating. *Ceram. Int.* **2018**, *44*, 753–759. [CrossRef]

157. Yuan, C.; Li, H.; Xie, L.; Wang, F.; Deng, H.; Chang, F.; Sun, Y. Flower-like NiO nanostructures synthesized by electrodeposition method for efficient detection of toluene gas. *RSC Adv.* **2015**, *5*, 92128–92133. [CrossRef]

158. Zhang, Y.; Xie, L.-Z.; Li, H.-R.; Wang, P.; Liu, S.; Peng, Y.-Q.; Zhang, M. Facile Synthesis of Rose-Like NiO Nanoparticles and Their Ethanol Gas-Sensing Property. *Chin. Phys. Lett.* **2015**, *32*, 098103. [CrossRef]

159. Pai, S.H.S.; Mondal, A.; Barathy T, R.; Ajitha, B.; Samuel E, J.J.; Reddy, Y.A.K. Effect of calcination temperature on NiO for hydrogen gas sensor performance. *Int. J. Hydrogen Energy* **2024**, *50*, 928–941. [CrossRef]

160. Song, Z.; Zhang, L.; Zhou, Q.; Zhang, Z.; Dong, Z.; Nie, L.; Liu, Q.; Pan, G. In-situ synthesis of needle-like PdO-decorated NiO thin films on $Al_2O_3$ substrates for high-performance $H_2$ sensors. *Ceram. Int.* **2022**, *48*, 31746–31754. [CrossRef]

161. Wang, C.; Cui, X.; Liu, J.; Zhou, X.; Cheng, X.; Sun, P.; Hu, X.; Li, X.; Zheng, J.; Lu, G. Design of Superior Ethanol Gas Sensor Based on Al-Doped NiO Nanorod-Flowers. *ACS Sens.* **2016**, *1*, 131–136. [CrossRef]

162. Kaur, N.; Zappa, D.; Comini, E. Shelf Life Study of NiO Nanowire Sensors for $NO_2$ Detection. *Electron. Mater. Lett.* **2019**, *15*, 743–749. [CrossRef]

163. Kaur, N.; Zappa, D.; Ferroni, M.; Poli, N.; Campanini, M.; Negrea, R.; Comini, E. Branch-like NiO/ZnO heterostructures for VOC sensing. *Sens. Actuators B Chem.* **2018**, *262*, 477–485. [CrossRef]

164. Kaur, N.; Comini, E.; Poli, N.; Zappa, D.; Sberveglieri, G. NiO/ZnO Nanowire-heterostructures by Vapor Phase Growth for Gas Sensing. *Procedia Eng.* **2016**, *168*, 1140–1143. [CrossRef]

165. San, X.; Li, M.; Liu, D.; Wang, G.; Shen, Y.; Meng, D.; Meng, F. A facile one-step hydrothermal synthesis of NiO/ZnO heterojunction microflowers for the enhanced formaldehyde sensing properties. *J. Alloys Compd.* **2018**, *739*, 260–269. [CrossRef]

166. Ao, D.; Li, Z.; Fu, Y.; Tang, Y.; Yan, S.; Zu, X. Heterostructured NiO/ZnO Nanorod Arrays with Significantly Enhanced $H_2S$ Sensing Performance. *Nanomaterials* **2019**, *9*, 900. Available online: https://www.mdpi.com/2079-4991/9/6/900 (accessed on 20 June 2023). [CrossRef]

167. Zhou, W.-D.; Dastan, D.; Li, J.; Yin, X.-T.; Wang, Q. Discriminable sensing response behavior to homogeneous gases based on n-ZnO/p-NiO composites. *Nanomaterials* **2020**, *10*, 785. [CrossRef]

168. Liang, Y.-C.; Chang, Y.-C. The effect of Ni content on gas-sensing behaviors of ZnO–NiO p–n composite thin films grown through radio-frequency cosputtering of ceramic ZnO and NiO targets. *CrystEngComm* **2020**, *22*, 2315–2326. [CrossRef]

169. Zhao, S.; Shen, Y.; Xia, Y.; Pan, A.; Zhou, L.; Carraro, C.; Maboudian, R. Synthesis and gas sensing properties of NiO/ZnO heterostructured nanowires. *J. Alloys Compd.* **2021**, *877*, 160189. [CrossRef]

170. Lu, Y.; Ma, Y.; Ma, S.; Yan, S. Hierarchical heterostructure of porous NiO nanosheets on flower-like ZnO assembled by hexagonal nanorods for high-performance gas sensor. *Ceram. Int.* **2017**, *43*, 7508–7515. [CrossRef]

171. Wei, Z.; Zhou, Q.; Wang, J.; Lu, Z.; Xu, L.; Zeng, W. Hydrothermal Synthesis of $SnO_2$ Nanoneedle-Anchored NiO Microsphere and its Gas Sensing Performances. *Nanomaterials* **2019**, *9*, 1015. [CrossRef] [PubMed]

172. Mangalam, S.K.; Jose, A.S.; K., P.; Chowdhury, P.; Barshilia, H.C. Sputter deposited p-NiO/n-$SnO_2$ porous thin film heterojunction based $NO_2$ sensor with high selectivity and fast response. *Sens. Actuators B Chem.* **2020**, *310*, 127830. [CrossRef]

173. Bai, S.; Liu, C.; Luo, R.; Chen, A. Metal organic frameworks-derived sensing material of SnO$_2$/NiO composites for detection of triethylamine. *Appl. Surf. Sci.* **2018**, *437*, 304–313. [CrossRef]

174. Yan, S.; Song, W.; Wu, D.; Jin, S.; Dong, S.; Hao, H.; Gao, W. Assembly of In$_2$O$_3$ nanoparticles decorated NiO nanosheets heterostructures and their enhanced gas sensing characteristics. *J. Alloys Compd.* **2021**, *896*, 162887. [CrossRef]

175. Yu, Q.; Jin, R.; Zhao, L.; Wang, T.; Liu, F.; Yan, X.; Wang, C.; Sun, P.; Lu, G. MOF-Derived Mesoporous and Hierarchical Hollow-Structured In$_2$O$_3$-NiO Composites for Enhanced Triethylamine Sensing. *ACS Sens.* **2021**, *6*, 3451–3461. [CrossRef]

176. Deus, R.C.; Amoresi, R.A.C.; Desimone, P.M.; Schipani, F.; Rocha, L.S.R.; Ponce, M.A.; Simoes, A.Z.; Longo, E. Electrical behavior of cerium dioxide films exposed to different gases atmospheres. *Ceram. Int.* **2016**, *42*, 15023–15029. [CrossRef]

177. Li, H.; Qu, Y.; Zhang, X. The gas sensor utilizing CeO$_2$ nanorods for the low temperature detection of hydrogen. *Inorg. Chem. Commun.* **2021**, *130*, 108692. [CrossRef]

178. Zito, C.A.; Perfecto, T.M.; Dippel, A.-C.; Volanti, D.P.; Koziej, D. Low-Temperature Carbon Dioxide Gas Sensor Based on Yolk–Shell Ceria Nanospheres. *ACS Appl. Mater. Interfaces* **2020**, *12*, 17745–17751. [CrossRef] [PubMed]

179. Kabure, A.; Shirke, B.; Mane, S.; Garadkar, K. Microwave-assisted sol-gel synthesis of CeO$_2$–NiO nanocomposite based NO$_2$ gas sensor for selective detection at lower operating temperature. *J. Indian Chem. Soc.* **2022**, *99*, 100369. [CrossRef]

180. Liu, Y.; Sun, X.; Zhou, Z.; Lei, Y. Electrospun Ce–Ni–O composite nanofibers for highly selective propane detection at high temperature based on its rapid reaction kinetics. *J. Mater. Chem. A* **2014**, *2*, 14038–14047. [CrossRef]

181. Long, N.V.; Teranishi, T.; Yang, Y.; Thi, C.M.; Cao, Y.; Nogami, M. Iron Oxide Nanoparticles for Next Generation Gas Sensors. *Int. J. Met. Mater. Eng.* **2015**, *1*, 1–18. [CrossRef] [PubMed]

182. Wang, G.; Gou, X.; Horvat, J.; Park, J. Facile Synthesis and Characterization of Iron Oxide Semiconductor Nanowires for Gas Sensing Application. *J. Phys. Chem. C* **2008**, *112*, 15220–15225. [CrossRef]

183. Pan, H.; Li, Z.; Lou, C.; Lei, G.; Xie, J.; Zheng, W.; Liu, X.; Zhang, J. Anchoring Fe$_2$O$_3$ nanosheets on NiO nanoprisms to regulate the electronic properties for improved n-butanol detection. *Sens. Actuators B Chem.* **2022**, *354*, 131223. [CrossRef]

184. Wang, C.; Cheng, X.; Zhou, X.; Sun, P.; Hu, X.; Shimanoe, K.; Lu, G.; Yamazoe, N. Hierarchical α-Fe$_2$O$_3$/NiO composites with a hollow structure for a gas sensor. *ACS Appl. Mater. Interfaces* **2014**, *6*, 12031–12037. [CrossRef] [PubMed]

185. Lee, C.-S.; Dai, Z.; Jeong, S.-Y.; Kwak, C.-H.; Kim, B.-Y.; Kim, D.H.; Jang, H.W.; Park, J.-S.; Lee, J.-H. Monolayer Co$_3$O$_4$ inverse opals as multifunctional sensors for volatile organic compounds. *Chemistry* **2016**, *22*, 7102–7107. [CrossRef]

186. Gao, J.; Liu, C.; Guo, S.; Yang, L.; Yang, Y.; Xu, K. Hetero-epitaxy growth of cobalt oxide/nickel oxide nanowire arrays on alumina substrates for enhanced ethanol sensing characteristics. *Ceram. Int.* **2022**, *48*, 3849–3859. [CrossRef]

187. Su, C.; Zhang, L.; Han, Y.; Ren, C.; Zeng, M.; Zhou, Z.; Su, Y.; Hu, N.; Wei, H.; Yang, Z. Controllable synthesis of heterostructured CuO–NiO nanotubes and their synergistic effect for glycol gas sensing. *Sens. Actuators B Chem.* **2019**, *304*, 127347. [CrossRef]

188. Govindhan, M.; Sidhureddy, B.; Chen, A. High-Temperature Hydrogen Gas Sensor Based on Three-Dimensional Hierarchical-Nanostructured Nickel–Cobalt Oxide. *ACS Appl. Nano Mater.* **2018**, *1*, 6005–6014. [CrossRef]

189. Sui, L.; Yu, T.; Zhao, D.; Cheng, X.; Zhang, X.; Wang, P.; Xu, Y.; Gao, S.; Zhao, H.; Gao, Y.; et al. In situ deposited hierarchical CuO/NiO nanowall arrays film sensor with enhanced gas sensing performance to H$_2$S. *J. Hazard. Mater.* **2020**, *385*, 121570. [CrossRef]

190. Ding, Y.; Zhuang, Q.; Guo, X.; Li, H.; Liang, C.; Du, B.; Zhao, C.; Shi, Y.; Meng, G.; Li, R.; et al. NiO-CuO hydrangeas-like composite derived from Ni/Cu bimetallic MOFs for sensitive detection of H$_2$S at room temperature. *Appl. Surf. Sci.* **2023**, *612*, 155792. [CrossRef]

191. Nayak, A.K.; Ghosh, R.; Santra, S.; Guha, P.K.; Pradhan, D. Hierarchical nanostructured WO$_3$–SnO$_2$ for selective sensing of volatile organic compounds. *Nanoscale* **2015**, *7*, 12460–12473. [CrossRef] [PubMed]

192. Liu, H.; Wang, Z.; Cao, G.; Pan, G.; Yang, X.; Qiu, M.; Sun, C.; Shao, J.; Li, Z.; Zhang, H. Construction of hollow NiO/ZnO p-n heterostructure for ultrahigh performance toluene gas sensor. *Mater. Sci. Semicond. Process.* **2022**, *141*, 106435. [CrossRef]

193. Wang, S.-C.; Wang, X.-H.; Qiao, G.-Q.; Chen, X.-Y.; Wang, X.-Z.; Wu, N.-N.; Tian, J.; Cui, H.-Z. NiO nanoparticles-decorated ZnO hierarchical structures for isopropanol gas sensing. *Rare Met.* **2022**, *41*, 960–971. [CrossRef]

194. Selvaraj, B.; Rayappan, J.B.B.; Babu, K. Room temperature ZnO/NiO heterostructure sensing response: A breath biomarker sensor. *J. Alloys Compd.* **2022**, *914*, 165224. [CrossRef]

195. Zhang, J.; Li, J. The Oxygen Vacancy Defect of ZnO/NiO Nanomaterials Improves Photocatalytic Performance and Ammonia Sensing Performance. *Nanomaterials* **2022**, *12*, 433. [CrossRef]

196. Xu, S.; Wang, J.; Lin, H.; Li, R.; Cheng, Y.; Sang, S.; Zhuo, K. ZnO/NiO nanofibers prepared by electrostatic spinning for rapid ammonia detection at room temperature. *Electron. Mater. Lett.* **2022**, *18*, 568–577. [CrossRef]

197. Nagarjuna, Y.; Hsiao, Y.-J. Low-Temperature Ammonia Gas Sensor Based on NiO/ZnO Heterojunction Nanosheet on MEMS Devices. *J. Electrochem. Soc.* **2022**, *169*, 077502. [CrossRef]

198. Wang, X.; Wang, S.; Tian, J.; Cui, H.; Wang, X. Synthesis of 1D SnO$_2$ nanorods/2D NiO porous nanosheets p-n heterostructures for enhanced ethanol gas sensing performance. *Vacuum* **2022**, *205*, 111399. [CrossRef]

199. Das, S.; Kumar, A.; Singh, J.; Kumar, M. Fabrication and modeling of laser ablated NiO nanoparticles decorated SnO$_2$ based formaldehyde sensor. *Sens. Actuators B Chem.* **2023**, *387*, 133824. [CrossRef]

200. Hsiao, Y.-J.; Shi, Z.-H.; Nagarjuna, Y.; Huang, Z.-Y.; Lai, T.-Y.; Wu, S. Double-Layered NiO/SnO$_2$ Sensor for Improved SO$_2$ Gas Sensing with MEMS Microheater Device. *ECS J. Solid State Sci. Technol.* **2022**, *11*, 057002. [CrossRef]

201. Yin, X.-T.; Dastan, D.; Gity, F.; Li, J.; Shi, Z.; Alharbi, N.D.; Liu, Y.; Tan, X.-M.; Gao, X.-C.; Ma, X.-G.; et al. Gas sensing selectivity of $SnO_2$-xNiO sensors for homogeneous gases and its selectivity mechanism: Experimental and theoretical studies. *Sens. Actuators A Phys.* **2023**, *354*, 114273. [CrossRef]

202. Liang, Y.; Li, H.; Zhao, X.; Xue, L.; Tang, L.; Xue, F.; Yu, T.; Yang, Y. Crystal facets-controlled $NiO/SnO_2$ p-n heterostructures with engineered surface and interface towards triethylamine sensing. *J. Alloys Compd.* **2023**, *947*, 169503. [CrossRef]

203. Perrone, O.M.; Roveda, A.C.; de Moraes, D.A.; Theodoro, R.d.S.; Volanti, D.P. Highly efficient detection of ethanol by $SnO_2$ nanoparticles-decored NiO nanocuboids. *Mater. Res. Bull.* **2023**, *158*, 112086. [CrossRef]

204. Cai, Z.; Park, J.; Park, S. Synergistic effect of Pd and $Fe_2O_3$ nanoparticles embedded in porous NiO nanofibers on hydrogen gas detection: Fabrication, characterization, and sensing mechanism exploration. *Sens. Actuators B Chem.* **2023**, *388*, 133836. [CrossRef]

205. Li, L.; Zhou, L.; Hu, Z.; Li, T.; Chen, B.; Li, H.-Y.; Liu, H. Hollow-Out $Fe_2O_3$-Loaded NiO Heterojunction Nanorods Enable Real-Time Exhaled Ethanol Monitoring under High Humidity. *ACS Appl. Mater. Interfaces* **2023**, *15*, 15707–15720. [CrossRef]

206. Zhang, D.; Wang, T.; Huo, L.; Gao, S.; Li, B.; Guo, C.; Yu, H.; Major, Z.; Zhang, X.; Cheng, X.; et al. Small size porous $NiO/NiFe_2O_4$ nanocubes derived from Ni-Fe bimetallic metal–organic frameworks for fast volatile organic compounds detection. *Appl. Surf. Sci.* **2023**, *623*, 157075. [CrossRef]

207. Yang, J.; Han, W.; Jiang, B.; Wang, X.; Sun, Y.; Wang, W.; Lou, R.; Ci, H.; Zhang, H.; Lu, G. Electrospinning Derived $NiO/NiFe_2O_4$ Fiber-in-Tube Composite for Fast Triethylamine Detection under Different Humidity. *ACS Sens.* **2022**, *7*, 995–1007. [CrossRef]

208. Perrone, O.M.; Roveda, A.C.; de Moraes, D.A.; Volanti, D.P. The enhanced n-butanol sensing performance of $In_2O_3$ loaded NiO cuboid heterostructure. *J. Alloys Compd.* **2023**, *930*, 167483. [CrossRef]

209. Wang, X.; Zhang, W.; Wang, X.; Li, X.; Sui, X.; Liu, G.; Li, B.; Zhou, J.; Xie, E.; Zhang, Z. Facile fabrication of NiO foam@Sn-doped $In_2O_3$ nanowire heterosturctures for highly sensitive ethylene glycol gas sensors at low temperatures. *Sens. Actuators B Chem.* **2023**, *377*, 132991. [CrossRef]

210. Zhang, S.; Li, J.; Han, L.; Zhang, B.; Wang, Y.; Zhang, Z. Preparation of porous $NiO/In_2O_3$ nanoflower-like composites and their dual selectivity for $CO/CH_4$. *Mater. Res. Bull.* **2023**, *165*, 112332. [CrossRef]

211. Wu, Z.; Zhang, H.; Ji, H.; Yuan, Z.; Meng, F. Novel combined waveform temperature modulation method of $NiO-In_2O_3$ based gas sensor for measuring and identifying VOC gases. *J. Alloys Compd.* **2022**, *918*, 165510. [CrossRef]

212. Meng, D.; Qiao, T.; Wang, G.; Shen, Y.; San, X.; Pan, Y.; Meng, F. NiO-functionalized $In_2O_3$ flower-like structures with enhanced trimethylamine gas sensing performance. *Appl. Surf. Sci.* **2022**, *577*, 151877. [CrossRef]

213. Zhang, H.; Wei, W.; Tao, T.; Li, X.; Xia, X.; Bao, Y.; Lourenço, M.; Homewood, K.; Huang, Z.; Gao, Y. Hierarchical $NiO/TiO_2$ heterojuntion-based conductometric hydrogen sensor with anti-CO-interference. *Sens. Actuators B Chem.* **2023**, *380*, 133321. [CrossRef]

214. Lee, J.-H.; Kim, J.-Y.; Mirzaei, A.; Nam, M.-S.; Kim, H.W.; Kim, S.S. Room-temperature detection of acetone gas by PANI/NiO-loaded $TiO_2$ nanoparticles under UV irradiation. *Sens. Actuators B Chem.* **2023**, *374*, 132850. [CrossRef]

215. Li, C.; Choi, P.G.; Masuda, Y. Highly Sensitive and Selective Gas Sensors Based on $NiO/MnO_2$@NiO Nanosheets to Detect Allyl Mercaptan Gas Released by Humans under Psychological Stress. *Adv. Sci.* **2022**, *9*, e2202442. [CrossRef]

216. Wang, X.; Zhang, W.; Wang, X.; Li, X.; Sui, X.; Jiang, H.; Liu, G.; Li, B.; Sheng, Y.; Zhou, J.; et al. Heterostructure engineering of NiO foam/$In_2S_3$ film for high-performance ethylene glycol gas sensors. *Sens. Actuators B Chem.* **2023**, *392*, 134110. [CrossRef]

217. Yang, J.; Gui, Y.; Wang, Y.; He, S. $NiO/Ti_3C_2Tx$ MXene nanocomposites sensor for ammonia gas detection at room temperature. *J. Ind. Eng. Chem.* **2023**, *119*, 476–484. [CrossRef]

218. Zhang, P.; Sun, Y.; Ning, T.; Ren, Q.; Xu, M.; Zhao, X.; Chen, Q.; Huang, N.; Luo, X.; Zhai, C.; et al. Ultrasensitive Gas Sensor Based on Ball-Flower Like Wo3/Nio Composites for Fast No2 Detection. Available online: https://papers.ssrn.com/sol3/papers.cfm?abstract_id=4290985 (accessed on 27 December 2023).

219. Li, H.; Ding, B.; Wu, J.; Lv, Q. Synthesis of $MoO_3/NiO$ nanolamella and their enhanced hydrogen sensing performance. *Inorg. Chem. Commun.* **2022**, *145*, 109967. [CrossRef]

220. Yang, W.; Fang, B.; Xiao, X.; Meng, H.; Liu, S. Hierarchical core-shell heterostructures of α-$MoO_3$ nanorods@NiO nanosheets for significant detection of ethyl acetate vapor. *Sens. Actuators B Chem.* **2022**, *358*, 131457. [CrossRef]

221. Koo, W.-T.; Choi, S.-J.; Kim, S.-J.; Jang, J.-S.; Tuller, H.L.; Kim, I.-D. Heterogeneous Sensitization of Metal–Organic Framework Driven Metal@Metal Oxide Complex Catalysts on an Oxide Nanofiber Scaffold Toward Superior Gas Sensors. *J. Am. Chem. Soc.* **2016**, *138*, 13431–13437. [CrossRef] [PubMed]

222. Hwang, J.; Jung, H.; Shin, H.-S.; Kim, D.-S.; Kim, D.S.; Ju, B.-K.; Chun, M.P. The Effect of Noble Metals on Co Gas Sensing Properties of $In_2O_3$ Nanoparticles. *Appl. Sci.* **2021**, *11*, 4903. [CrossRef]

223. Rai, P.; Yoon, J.-W.; Jeong, H.-M.; Hwang, S.-J.; Kwak, C.-H.; Lee, J.-H. Design of highly sensitive and selective Au@NiO yolk–shell nanoreactors for gas sensor applications. *Nanoscale* **2014**, *6*, 8292–8299. [CrossRef] [PubMed]

224. Ahmad, R.; Bedük, T.; Majhi, S.M.; Salama, K.N. One-step synthesis and decoration of nickel oxide nanosheets with gold nanoparticles by reduction method for hydrazine sensing application. *Sens. Actuators B Chem.* **2019**, *286*, 139–147. [CrossRef]

225. Balamurugan, C.; Cho, K.; Park, B.; Kim, J.; Kim, N.; Pak, Y.; Kong, J.; Kwon, S. Large modulation of the chemical and electronic sensitization of $TiO_2/Ag/NiO$ nanostructure via in situ hydrothermal-induced heterointerface engineering. *Chem. Eng. J.* **2022**, *430*, 132690. [CrossRef]

226. Tian, K.; Wang, X.-X.; Li, H.-Y.; Nadimicherla, R.; Guo, X. Lotus pollen derived 3-dimensional hierarchically porous NiO microspheres for $NO_2$ gas sensing. *Sens. Actuators B Chem.* **2016**, *227*, 554–560. [CrossRef]

227. Fu, J.; Zhao, C.; Zhang, J.; Peng, Y.; Xie, E. Enhanced Gas Sensing Performance of Electrospun Pt-Functionalized NiO Nanotubes with Chemical and Electronic Sensitization. *ACS Appl. Mater. Interfaces* **2013**, *5*, 7410–7416. [CrossRef]

228. Fasaki, I.; Kandyla, M.; Tsoutsouva, M.; Kompitsas, M. Optimized hydrogen sensing properties of nanocomposite NiO:Au thin films grown by dual pulsed laser deposition. *Sens. Actuators B Chem.* **2013**, *176*, 103–109. [CrossRef]

229. Shin, W.; Matsumiya, M.; Izu, N.; Murayama, N. Hydrogen-selective thermoelectric gas sensor. *Sens. Actuators B Chem.* **2003**, *93*, 304–308. [CrossRef]

230. Wang, X.; Lu, J.; Han, W.; Yang, J.; Jiang, B.; Sun, Y.; Zhang, H.; Lu, G. Co-PBA MOF-derived hierarchical hollow $Co_3O_4$@NiO microcubes functionalized with Pt for superior $H_2S$ sensing. *Sens. Actuators B Chem.* **2021**, *342*, 130028. [CrossRef]

231. Chen, H.-I.; Hsiao, C.-Y.; Chen, W.-C.; Chang, C.-H.; Chou, T.-C.; Liu, I.-P.; Lin, K.-W.; Liu, W.-C. Characteristics of a Pt/NiO thin film-based ammonia gas sensor. *Sens. Actuators B Chem.* **2018**, *256*, 962–967. [CrossRef]

232. Majhi, S.M.; Naik, G.K.; Lee, H.-J.; Song, H.-G.; Lee, C.-R.; Lee, I.-H.; Yu, Y.-T. Au@NiO core-shell nanoparticles as a p-type gas sensor: Novel synthesis, characterization, and their gas sensing properties with sensing mechanism. *Sens. Actuators B Chem.* **2018**, *268*, 223–231. [CrossRef]

233. Kruefu, V.; Wisitsoraat, A.; Phokharatkul, D.; Tuantranont, A.; Phanichphant, S. Enhancement of p-type gas-sensing performances of NiO nanoparticles prepared by precipitation with $RuO_2$ impregnation. *Sens. Actuators B Chem.* **2016**, *236*, 466–473. [CrossRef]

234. John, R.A.B.; Kumar, A.R. Tailoring on p-type conductivity of nickel oxide nanostructures by palladium for the detection of 2-methoxy ethanol. *J. Mater. Sci. Mater. Electron.* **2023**, *34*, 664. [CrossRef]

235. Nakate, U.T.; Ahmad, R.; Patil, P.; Wang, Y.; Bhat, K.S.; Mahmoudi, T.; Yu, Y.T.; Suh, E.; Hahn, Y.-B. Improved selectivity and low concentration hydrogen gas sensor application of Pd sensitized heterojunction n-ZnO/p-NiO nanostructures. *J. Alloys Compd.* **2019**, *797*, 456–464. [CrossRef]

236. Kandyla, M.; Chatzimanolis-Moustakas, C.; Guziewicz, M.; Kompitsas, M. Nanocomposite NiO:Pd hydrogen sensors with sub-ppm detection limit and low operating temperature. *Mater. Lett.* **2014**, *119*, 51–55. [CrossRef]

237. Al-Bahrani, M.R.; Ahmad, W.; Mehnane, H.F.; Chen, Y.; Cheng, Z.; Gao, Y. Enhanced Electrocatalytic Activity by RGO/MWCNTs/NiO Counter Electrode for Dye-sensitized Solar Cells. *Nano-Micro Lett.* **2015**, *7*, 298–306. [CrossRef]

238. Yang, C.; Qing, Y.; An, K.; Zhang, Z.; Wang, L.; Liu, C. Facile synthesis of the N-doped graphene/nickel oxide with enhanced electrochemical performance for rechargeable lithium-ion batteries. *Mater. Chem. Phys.* **2017**, *195*, 149–156. [CrossRef]

239. Ahmad, R.; A Shah, M. Hydrothermally synthesised nickel oxide nanostructures on nickel foam and nickel foil for supercapacitor application. *Ceram. Int.* **2023**, *49*, 6470–6478. [CrossRef]

240. Yadav, A.; Verma, N. Efficient hydrogen production using Ni-graphene oxide-dispersed laser-engraved 3D carbon micropillars as electrodes for microbial electrolytic cell. *Renew. Energy* **2019**, *138*, 628–638. [CrossRef]

241. Irfan, M.; Liu, X.; Li, S.; Khan, I.U.; Li, Y.; Wang, J.; Wang, X.; Du, X.; Wang, G.; Zhang, P. High-performance glucose fuel cell with bimetallic Ni–Co composite anchored on reduced graphene oxide as anode catalyst. *Renew. Energy* **2020**, *155*, 1118–1126. [CrossRef]

242. Refaat, Z.; El Saied, M.; Abo El Naga, A.O.; Shaban, S.A.; Hassan, H.B.; Shehata, M.R.; El Kady, F.Y. Efficient $CO_2$ methanation using nickel nanoparticles supported mesoporous carbon nitride catalysts. *Sci. Rep.* **2023**, *13*, 4855. [CrossRef] [PubMed]

243. Liu, G.-T.; Chen, H.-F.; Lin, G.-M.; Ye, P.; Wang, X.-P.; Jiao, Y.-Z.; Guo, X.-Y.; Wen, Y.; Yang, H.-F. One-step electrodeposition of graphene loaded nickel oxides nanoparticles for acetaminophen detection. *Biosens. Bioelectron.* **2014**, *56*, 26–32. [CrossRef]

244. Buledi, J.A.; Liu, G.-T.; Liu, G.-T.; Liu, G.-T.; Liu, G.-T.; Liu, G.-T.; Liu, G.-T. A Reusable Nickel Oxide Reduced Graphene Oxide Modified Platinum Electrode for the Detection of Linezolid Drug. *Ind. Eng. Chem. Res.* **2023**, *62*, 4665–4675. [CrossRef]

245. Dung, N.Q.; Patil, D.; Jung, H.; Kim, J.; Kim, D. NiO-decorated single-walled carbon nanotubes for high-performance nonenzymatic glucose sensing. *Sens. Actuators B Chem.* **2013**, *183*, 381–387. [CrossRef]

246. Wang, B.; Gu, Y.; Chen, L.; Ji, L.; Zhu, H.; Sun, Q. Gas sensing devices based on two-dimensional materials: A review. *Nanotechnology* **2022**, *33*, 252001. [CrossRef]

247. Gavgani, J.N.; Tavakoli, N.; Heidari, H.; Mahyari, M. Graphene-based nanocomposites sensors for detection of ammonia. *Int. J. Environ. Anal. Chem.* **2022**, 1–25. [CrossRef]

248. Sun, D.; Luo, Y.; Debliquy, M.; Zhang, C. Graphene-enhanced metal oxide gas sensors at room temperature: A review. *Beilstein J. Nanotechnol.* **2018**, *9*, 2832–2844. [CrossRef]

249. Kiranakumar, H.V.; Thejas, R.; Naveen, C.S.; Khan, M.I.; Prasanna, G.D.; Reddy, S.; Oreijah, M.; Guedri, K.; Bafakeeh, O.T.; Jameel, M. A review on electrical and gas-sensing properties of reduced graphene oxide-metal oxide nanocomposites. *Biomass-Convers. Biorefinery* **2022**, 1–11. [CrossRef]

250. Malepe, L.; Ndungu, P.; Ndinteh, D.T.; Mamo, M.A. Nickel Oxide-Carbon Soot-Cellulose Acetate Nanocomposite for the Detection of Mesitylene Vapour: Investigating the Sensing Mechanism Using an LCR Meter Coupled to an FTIR Spectrometer. *Nanomaterials* **2022**, *12*, 727. [CrossRef] [PubMed]

251. Ngo, Y.-L.T.; Hur, S.H. Low-temperature $NO_2$ gas sensor fabricated with NiO and reduced graphene oxide hybrid structure. *Mater. Res. Bull.* **2016**, *84*, 168–176. [CrossRef]

252. Hoa, L.T.; Tien, H.N.; Luan, V.H.; Chung, J.S.; Hur, S.H. Fabrication of a novel 2D-graphene/2D-NiO nanosheet-based hybrid nanostructure and its use in highly sensitive $NO_2$ sensors. *Sens. Actuators B Chem.* **2013**, *185*, 701–705. [CrossRef]

253. Zhang, D.; Chang, H.; Li, P.; Liu, R. Characterization of nickel oxide decorated-reduced graphene oxide nanocomposite and its sensing properties toward methane gas detection. *J. Mater. Sci. Mater. Electron.* **2016**, *27*, 3723–3730. [CrossRef]

254. Bayoumy, A.M.; Gomaa, I.; Elhaes, H.; Sleim, M.; Ibrahim, M.A. Application of Graphene/Nickel Oxide Composite as a Humidity Sensor. *Egypt. J. Chem.* **2021**, *64*, 85–91.

255. Li, L.; Zhang, G.; Chen, L.; Bi, H.-M.; Shi, K.-Y. Ni(NiO)/single-walled carbon nanotubes composite: Synthesis of electro-deposition, gas sensing property for NO gas and density functional theory calculation. *Mater. Res. Bull.* **2013**, *48*, 504–511. [CrossRef]

256. Chen, N.; Li, Q.; Li, Y.; Deng, D.; Xiao, X.; Wang, Y. Facile synthesis and gas sensing performances based on nickel oxide nanoparticles/multi-wall carbon nanotube composite. *J. Mater. Sci. Mater. Electron.* **2015**, *26*, 8240–8248. [CrossRef]

257. Adekunle, A.S.; Ozoemena, K.I. Electron transfer behaviour of single-walled carbon nanotubes electro-decorated with nickel and nickel oxide layers. *Electrochim. Acta* **2008**, *53*, 5774–5782. [CrossRef]

258. Hua, C.; Shang, Y.; Wang, Y.; Xu, J.; Zhang, Y.; Li, X.; Cao, A. A flexible gas sensor based on single-walled carbon nanotube-$Fe_2O_3$ composite film. *Appl. Surf. Sci.* **2017**, *405*, 405–411. [CrossRef]

259. Lu, G.; Ocola, L.E.; Chen, J. Room-temperature gas sensing based on electron transfer between discrete tin oxide nanocrystals and multiwalled carbon nanotubes. *Adv. Mater.* **2009**, *21*, 2487–2491. [CrossRef]

260. Govind, A.; Bharathi, P.; Mathankumar, G.; Mohan, M.K.; Archana, J.; Harish, S.; Navaneethan, M. Enhanced charge transfer in 2D carbon- rich g-$C_3N_4$ nanosheets for highly sensitive $NO_2$ gas sensor applications. *Diam. Relat. Mater.* **2022**, *128*, 109205. [CrossRef]

261. Li, X.; Wang, Y.; Tian, W.; Cao, J. Graphitic Carbon Nitride Nanosheets Decorated Flower-like NiO Composites for High-Performance Triethylamine Detection. *ACS Omega* **2019**, *4*, 9645–9653. [CrossRef] [PubMed]

262. Srirattanapibul, S.; Nakarungsee, P.; Issro, C.; Tang, I.-M.; Thongmee, S. Performance of NiO intercalated rGO nanocomposites for $NH_3$ sensing at room temperature. *Mater. Sci. Semicond. Process.* **2022**, *137*, 106221. [CrossRef]

263. Yang, M.; Zhang, X.; Cheng, X.; Xu, Y.; Gao, S.; Zhao, H.; Huo, L. Hierarchical NiO Cube/Nitrogen-Doped Reduced Graphene Oxide Composite with Enhanced $H_2S$ Sensing Properties at Low Temperature. *ACS Appl. Mater. Interfaces* **2017**, *9*, 26293–26303. [CrossRef]

264. Kamal, T. High performance NiO decorated graphene as a potential $H_2$ gas sensor. *J. Alloys Compd.* **2017**, *729*, 1058–1063. [CrossRef]

265. Kavitha, G.; Vinoth Kumar, J.; Arulmozhi, R.; Kamath, S.M.; Priya, A.K.; Rao, K.S.; Abirami, N. 2D graphene supported nickel oxide nano-composite for fiber optic ethanol gas sensing, removal of azo dye, and biological activity. *J. Mater. Sci. Mater. Electron.* **2022**, *33*, 9498–9511. [CrossRef]

266. Jung, D.; Han, M.; Lee, G.S. Gas-sensing properties of multi-walled carbon-nanotube sheet coated with NiO. *Carbon* **2014**, *78*, 156–163. [CrossRef]

267. Yan, Y.; Yang, G.; Xu, J.-L.; Zhang, M.; Kuo, C.-C.; Wang, S.-D. Conducting polymer-inorganic nanocomposite-based gas sensors: A review. *Sci. Technol. Adv. Mater.* **2020**, *21*, 768–786. [CrossRef]

268. Šetka, M.; Drbohlavová, J.; Hubálek, J. Nanostructured Polypyrrole-Based Ammonia and Volatile Organic Compound Sensors. *Sensors* **2017**, *17*, 562. [CrossRef]

269. Hu, Q.; Wang, Z.; Chang, J.; Wan, P.; Huang, J.; Feng, L. Design and preparation of hollow NiO sphere- polyaniline composite for $NH_3$ gas sensing at room temperature. *Sens. Actuators B Chem.* **2021**, *344*, 130179. [CrossRef]

270. Singh, P.; Kushwaha, C.S.; Shukla, S.; Dubey, G. Synthesis and Humidity Sensing Properties of NiO Intercalated Polyaniline Nanocomposite. *Polym. Technol. Mater.* **2019**, *58*, 139–147. [CrossRef]

271. Ramesan, M.T.; Nushhat, K.; Parvathi, K.; Anilkumar, T. Nickel oxide @ polyindole/phenothiazine blend nanocomposites: Preparation, characterization, thermal, electrical properties and gas sensing applications. *J. Mater. Sci. Mater. Electron.* **2019**, *30*, 13719–13728. [CrossRef]

272. Ramesan, M.T.; Santhi, V. Synthesis, characterization, conductivity and sensor application study of polypyrrole/silver doped nickel oxide nanocomposites. *Compos. Interfaces* **2018**, *25*, 725–741. [CrossRef]

273. Zhang, J.; Wu, C.; Li, T.; Xie, C.; Zeng, D. Highly sensitive and ultralow detection limit of room-temperature $NO_2$ sensors using in-situ growth of PPy on mesoporous NiO nanosheets. *Org. Electron.* **2020**, *77*, 105504. [CrossRef]